IMPACTS OF STORM ON SEA ICE: FROM CASE STUDY TO CLIMATE SCALE ANALYSIS

By

Liran Peng, M.S.

A Dissertation Submitted in Partial Fulfillment of the Requirements

for the degree of

DOCTOR OF PHILOSOPHY

i n

Atmospheric Science

University of Alaska Fairbanks

December 2019

APPROVED by:

Xiangdong Zhang, Advisor and Committee Chair

Richard Collins, Committee Member

Javier Fochesatto, Committee Member

Igor Polyakov, Committee Member

Javier Fochesatto, Chair

Department of Atmospheric Science

Leah Wrenn Berman, Interim Dean

College of Natural Science and Mathematics

Michael Castellini, Interim Dean, *Graduate School*

ABSTRACT

Recent studies have shown that intense and long-lasting storms potentially facilitate sea ice melting. Under the background of extratropical storm tracks poleward shift, significant reductions of Arctic sea ice coverage, and thinning of sea ice thickness over the last several decades, a better understanding on how storms impact sea ice mass balance is obviously of great importance to better predict future sea ice and the Arctic climate changes. This thesis presents a multi-scale study on how storms impact sea ice, consisting of three different parts of the effort. In the first part, we examined the impacts of the 2016 summer intense storm on sea ice changes over the Chukchi Sea using ship-borne observations. The results show that the intense storm can accelerate ice melt through enhanced upper-ocean mixing and upward heat transport.

The satellite-observed long-term sea ice variations potentially can be impacted by many factors. In the second part, we first explore key physical processes controlling sea ice changes under no-storm condition. We examined and compared results from 25 sensitivity experiments using the NCAR's Community Earth System Model (CESM). We found that sea ice volume, velocity, and thickness are highly sensitive to perturbed air-ice momentum flux and sea ice strength. Increased sea ice strength or decreased air-ice momentum flux causes counter-clockwise rotation of the transpolar drift, resulting in an increase in sea ice export through Fram Strait and therefore reduction of the pan-Arctic sea ice thickness. Following four tracers released over the Arctic, we found the sea ice thickness distributions following those tracers are broader over the western Arctic and becomes narrower over the eastern Arctic. Additionally, thermodynamic processes are more dominant controlling sea ice thickness variations, especially over periphery seas. Over the eastern Arctic, dynamic processes play a more important role in controlling sea

ice thickness variation. Previous studies show that thin ice responds to external perturbations much faster than the thick ice. Therefore, the impacts of storms on sea ice are expected to be different compared with the western/eastern Arctic and the central/periphery seas. In the third part, we conduct a new composite analysis to investigate the storm impact on sea ice over seven regions for all storms spanning from 1979 to 2018. We focused on sea ice and storm changes over seven regions and found storms tend to have different short-term (two days before and after storm passage), mid-term (one-two weeks after storm passage), and long-term (from 1979 to 2018) impact on sea ice area over those regions. Over periphery seas (Chukchi, East Siberian, Laptev, Kara, and Barents Seas), storms lead to a short-term sea ice area decrease below the climatology, and a mid-term sea ice increase above the climatology. This behavior causes sea ice area to have a small correlation with the storm counts from 1979 to 2018, which suggest that storms have a limited long-term impact on sea ice area over periphery seas. Both the short-term and mid-term storm impacts on sea ice area are confined within a 400 km radius circle with maximum impacts shown within a 200 km radius circle. Storms over the western Arctic (Chukchi, East Siberian, and Laptev Seas) have a stronger short-term and mid-term impact on sea ice area compared with the Eastern Arctic (Barents and Kara Seas). Storms over both Atlantic and Pacific entrance regions have a small impact on sea ice area, and storms over the Norwegian, Iceland, and Greenland Seas have the smallest impact on the sea ice area. Compared to the periphery seas, storms tend to have a stronger long-term impact on sea ice area over the central Arctic. The correlation coefficients between the storm count and sea ice area exceed 0.75.

Table of Contents

List of Figures

Page

List of Tables

Page

Acknowledgements

I want to take this opportunity to thank all of those who have been helped me and contributed to this dissertation work. Foremost, I would like to thank my Ph.D. advisor, Dr. Xiangdong Zhang, for his guidance, constant patience, and supports without which my thesis would not have been possible. Dr. Zhang has set an example of excellence as research, mentor, instructor, and scientific ethics. He is someone you will instantly love and never forget once you meet him. Dr. Zhang gives me the opportunity to work on the cutting-edge research topic in his research group. He helped me design my research pathway and encouraged me to work independently but would come through if I really need help. His expertise and insight suggestions are gratefully appreciated. Through this process, I obtained so much knowledge and gradually learned how to solve the problem like a real scientist, which will benefit me in my career endeavors.

My sincere thanks also go to my committee members Drs. Richard Collins, Javier Fochesatto, and Igor Polyakov for serving in my defense committee and answering my questions despite their overwhelmingly busy schedule. The improvement at different stages of my research benefitted a lot from many fruitful discussions with them. I would like to express my deepest gratitude for the teaching and guidance they provided. I would also like to thank Dr. Berman for her insightful comments and suggestions. I would also like to thank Marie-Sylvestre Olesen for her help on revising the final draft.

This research was funded by the National Science Foundation (NSF) Grant ARC-1023592.

Additionally, I would also like to extend my deepest gratitude to my collaborators in different part of this research, including Dr. Joo-Hong Kim (Korea Polar Research Institute, South Korea), Dr. Baek-Min Kim (Pukyong National University), Kyoung-Ho Cho (Korea Polar Research Institute, South Korea), Dr. Sang-Jong Park (Korea Polar Research Institute, South Korea), Dr. Jing Zhang (North Carolina Agricultural and Technical State University), Dr. Wei Tao (North Carolina Agricultural and Technical State University), and Dr. Zhaomin Wang (Hohai University). I also thank Kwang Ho Jin, Changkyu Lim, Zelin Xie, Yizhi Li, and Liangjun Yang for their collaboration on the fieldwork on Araon. I will forever be thankful to my former research advisors, Dr. Shoujuan Shu, Dr. Zhien Wang, and Dr. Jefferson Robert Snider. I would not have made it this far without them. They are the reason why I decided to go to pursue a career in research. There are so many people I would like to acknowledge, but it is almost impossible to list all of them here.

Finally, I would like to thank my family for their unconditional love and support. I would like to express my particular gratitude to my parents for their understanding and support of me pursuing my education and career. I want to thank my wife Yang Yang, for her love and support. Her love and support have kept me smiling and inspired. There are no words to convey how much I love her. I'll never forget many wonderful moments we have spent together.

Chapter 1 Introduction

The Arctic has been experiencing unprecedented changes in recent decades including more mid-latitude storms entering the Arctic (Zhang et al., 2004; Yin, 2005; Chang et al., 2012), a significant reduction of the sea ice coverage (e.g., Comiso, 2012; Stroeve et al., 2012; Cavalieri and Parkinson, 2012) and thinning of the sea ice thickness (e.g., Yu et al., 2004; Kwok and Rothrock, 2009; Lindsay and Schweiger, 2015). Melting sea ice has opened up the prospect of exploring the massive oil, gas, mineral, and fishery resources, and new shipping routes that were considered impregnable environments (Emmerson and Lahn, 2012). This expanding economic opportunity is also challenged by a variety of hazards. Increases in the frequency and intensity of Arctic storms (Dickson et al., 2000; Graham and Diaz, 2001) and the resulting weather hazards have caused risks to the offshore environment (Dupre, 1980; Dau et al., 2011; Terenzi et al., 2014), coastal community, and landscape (Anderson et al., 2018), aircraft/ship transportation (Arctic Council, 2009; Overland, 1990), and energy infrastructures (Holland-Bartels and Pierce, 2011).

Storm activity has been linked to various modes of large-scale atmospheric variability such as the Arctic Oscillation (AO) and the North Atlantic Oscillation (NAO). During positive NAO phase, both Icelandic Low and Azores High are strong, storm tracks over the North Atlantic exhibit a north-eastward orientation and more numerous in storm counts, while an east-west orientation and fewer storms counts are associated with negative NAO phase (Rogers, 1990; Serreze et al., 1997). The phase shift of the NAO may also influence storm activity over Europe (Ulbrich and Christoph, 1999). An increasing storm activity from 1988 to 1991 was found to be linked to the increase of the AO index (Zhang et al., 2004), especially over the Pacific (Chang

and Fu, 2002). The transition from tri-polar AO/NAO to a dipolar pattern could potentially be a manifestation of the intensified storm activity (Zhang et al., 2008).

Rapid sea ice decline has also been linked with large-scale atmospheric variability. From 1970 to 1989, the winter AO index shifted from negative to positive, which resulted in a weakening of the Beaufort High and westward shift of the Transpolar Drift. Decreased cyclonic sea ice motion weakens thin ice production during the winter. A positive AO also causes less sea ice recirculation and more sea ice export through the Fram Strait with a stronger ice velocity (Rigor et al., 2002).

At shorter time scales, storms potentially impact on sea ice in different ways. Recent studies have shown evidence that storms bring warm and humid air from lower latitudes into higher latitudes (Kim et al., 2017), form mixed-phase clouds (Shupe and Intrieri, 2004; Doyle et al., 2011; Persson, 2012; Persson et al., 2016), and result in variations of sea ice melting/growth rate (Boisvert et al., 2016). Storms-induced high surface winds may cause upwelling along the Beaufort Sea continental slope (Pickart et al., 2009) so that mixing can penetrate through the halocline (Yang et al., 2001) and even can go deeper into the thermocline (Yang et al., 2004). According to model simulations, excessive upward heat transport during the intense summer storm in 2012 resulted in rapid sea-ice bottom melt and sea ice decrease afterward (Zhang et al., 2013). Based on satellite and ice-drift buoy datasets, storms cause surface divergence, which leads to sea ice concentration decrease and formation of open water areas (Maslanik and Barry, 1989; Barry and Maslanik, 1989; Maslanik et al., 1995). Furthermore, sea ice separated from the main ice pack due to the 2012 storm could potentially facilitate sea ice melting since it

became more vulnerable to external forcing (Simmonds and Rudeva, 2012; Parkinson and Comiso, 2013).

Storms often induce strong perturbations compared with pre-storm and climatology conditions. Regional sea ice conditions play an essential role through its influence on the energy exchange between the atmosphere and ocean. Forced by the atmosphere, ice floes tend to move much slower or even decoupled with the surface winds (Steele et al., 1997). Thus, complete ice coverage tends to impede the downward momentum transfer. On the other hand, observations show that the average air-ice drag is much greater than the air-ocean drag (Large and Pond, 1981; Overland, 1985; Guest and Davidson, 1991; Fairall et al., 2003), which indicates that partial sea-ice cover can facilitate downward momentum transfer. The model study shows that the optimal ice concentration, which leads to a maximum momentum flux into the ocean, is 80-90% (Martin et al., 2014). Through the growth-thickness feedback (Bitz and Roe, 2004), sea ice thickness plays an important role in controlling the sea ice growth rate. When subject to a perturbation, thin ice reaches a new equilibrium state via fast adjustment to the sea-ice growth rate, while thick ice requires more response time and eventually melts more compared with thin ice. Therefore, to accurately capture storm impact on sea ice, the climatological condition of sea ice thickness distribution is expected to be an important factor governing how fast sea ice responds to external forcing induced by storms.

Due to the fact that storms induce complex air-ice-sea interactions at different temporal and spatial scales, it still remains unclear how storms impact on underlying sea ice and ocean during and after the storm passage. Additionally, previous studies did not provide direct evidence on how storms impact long-term regional sea ice changes due to other factors that may also

contribute to the long-term sea ice changes. We take advantage of using the climatological forcing to exclude the impact by storms and examine what major factors impact on long-term sea ice changes are. Results from this part of the analysis further guide us to explore more direct evidence on the long-term storm impact on sea ice over different regions using a newly developed composite analysis. Improvements of knowledge on the climatology of storms and sea ice, and furthering understanding of the impacts of storms on sea ice, its seasonal and interannual variations, geographical variations, impact durations, as well as impact ranges is important for predicting future sea ice changes, designing offshore drilling and production platforms as well as onshore support facilities.

This dissertation has three foci from synoptic scale case study to climate scale statistical analysis.

a. In 2016, the September sea ice extent became the second-lowest record since the beginning of the satellite era. Strong storms, which caused rapid sea ice decrease, occurred during August and was captured by the Korean ice breaker AROAN. How do those storms impact sea ice energy budgets and therefore the sea ice mass balance? What physical process governs the sea ice energy change during the storm period?
b. Under the climatological conditions (no-storm condition), what factors control the sea ice thickness distribution according to model simulations? In the pan-Arctic scale, how does sea ice thickness distribution respond to the various magnitude of air-ice drag and sea ice strength? How does sea ice thickness respond to thermodynamic and dynamic external forcing over different regions?

c. What are the short-term trends of storm counts and sea ice area over the Arctic from 1979-2018? Over different locations and time of the year, how do storms impact sea ice? What are the seasonal and interannual variations of storm counts? Within the same time and locations, how does sea ice area change? Over different locations and time of the year, how do storms impact sea ice? What are the storms' short-term, mid-term, and long-term impact on sea ice?

Following this chapter, the dissertation is split into three parts focusing on the major questions listed above. Specifically, Chapter 2 provides observational evidence on how the 2016 storm impacts sea ice according to the ship-based and satellite-based measurements. Through this study, we focused primarily on storm-induced thermodynamic processes. Chapter 3 will discuss feedback mechanisms controlling the sea ice thickness distribution on a pan-Arctic scale: how sea ice thickness varies under different air-ice drag and sea ice strength conditions. Chapter 4 will discuss a new composite analysis and provide more general conclusions on how storms impact sea ice at different temporal and spatial scales. In this chapter, we compared changes of storm counts, sea ice conditions, and storm impact on sea ice over seven regions categorized into four ten-year windows, 1979-1988, 1989-1998, 1999-2008, and 2009-2018.

References

Anderson, T. R., and Coauthors (2018), Modeling multiple sea level rise stresses reveals up to twice the land at risk compared to strictly passive flooding methods. *Sci. Rep.*, **8**(1), 14484.

Arctic Council (2009), Arctic marine shipping assessment 2009 report. *Tech. Rep.*, Arctic Council Norweigian Chairmanship.

Barry, R. G., and J. A. Maslanik (1989), Arctic sea ice characteristics and associated atmosphere-ice interactions in summer inferred from SMMR data and drifting buoys, 1979-1984, *Geo. Journal*, **18**, 35–44.

Bitz, C. M., and G. H. Roe (2004), A Mechanism for the High Rate of Sea Ice Thinning in the Arctic Ocean, *J. Clim.*, **17**, 3623–3632.

Boisvert, L., A. Petty, J. Stroeve (2016), The impact of the extreme winter 2015/16 Arctic cyclone on the Barents–Kara Seas. *Mon. Weather. Rev.*, **144**, 4279–4287. https://doi.org/10.1175/mwr-d-16-0234.1.

Cavalieri, D. J., and C. L. Parkinson (2012), Arctic sea ice variability and trends, 1979–2010, *The Cryosphere*, **6**(4), 881–889, doi:10.5194/tc-6-881-2012.

Chang, E. K. M., and Y. Fu, (2002), Interdecadal Variations in Northern Hemisphere Winter Storm Track Intensity. *J. Clim.*, **15**, 642-658.

Chang, E. K. M., Y. Guo, and X. Xia (2012), CMIP5 multimodel ensemble projection of storm track change under global warming, *J. Geophys. Res.*, **117**, D23118, doi:10.1029/2012JD018578.

Comiso, J. C. (2012), Large Decadal Decline of the Arctic Multiyear Ice Cover, *J. Clim.*, **25**(4), 1176–1193, doi:10.1175/JCLI-D-11-00113.1.

Dau, C. P., J. G. King Jr. and C. J. Lensink (2011), Effects of storm surge erosion on waterfowl habitats at the Kashunuk River, Yukon– Kuskokwim Delta, Alaska. U.S. Fish and Wildlife Service, Anchorage, Alaska, USA.

Dickson, R. R., and Coauthors, 2000: The Arctic Ocean Response to the North Atlantic Oscillation. *J. Clim.*, **13**, 2671-2696.

Doyle, J. G., and Coauthors (2011), Water vapor intrusions into the high Arctic during winter. *Geophys. Res. Lett.*, **38**, L12806. doi: 10.1029/2011GL047493.

Dupre, W. R. (1980), Yukon Delta coastal processes study. National Oceanic and Atmospheric Administration, Outer Continental Shelf Environmental Assessment Program, *Tech. Rep.*, **58**, 393–447.

Emmerson, C., and G. Lahn (2012), Arctic opening: opportunity and risk in the high north. Lloyds, Chattham House, London.

Fairall, C. W., E. F. Bradley, J. E. Hare, A. A. Grachev, and J. B. Edson (2003), Bulk parameterization of air-sea fluxes: Updates and verification for the COARE algorithm, *J. Clim.*, **16**(4), 571–591.

Graham, N. E., and H. F. Diaz (2001), Evidence for Intensification of North Pacific Winter Cyclones since 1948. *Bull. Amer. Meteor. Soc.*, **82**, 1869-1893.

Guest, P. S., and K. L. Davidson (1991), The aerodynamic roughness of different types of sea ice, *J. Geophys. Res.*, **96**(C3), 4709–4721.

Holland-Bartels, L. and B. Pierce (2011), An evaluation of the science needs to inform decisions on outer continental shelf energy development in the Chukchi and Beaufort seas, Alaska, U.S. Geological Survey Circular 1370.

Kim, B-M, and Coauthors (2017), Major cause of unprecedented Arctic warming in January 2016: critical role of an Atlantic windstorm. *Sci. Rep.*, **7**, 40051.

Kwok, R., and D. A. Rothrock (2009), Decline in Arctic sea ice thickness from submarine and ICESat records: 1958-2008, *Geophys. Res. Lett.*, **36**, L15501, doi:10.1029/2009GL039035.

Large, W. G., and S. Pond (1981), Open ocean momentum flux measurements in moderate to strong winds, *J. Phys. Oceanogr.*, **11**(3), 324–336.

Lindsay, R. W., and A. Schweiger (2015), Arctic sea ice thickness loss determined using subsurface, aircraft, and satellite observations. *The Cryosphere*, **9**, 269–283. https://doi.org/10.5194/tc-9-269-2015.

Martin, T., M. Steele, and J. Zhang (2014), Seasonality and long-term trend of Arctic Ocean surface stress in a model, *J. Geophys. Res. Oceans*, **119**, 1723–1738, doi:10.1002/2013JC009425.

Maslanik, J. A., and R. G. Barry (1989), Short-term interactions between atmospheric synoptic conditions and sea-ice behaviour in the Arctic, *Ann. Glaciol.*, **12**, 113–117, 1.

Maslanik, J., and J. Key (1995), On treatments of fetch and stability sensitivity in large-area estimates of sensible heat flux over sea ice, *J. Geophys. Res.*, **100**(C3), 4573–4584.

Overland, J. E. (1985), Atmospheric boundary layer structure and drag coefficients over sea ice, *J. Geophys. Res.*, **90**(C5), 9029–9049.

Overland, J. E. (1990), Prediction of Vessel Icing for Near-Freezing Sea Temperatures. *Weather and Forecasting*, **5**, 62-77.

Parkinson, C. L., and J. C. Comiso (2013), On the 2012 record low Arctic sea ice cover: Combined impact of preconditioning and an August storm, *Geophys. Res. Lett.*, **40**, 1356–1361, doi:10.1002/grl.50349.

Persson, P. O. G. (2012), Onset and end of the summer melt season over sea ice: Thermal structure and surface energy perspective from SHEBA, *Clim. Dyn.*, **39**(6), 1349–1371, doi:10.1007/s00382-011-1196-9.

Persson, P. O. G., M. D. Shupe, D. Perovich, and A. Solomon (2016), Linking atmospheric synoptic transport, cloud phase, surface energy fluxes, and sea-ice growth: observations of midwinter SHEBA condition, *Clim. Dyn.*, 1–24.

Pickart, R. S., and Coauthors (2009), Upwelling on the continental slope of the Alaskan Beaufort Sea: Storms, ice, and oceanographic response, *J. Geophys. Res.*, **114**, C00A13, doi:10.1029/2008JC005009.

Rigor, I. G., J. M. Wallace, and R. L. Colony (2002), Response of Sea Ice to the Arctic Oscillation, *J. Clim.*, **15**, 2648–2663.

Rogers, J. C. (1990), Patterns of low-frequency monthly sea level pressure variability (1899–1986) and associated wave cyclone frequencies. *J. Clim.*, **3**, 1364–1379.

Serreze, M. C, F. Carse, R. G. Barry, and J. C. Rogers (1997), Icelandic low activity: climatological features, linkages with the NAO, and relationships with recent changes in the Northern Hemisphere circulation. *J. Clim.*, **10**, 453-164.

Shupe, M. D., and J. M. Intrieri (2004), Cloud radiative forcing of the Arctic surface: The influence of cloud properties, surface albedo, and solar zenith angle, *J. Clim.*, **17**(3), 616–628, doi:10.1175/1520-0442(2004)017<0616:CRFOTA>2.0.CO;2.

Simmonds, I., and I. Rudeva (2012), The great Arctic cyclone of August 2012, *Geophys. Res. Lett.*, **39**, L23709, doi:10.1029/2012GL054259.

Steele, M., J. Zhang, D. Rothrock, and H. Stern (1997), The force balance of sea ice in a numerical model of the Arctic Ocean, *J. Geophys. Res.*, **102**(C9), 21,061–21,079.

Stroeve J. C., M. Serreze, M. Holland, J. Kay, J. Maslanik, A. Barrett (2012), The Arctic's rapidly shrinking sea-ice cover: a research synthesis. *Clim. Chang*, **110**, 1005–1027. https://doi.org/10.1007/s1058 4-011-0101-1.

Terenzi, J., M. T. Jorgenson, and C. R. Ely. (2014), Storm-surge flooding on the Yukon–Kuskokwim Delta, Alaska. Arctic 67:360–374.

Ulbrich, U., and M. Christoph (1999), A shift of the NAO and increasing storm track activity over Europe due to anthropogenic greenhouse gas forcing. *Clim. Dyn.*, **15**, 551-559.

Yang, J., J. Comiso, R. Krishfield, and S. Honjo (2001), Synoptic storms and the development of the 1997 warming and freshening event in the Beaufort Sea, *Geophys. Res. Lett.*, **28**, 799–802, 2001, doi:10.1029/2000JC000583.

Yang, J., J. Comiso, D. Walsh, R. Krishfield, and S. Honjo (2004), Storm-driven mixing and potential impact on the Arctic Ocean, *J. Geophys. Res.*, **109**, C04008, doi:10.1029/2001JC001248.

Yin, J. H. (2005), A consistent poleward shift of the storm tracks in simulations of 21st century climate, *Geophys. Res. Lett.*, **32**, L18701, doi:10.1029/2005GL023684.

Yu, Y., G. A. Maykut, and D. A. Rothrock (2004), Changes in the thickness distribution of Arctic sea ice between 1958-1970 and 1993-1997, *J. Geophys. Res.*, **109**, C08004, doi:10.1029/2003JC001982.

Zhang X., and Coauthors (2004), Climatology and inter-annual variability of Arctic cyclone activity: 1948–2002. *J. Clim.*, **17**(12), 2300–2317. https://doi.org/10.1175/1520-0442(2004)017<2300:caivoa>2.0.co;2.

Zhang X., and Coauthors (2008), Recent radical shifts of atmospheric circulations and rapid changes in Arctic climate system. *Geophys. Res. Lett.*, **35**, L22701, https://doi.org/10.1029/2008gl035607.

Zhang, J., R. Lindsay, A. Schweiger, and M. Steele (2013), The impact of an intense summer cyclone on 2012 Arctic sea ice retreat, *Geophys. Res. Lett.*, **40**, doi:10.1002/grl.50190.

Chapter 2 Two Intense Arctic Storms Occurred in Summer 2016 and their Impacts on Melting Process of Sea Ice[1]

Abstract

Climate analyses of the Arctic have suggested an intensification of Arctic storm activities. Unusually intense storms, which have occurred preceding extreme sea ice loss or surface warming events, have been more frequently observed during recent decades and may suggest their important role in rapid Arctic climate change. However, the underlying physical processes and mechanisms have not been well investigated and understood. In this study, we examine how the storm impacts the state of sea ice and upper ocean by employing the in-situ observations during the 2016 Arctic expedition of the ice-breaking R/V Araon. Storms have an overall cooling effect under the background of moderate warming over the air-ice interface. Gradually increased surface winds enhance the Ekman pumping and causes the Pacific-origin warm water concentrated under the Surface Mixed Layer (SML). As the storm approaches, a rapid surface wind enhancement stimulates strong mixing between SML and Pacific-origin warm water, which results in a noted upper-ocean warming and, in turn, an increase in ocean-to-sea ice heat flux, larger than the net cooling effect of the storm. As a consequence, the sea ice decline accelerated.

---

[1]Peng L., J. H. Kim, X. Zhang, K. Cho, B. M. Kim, S. J. Park, Z. Wang, and Z. Xie. In Preparation for *Geophysical Research Letters*, Two Intense Arctic Storms Occurring in Summer 2016 and their Impacts on Melting Process of Sea Ice.

2.1 Introduction

Storm tracks tend to have a poleward shift as a result of climate change (Zhang et al., 2004; Yin 2005; Chang et al., 2012), and strong storms have been more frequently highlighted. Several case studies have examined extreme Arctic storms and have commonly shown that storms accompanied a rapid sea ice decline after their invasion during the summer (Simmonds and Rudeva, 2012; Zhang et al., 2012; Parkinson and Comiso, 2013). Statistical analysis has also suggested that intense summer storms potentially facilitate the melting of sea ice (Simmonds and Keay, 2009; Kriegsmann and Brümmer, 2014). Sea ice plays an important role in the polar energy balance and water cycles (e.g. Zhang et al., 2013; Vihma, 2014), therefore, accurate knowledge about storm impact on sea ice and the upper ocean is essential for better understanding of the Arctic climate system and making more accurate predictions.

Due to complicated air-ice-ocean interactions, a complete picture of the impact of the storm on sea ice has yet to be established. Studies have shown that storm invasions may transport warm and moist air into the Arctic (e.g., Sorteberg and Walsh, 2008; Zhang et al., 2013) and have a further impact on the precipitation and cloud cover (e.g., Kay et al., 2008). Additionally, high surface winds induced by storms play an important, but an enigmatic role in controlling sea ice mass balance and upper ocean structure. The direct impact of high winds is driving sea ice motion (e.g., Ogi et al., 2010). It also separates the main ice pack into fragments, which are more vulnerable and sensitive to the perturbed external forcings (Parkinson and Comiso, 2013). Observational evidence shows that high surface winds may enhance the oceanic upwellings (Pickart et al., 2009) and result in an upward heat transported into the bottom of the Surface Mixed Layer (SML) during the spring, fall, and winter seasons (Jackson et al., 2010; Jackson et al., 2012; Steele and Morison, 1993; Yang et al., 2001; Yang et al., 2004). However, due to

the sea ice melting in summer, a strong oceanic stratification forms a pycnocline, which tends to prevent the subsurface heat transported upward into the SML (Aagaard et al., 1981).

Summer storms are more numerous, longer-lived, but less intense than winter storms (Zhang et al., 2004). There are some knowledge we gained from previous observational and modeling studies, including the storm-induced upper ocean mixing over the Chukchi Sea was found reached 40 m deep during the summer (Woodgate et al., 2005), rapid sea ice melting during the storm period was largely due to the bottom melting (Perovich et al., 2007; Zhang et al., 2012). The extent to which the sea ice was modified by storm-induced upward heat transport during the summer, especially the details about the process of this upward heat transport and the mixing are still not clear. Over the Chukchi Sea, sea ice changes are remarkable during the summer season (Parkinson et al., 1999; Comiso et al., 2008; Yoshizawa et al., 2015) and are closely related to the heat inflow, which typically reaches the maximum from the Bering Strait in August and September (Serreze et al., 2016). The northward warm water inflow from the North Pacific Ocean provides important subsurface heat reservoirs (Weingartner et al., 2005; Shimada et al., 2001; Shimada et al., 2006; Woodgate et al., 2010; Woodgate et al., 2015) that may contribute to changes in sea ice mass and energy balance (Maykut and Untersteiner, 1971).

Besides the above listed longer-term oceanic and atmospheric forcing parameters, we need to consider physical processes of intense air-ice-ocean interactions during the storm period as a synoptic time-scale processes for a more complete understanding. We have addressed this question by using ship-borne and remote sensing measurements of ocean, sea ice, and atmosphere. Direct measurements during storm processes have been rare, especially in sea ice-covered regions. Our study can contribute to filling this gap using in-situ atmosphere and ocean

observations close to the area of the 2016 storm center. Along with satellite-derived products, we will provide a more comprehensive picture of how storm-associated rapid surface wind speed change caused upward heat transport. We also showed that the entrained warm water was sufficient to cause a significant reduction of sea ice.

2.2 Data and Method

The 2016 Arctic expedition was conducted in the Chukchi Sea and East Siberian Sea using the Korean icebreaking research vessel (IBRV) Araon. During its first leg (5 August to 21 August), Araon voyaged in the ice-covered region over the Chukchi and East Siberian seas. A two-day ice camp was deployed at the southern tip of the Mendeleev Ridge during 14-15 August 2016. In this study, we define a region from 65 ^{o}N to 82 ^{o}N and from 158 ^{o}E and 148 ^{o}W as the observational area (OA), which is bounded by the blue dashed lines shown in Figure 1a-d. Surface meteorological observations were continuously operated on Araon. At the foremast observational platform (~21 m above sea level), air temperature and humidity were measured by the Vaisala HMP155 thermohygrometer housed in a passively ventilated Campbell URS1 shield and four components of net radiation were measured by the CNR4 net radiometer. A barometric sensor (Vaisala, Helsinki, Finland, model PTB110) was installed at the lower part of the foremast (~12 m above the sea level). The aforementioned instruments were interrogated every second. Wind measurements were based on a sonic anemometer at the radarmast (~33 m above sea level), and a conversion to the true wind was conducted afterward. The ice temperature was obtained from the ice mass balance buoy (IMB) deployed through sea ice (depth of 2 m) at the ice camp site, which was located near 78 ^{o}N, 177 ^{o}W during the storm period. The IMB measured the 5-m vertical temperature profile from the near-surface air to the

underlying upper-ocean. The vertical hydrological structure of the water column was obtained from the SeaBird (SBE-911) CTD profiler. During 5-21 August, there were 36 CTD observations conducted.

The surface atmospheric conditions were examined using the European Centre for Medium-Range Weather Forecasts (ECMWF) Interim Reanalysis (ERA-Interim) dataset (Dee et al., 2011). The spatial and temporal resolution of the reanalysis data is $0.75^{o}\times0.75^{o}$ in latitude and longitude and 6-hourly in time respectively. We used the automatic storm tracking algorithm, which was also used by Zhang et al., (2004), to detect storms based on the ERA-Interim dataset. Briefly, all the low-pressure centers were identified based on the mean sea level pressure field at each 6 hourly time step. Storm tracks were obtained by linking all identified centers successively. The sea ice concentration is derived from two datasets. The total sea ice area within the OA is estimated based on the Bootstrap Sea Ice Concentrations from Nimbus 7 scanning multichannel microwave radiometer (SSMR) and the Defense Meteorological Satellite Program Special Sensor Microwave Imager (SSMI), and the Special Sensor Microwave Imager/Sounder (SSMIS), version 3 dataset (Comiso, 2017). We used the daily sea ice concentration data available from the National Snow and Ice Data Center (NSIDC) with a 25 km horizontal resolution. The spatial distribution of the sea ice concentration is examined based on the Advanced Microwave Scanning Radiometer 2 (AMSR2) using Arctic Radiation and Turbulence Interaction Study (ARTIST) sea ice algorithm (ASI), which has the spatial resolutions of 6.25 km (ASI6k).

2.3 Development of Two Highlighted Storms

The storm track and the location of the Araon are shown in Figure 1a-f. The first storm was identified as a weak surface low pressure center over Novaya Zemlya on 00UTC 13 August near 73 °N, 49 °E (Figure 1a). It propagated northeastward into the central Arctic through the East Siberian Sea and merged with a preexisting storm on 15 August (Figure 1b), during which the first storm reached its shortest distance toward the location of the Araon. The surface observations from the Araon captured the minimum pressure (983 hPa) during this period (Figure 1h). As the storm moves northward during 15 August, the distance between the storm center and the Araon increases, and the storm center pressure also gradually increases. After the merging process, the first storm reached the minimum central pressure (967 hPa) at 00UTC 16 August (Figure 1c), which is a similar magnitude to the central pressure of the 2012 Great Arctic Storm (Simmonds and Rudeva, 2012; Yamagami et al., 2017). The first storm idles on 16 August and further moves northward reaching the most northern location at 12UTC on 16 August and turned southwestward later. From 06 UTC 18 August, the storm veers eastward until it finally merges with the second storm at 12 UTC 19 August (Figure 1f), and the total duration of the first storm is 7 days. The second storm is first identified at 18 UTC 17 August near 69 °N, 171 °E (Figure 1d), and it propagates northeastward through the OA. The second storm moves quickly toward the location of the Araon on 17 August and obtains its minimum distance from Araon on 18 August. It further moves northward and merged with the first storm (Figure 1f), reaching a minimum central pressure of 971 hPa is obtained at 00 UTC on 20 August. During the same period, Araon observes the second minimum surface pressure on 19 August (Figure 1h). The storm's central pressure keeps increasing afterward, and the second storm merges with a newborn storm over the Novaya Zemlya on 22 August (not shown).

2.4 The Sea Ice Variations During the Storm Period

Based on the ASI6k dataset (Section 2.2), we depict the spatial distribution of the sea ice concentration before, during, and after the storm passage on Figure 2a-f. On 13 August (Figure 2a), a large ice pack extends meridionally over the west flank of the Mendeleev Ridge before the first storm is identified. The ice edge on the right-hand side of the ice pack sits along the east flank of the Chukchi Borderland. This large ice pack directly connects to the main ice pack, and it is ~20% of the total ice area over the entire Arctic. Two ice-opening areas are formed over the Chukchi Abyssal Plain and the Mendeleev Abyssal Plain on 13 August (Figure 2a). A dramatic change of the ice pack is found after the invasion of storms (Figure 2f). The ice-opening area over the Chukchi Abyssal Plain extends further southward into part of the Herald Canyon, while the ice opening area over the Mendeleev Abyssal Plan moves westward and extends southward approached the northern tip of the Chukchi Borderland. Both opening areas became much broader and they only separate by ice fractures in between. The ice edge on the right-hand side shows a slightly westward retreatment, while a large eastward retreatment is observed on the left-hand side of the ice edge. According to the ice pack movements, we may deduce that the whole ice pack advected westward, which is the same as the prevailing surface wind direction (Figure 2a-f) and agree with our IMB data.

By focusing on the ice pack in the central area of our selected OA, sea ice loss due to large scale divergence is not expected to have a large impact on the total sea ice area, but rather the thermodynamic processes. Figure 2g shows a comparison of the total sea ice area within the OA between the 2016 storm and climatological condition. The climatology was derived by averaging the sea ice area from 2000 to 2016. This period includes 2007 and 2012 when sea ice

area reached its extremely low values. The climatological total sea ice area shows a linearly decreasing trend (0.02 km^2/day) throughout the storm period. On 13 and 14 August 2016, a similar decreasing rate is found, and the total sea ice area maintained about 10% lower than the climatological value until 15 August. As the first storm approaches, the total sea ice area decreases to 80% of the climatological value within three days, which also corresponds to a large sea ice decreasing rate (Figure 2h).

2.5 Storm Impact on the Sea Ice Energy Balance

To understand the storm impact on sea ice variations, we estimated the partitioning of the daily energy balance among different components at the air-ice interface (Figure 3a) including the net shortwave and longwave fluxes (F_{SW} and F_{LW}), the net sensible and latent heat fluxes (F_S and F_L), and the net total energy flux (F_{Net}). Details of the flux calculation and calibrations of the surface observations are summarized in Appendix 2.11.

Storm induced clouds play a complex role in regulating F_{Net}. As variations in F_{LW} due to sea ice and ocean skin temperatures variations are small, changes in the F_{LW} shown in Figure 3b mainly reflect variations of the downward longwave (LW) fluxes. At the air-ice interface, the dominant heat source available for sea ice melting was provided by F_{SW} with the magnitude span from 50 W/m^2 to 120 W/m^2. On 15 August, the sun is obscured by optically thick clouds (Figure 3c). Compared with that on 14 August, the downward shortwave (SW) fluxes were reduced by 22.12 W/m^2, while the downward LW fluxes was still negative and only increased by 2.21 W/m^2. Starting from 17 August, the sky becomes partially opened and finally becomes completely clear on early 21 August as the second storm moves away. From 19 August to 21 August, the downward SW fluxes increased by 63.33 W/m^2 while the downward LW only

decreased by 16.33 W/m^2 within the three-day period. Therefore, variations in cloud amounts have larger impact on reducing downward SW than enhancing downward LW fluxes for this storm case.

In addition to cloud fraction effects, decreasing ice concentration (Figure 2) tends to cause increasing F_{SW} due to the ice-albedo feedback. On both 14 and 19 August, the sky is partially covered by clouds (Figure 3c), and the downward SW fluxes have similar magnitudes, 93.99 W/m^2 and 95.07 W/m^2 respectively. The ice concentration, on the other hand, linearly decreased by 38.62%, which corresponded to a 9.41 W/m^2 decrease of the upward SW fluxes within 6 days. Thus, this magnitude is comparable to the cloud impact on downward LW fluxes but much smaller than the downward SW flux variations. As the sea ice concentration gradually decreases and the sky becomes clear, less energy is received over the sea ice surface and more energy has been absorbed by the ocean (Figure 3b).

Both the first and the second storms induce strong surface winds (daily average wind speed exceed 11 m/s) on 15 16, and 19 August (Figure 1g). The strong southwesterly winds induce warm continental air advection on 15 and 16 August. The horizontal advection causes surface warming (Figure 1g), which results in positive F_S (Figure 3a). Unlike August 19, the southwesterly wind causes the continental air mass to move over a longer distance over the ocean on 15 and 16 August, allowing the warm air to gain moisture from the ocean surface. Although the sign of F_L is still negative, it increases 5.1 W/m^2 on 15 August compared with 14 August. On the other hand, the strong southerly winds observed on 19 August directly brings the continental dry air to the location of Araon through a much shorter pathway causing 13.95

W/m^2 decreases of the F_L compared with one day earlier. The evaporative cooling occurred due to a large dew point depression of the dry continental air over the moist ocean.

In general, the small temperature differences between the near surface air and the skin air temperatures suggests that F_S plays the smallest role in influencing the magnitude of F_{Net} compared with other components as shown by Figure 3b. The contribution from F_L plays a larger role compared with F_S, but its influence depends on the pathway of the air mass and the distance towards the source region. A longer distance transport due to storm over the ocean surface allows the warm continental air to carry more humid air over the inner ocean surface compared with a shorter pathway. Through the early period of this process, or in another words, if the pathway is too short, the continental dry air advection will cause surface energy loss due to evaporation.

Based on CTD observations, we further estimate the ocean-to-ice heat flux (F_{io}) and the ice bottom melting rate ($\frac{\delta hio}{\delta t}$). Through our ice camp measurements (not shown), the conductive heat impacts on the ice energy balance is negligible during the storm period, therefore, we do not consider its effect on F_{io} and $\frac{\delta hio}{\delta t}$ throughout this calculation. The estimated F_{io} and $\frac{\delta hio}{\delta t}$ are shown in Table 1 indicating that F_{io} has a larger magnitude than the F_{Net} over the air-ice interface. More energy flux received at the ice-ocean interface than at the air-ice interface is responsible for the rapid sea ice decrease during the storm period. The enhanced upward ocean heat flux also leads to a large magnitude of bottom melting rate ($\frac{\delta hio}{\delta t}$). According to the Table 1, strong F_{io} on both 15 and 19 August also was accompanied by high surface winds. In the next section, we will discuss physical processes causing a large F_{io} during the storm period.

2.6 The Upper Ocean Structure During the Storm Period

The upward heat flux was estimated based on the surface mixed layer (SML) temperature. We defined the SML temperature and salinity as an average between 5 m and 7 m to avoid the impact of diurnal variations near the open ocean surface (Zeng and Beljaars, 2005; Kawai and Wada, 2007). Figure 4 shows the temperature and salinity profiles collected by two CTD groups. The first group (Figure 4a) is an average of the CTD profiles in station A and B, which were collected on 13 August. The second group is an average of CTD profiles in station C and D, which were collected on 16 August. Similarly, the third group (Figure 4b) combines CTD profiles in stations E and F, which were collected on 18 August and the last group combines the CTD profiles in stations G and H, which were collected on 19 August. Based on the surface winds and sea ice concentration, we estimate the Ekman velocity under a steady state assumption based on the classic Ekman theory via the procedures summarized in Appendix 2.11. Brown and black arrows in Figure 4a show the Ekman spirals on 13 August and 15 August respectively as the storm obtain its maximum wind speed during the first storm period on 15 August. The Ekman spirals for the second group is shown in Figure 4b based on data collected on 18 and 19 August.

On 13 and 16 August, the depth of the Ekman layer was shallow (~20 m) due to a relatively weak surface wind stress. The uniform temperature and salinity profiles within the SML suggest that the water is well-mixed. Friction tends to deviate currents within the SML pointing to the right-hand side relative to the surface wind direction and forming a net divergence within the Ekman layer. The divergence within the Ekman layer accompanies an upward mass transport but is confined within the halocline, therefore, the lifted water is concentrated near the bottom

of the SML forming a thin layer with a strong static stability. Similar to the schematic water mass structure shown by Proshutinsky and Johnson (1997), the Pacific-origin water mass tends to form a dome over the center of a cyclonic circulation and deepens over surrounding areas. The lifting over the center area is evidenced by an abrupt increase of the salinity underneath the SML (Figure 4a). A stair-like jump, indicating the shoaling of the Pacific-origin warm water, can be found on both the temperature and salinity profiles beneath the SML. The large variations on the temperature between 30 to 80 m (Figure 4a) were possibly due to inflow of the Alaskan Coastal Water (ACW, salinity range from 31 to 32), which replaced the summer Bering Sea Water (sBSW, salinity range from 32 to 33). Climatologically, the ACW flows through the coastline of Alaska into the Barrow Canyon (Paquette and Bourk, 1974), while the sBSW flows primarily through the Hope Valley into Herald Canyon (Winsor and Chapman, 2004) and through Hanna Canyon into the Chukchi Borderland (Weingartner et al., 2005; Pickart et al., 2016). On 13 August, the temperature and salinity at this level is relatively cold and salty indicating the water mass is dominated by sBSW. As the first group of CTD profiles are collected at the boundary between the sBSW and ACW controlled areas (Steele et al., 2004; Shimada et al., 2006), storms potentially enhance convergence at this level causing the lifting of the Pacific-origin water mass and westward extension of the ACW. As shown by the CTD profiles from 16 August, the temperature increases, and the salinity decreases at this level (30~80 m) suggesting ACW water becomes dominant on 16 August. Comparing it with the second group of the CTD profiles (Figure 4b), which are collected further eastward relative to the first CTD group, the Pacific-origin water mass is now dominant by ACW on both 18 and 19 August. The depth corresponding to the maximum temperature increased from ~50 m to ~60 m.

Compared with the pre-storm condition on 13 and 18 August, storm induced strong shear within the SML during the storm period, which enhances the mixing between Pacific-origin warm water and cold fresh SML water. Strong mixing between the cold fresh SML water and the warm Pacific-origin water underneath causes an increase of the SML temperature on 16 August (Figure 4a) and 19 August (Figure 4b) corresponding to an excessive ocean to ice heat flux, and in turn a rapid sea ice decrease (Table 1). Since the sea ice cover has reduced for the second CTD group (Table 1), an enhanced downward momentum flux causes the Ekman layer depth to increase from 18 m to 29 m on 19 August even though the surface wind speed is slightly decreased. The SML temperature increased by $0.21\ ℃/day$, which is larger than that caused by the solar heating ($0.02 - 0.09\ ℃/day$). The strong upward heat flux causes a decreasing of sea ice, a freshening of the SML, and in turn, an enhancement of the stratification of the halocline. Due to the strong stratification and a fast transition from a high wind to a quiescent condition, the warm fresh water is likely confined within the SML and the upward transport of the saltier Pacific warm water is prohibited after the passage of the storm.

2.7 Discussions and Summary

During the first storm period, a rapid sea ice decline is observed. Sea ice receives a moderate amount of heat from the atmosphere. The storms caused an overall cooling effect for sea ice. Taking the variations of cloud fraction, sea ice concentration, and horizontal advection of the continental dry air into account, our result suggests that the largest contribution to the heat flux decrease comes from the downward SW fluxes due to storm-induced cloud formations. If we estimate the ratio of the daily flux variations due to other components to the downward SW flux, we find that the cloud formation leads to a 10%-26% enhancement of the downward LW

flux, while only 2-7% of the energy gains are due to the sea ice decline during the storm period. Additionally, the continental dry air advection further induces 22%-79% energy lost due to the evaporation. The solar radiation absorbed by the upper ocean causes warming within the SML and such impact may further enhance as the sea ice declines afterwards. However, the surface warming due to solar heating is not sufficient to explain the observed rapid temperature increase during the observation period. Under the background of moderate energy gain at the air-ice interface, storms cause less energy received during the storm period at the air-ice interface. Therefore, it is not likely the mechanism triggering the initial rapid sea ice decline during the storm period.

Further investigations on the sea ice bottom energy budgets indicate a strong upward ocean-to-ice heat flux, which exceeds the overall heat received at the sea ice surface and the energy lost due to the storm invasion. Storm-induced strong winds and large changes of the surface wind speed in a short period are the main drivers for the SML warming and rapid sea ice decrease. As the storm approached, a gradual increase of the surface wind causes a shoaling of the subsurface Pacific-origin warm water due to the Ekman pumping effect. Storms lead to a surface divergence within the SML, and an upwelling underneath it invokes a lifting of the warm Pacific-origin warm water underneath the upper halocline. The lifted warm water tends to be concentrated underneath the SML forming a stair-like structure on both the temperature and salinity profiles. As the storm approached, a rapid increase of the surface wind deepens the SML, and the strong shear at the bottom of SML causes the concentrated warm water to diapycnal (i.e., across density gradients) mixed with the cold fresh water that was originally within the SML (Rainville et al., 2011). Such mixing processes tend to raise the SML temperature and salinity. Sea ice is not only influenced by the warming of the SML, but also

alters the magnitude of it. If the sea ice is present during the SML warming events, it tends to impede the warm SML water from being directly exposed to the cold atmosphere and releasing its heat. The warm SML water, on the other hand, causes a rapid sea ice decline, which tends to produce fresh water and reduces the SML salinity. Within the SML, if the freshening caused by the melted ice dominates the salinity raising caused by mixing with the saltier Pacific-origin water, an enhancement of the static stability within the upper halocline tends to inhibit further Ekman pumping produced upwellings, causing the SML to be isolated from the subsurface heat source. Dynamically, sea ice tends to reduce the momentum flux from the air into the ocean. As sea ice decreases, a stronger momentum flux associated with a deeper Ekman layer potentially enhanced mixing between the cold SML water with a deeper Pacific-origin warm water source, which, in turn, facilitate sea ice melting.

2.8 Figures

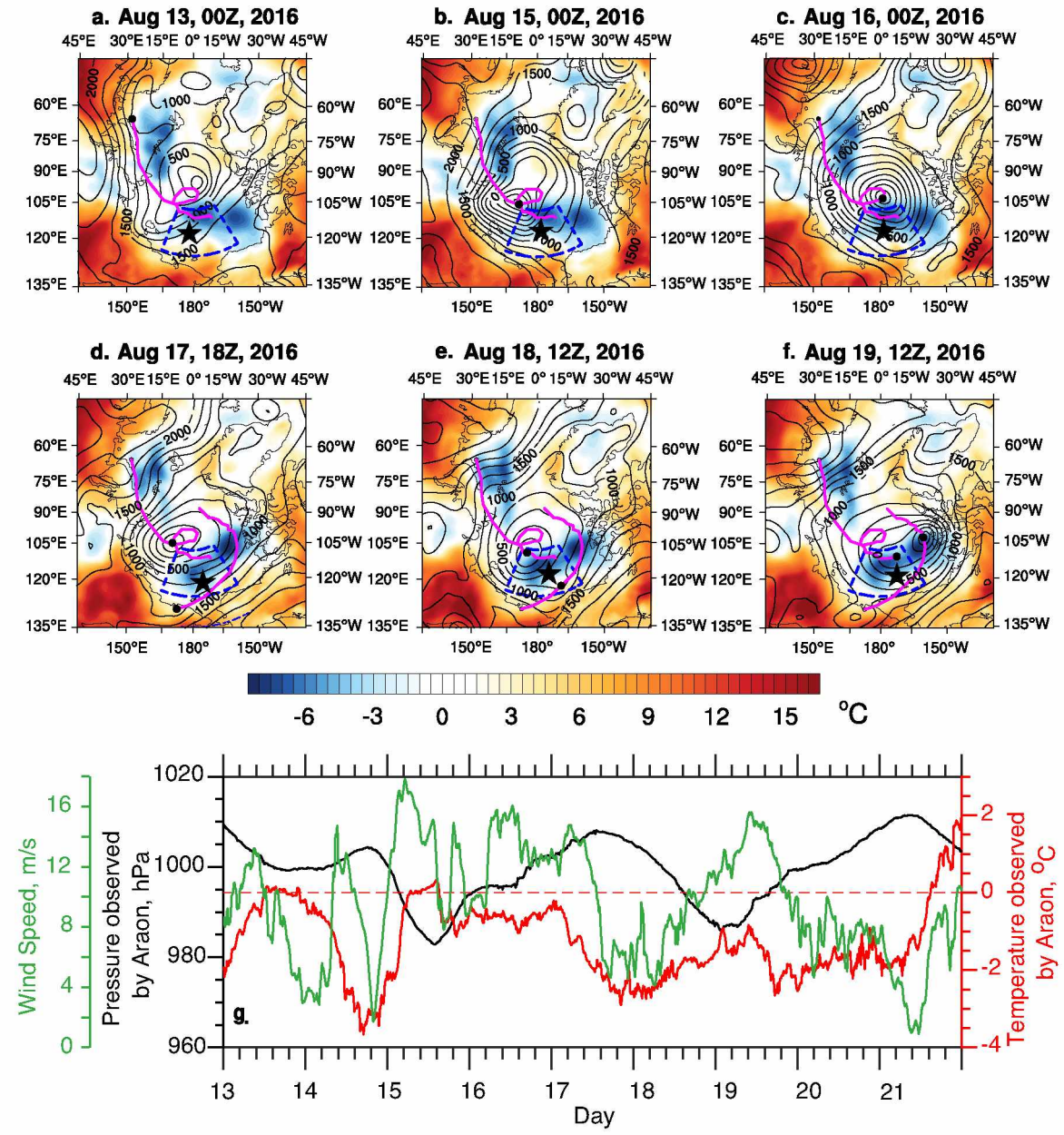

Figure 1. The mean sea level pressure (black solid contours) and surface air temperature (color scale shading) for six selected periods (a to f) based on the ERA-Interim reanalysis data. Two storm tracks are also shown by the solid magenta lines. The storm center location is shown by the black dot along the tracks. The location of Araon is indicated by the black star. The blue dash line highlighted the observational area (See Text). Time series of (g) the surface pressure (black line), temperature (red line), and the true wind speed (green) observed by Araon.

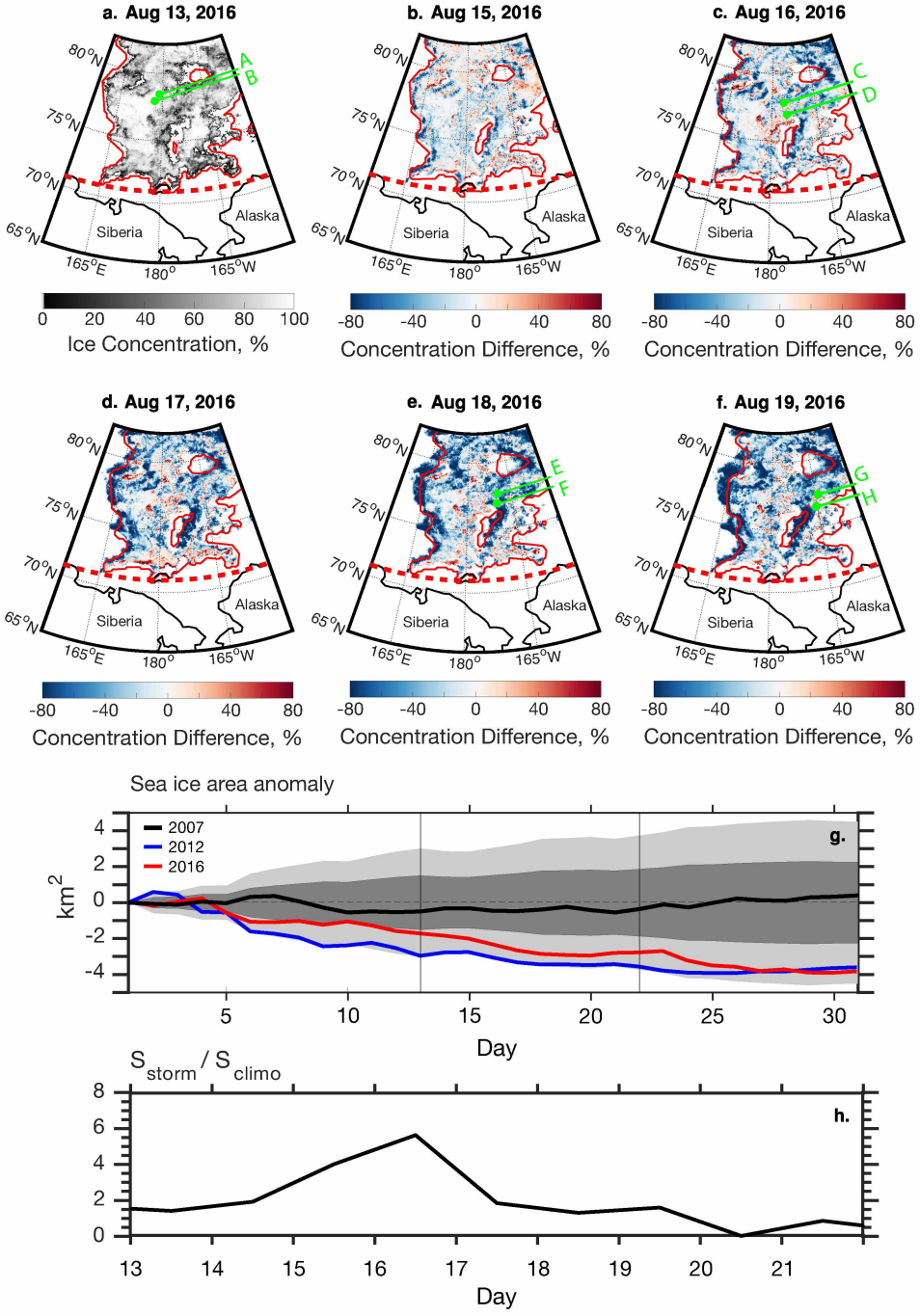

Figure 2. The sea ice concentration on (a) 13 August. The concentration difference between 13 August and (b) 14 August, (c) 16 August, (d) 17 August, (e) 18 August, and (f) 19 August. The ASI6k sea ice concentrations are shown in a grey scale, concentration differences are shown in a blue-white-red scale, and red contours represent the sea ice extent by the SSM/I dataset. The southern boundary of the analysis box is shown by the thick red dashed line. Time series of (g) the total sea ice area anomaly calculated by the SSM/I dataset over the area for the 2016 (red line), 2012 (blue line), 2007 (black line), and the climatology condition (red

Figure 2. (Continued) line, averaged between 2000-2016), and (h) the ratio between the total sea ice area decline rate under the storm and climatological condition.

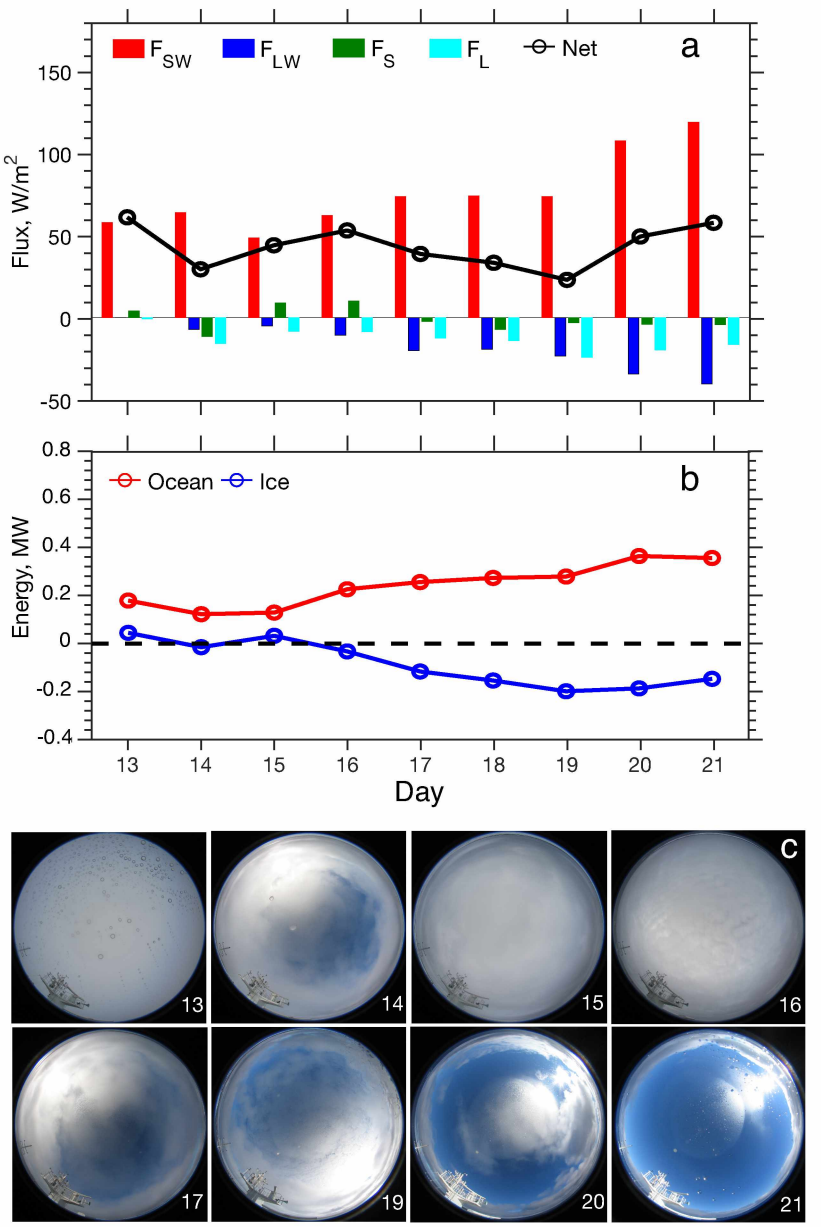

Figure 3. Daily averaged (a) sea ice concentrations, surface wind velocity at standard height under neutral condition, and (b) the total energy received over the open water (red) and sea ice (blue). (c) Cloud conditions are shown by selected all sky camera images with the number on the bottom-right corner indicating the days in August 2016.

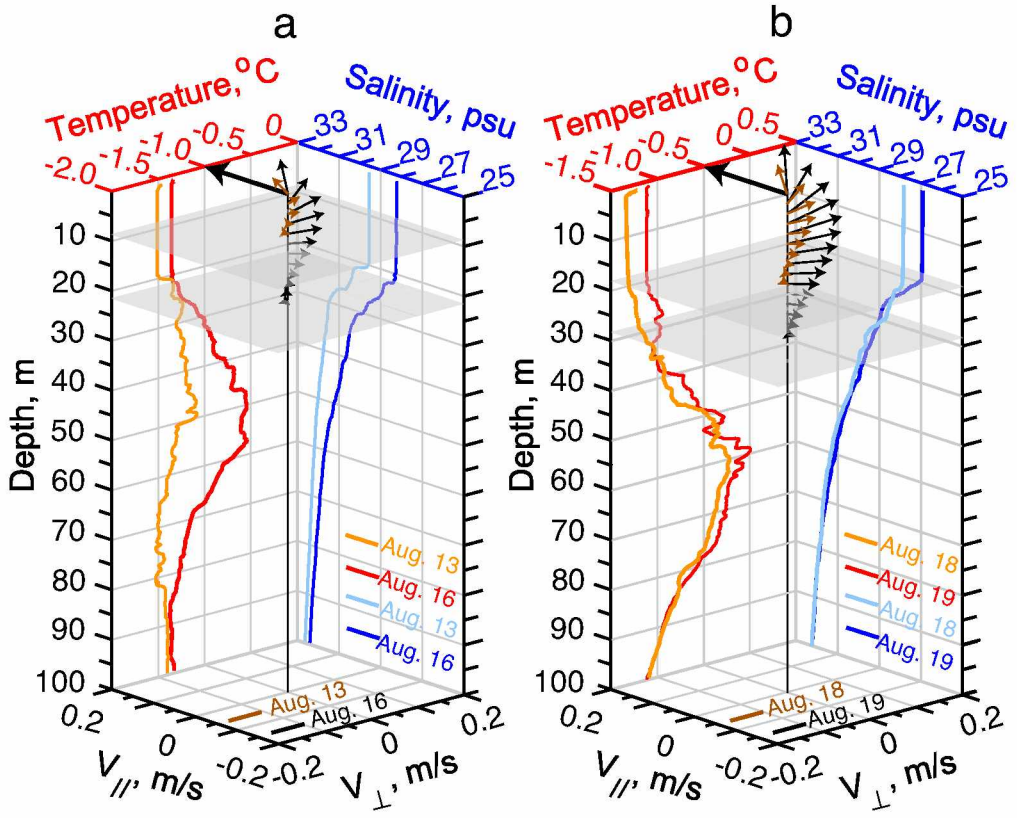

Figure 4. The upper ocean structures according to (a) the CTD profiles collected during 13 and 16 August, and (c) CTD profiles collected during 18 and 19 August. Lines shown on the left (right) hand side surface represent temperature (salinity) vertical profiles scaled by the red (blue) abscissa at the top. The thick horizontal black arrow at the top surface indicate the surface wind direction, and the thin horizontal arrows at each vertical level below represent the derived Ekman velocity profiles with scales shown on the bottom surface in black. Brown (black) arrows indicate currents calculated based on earlier (later) times (see text). The grey shaded planes represent the Ekman depths.

2.9 Tables

Table 1. Upward heat flux and sea ice bottom-melting rate based on CTD observations

	Aug. 13	Aug. 16	Aug. 18	Aug. 19
T_{sml} (°C)	-1.48	-1.32	-1.29	-1.08
S_{sml} (psu)	29.53	28.27	27.85	26.97
U (m/s)	8.84	13.12	8.20	12.66
C (%)	86.31	60.10	27.63	20.53
F_{io} (W/m^2)	57.63	93.70	96.53	165.55
$\frac{\delta h_{io}}{\delta t}(cm/day)$	1.84	3.00	3.09	5.30

2.10 References

Aagaard, K., L. Coachman, and E. Carmack (1981), On the halocline of the Arctic Ocean, *Deep Sea Res.*, Part A, **28**, 529–545, doi:10.1016/0198- 0149(81)90115-1.

Chang, E. K. M., Y. Guo, and X. Xia (2012), CMIP5 multimodel ensemble projection of storm track change under global warming, *J. Geophys. Res.*, **117**, D23118, doi:10.1029/2012JD018578.

Comiso, J. C., C. L. Parkinson, R. Gersten, and L. Stock (2008), Accelerated decline in the Arctic sea ice cover, *Geophys. Res. Lett.*, **35**, L01703, doi:10.1029/2007GL031972.

Comiso, J. C. (2017), *Bootstrap Sea Ice Concentrations from Nimbus-7 SMMR and DMSP SSM/I-SSMIS, Version 3*. (Indicate subset used). Boulder, Colorado USA. NASA National Snow and Ice Data Center Distributed Active Archive Center. doi: https://doi.org/10.5067/7Q8HCCWS4I0R. (Date Accessed).

Dee, D. P., and Coauthors (2011), The ERA-Interim reanalysis: Configuration and performance of the data assimilation system, *Q. J. R. Meteorol. Soc.*, **137**, 553–597.

Jackson, J. M., E. C. Carmack, F. A. McLaughlin, S. E. Allen, and R. G. Ingram (2010), Identification, characterization, and change of the near-surface temperature maximum in the Canada Basin, 1993–2008, *J. Geophys. Res.*, **115**, C05021, doi:10.1029/2009JC005265.

Jackson, J. M., W. J. Williams, and E. C. Carmack (2012), Winter sea-ice melt in the Canada Basin, Arctic Ocean, *Geophys. Res. Lett.*, **39**, L03603, doi:10.1029/2011GL050219.

Kawai, Y., and A. Wada (2007), Diurnal sea surface temperature variation and its impact on the atmosphere and ocean: A review, *J. Oceanogr.*, **63**, 721–744.

Kay, J. E., T. L'Ecuyer, A. Gettelman, G. Stephens, and C. O'Dell (2008), The contribution of cloud and radiation anomalies to the 2007 Arctic sea ice extent minimum, *Geophys. Res. Lett.*, **35**, L08503, doi:10.1029/ 2008GL033451.

Kriegsmann, A., and B. Brümmer (2014), Cyclone impact on sea ice in the central Arctic Ocean: a statistical study. *Cryosphere,* **8**, 303–317, doi:10.5194/tc-8-303-2014.

Maykut, G. A., and N. Untersteiner (1971), Some results from a time dependent thermodynamic model of sea ice, *J. Geophys. Res.*, **76**, 1550–1575, doi:10.1029/JC076i006p01550.

Ogi, M., K. Yamazaki, and J. M. Wallace (2010), Influence of winter and summer surface wind anomalies on summer Arctic sea ice extent, *Geophys. Res. Lett.*, **37**, L07701, doi:10.1029/2009GL042356.

Paquette, R.G., and R.H. Bourke (1974), Observations on the coastal current of Arctic Alaska. *J. Mar. Res.*, **32**, 195–207.

Parkinson, C. L., D. J. Cavalieri, P. Gloersen, H. J. Zwally, and J. C. Comiso (1999), Arctic sea ice extents, areas, and trends, 1978–1996, *J. Geophys. Res.*, **104**(C9), 20,837–20,856.

Parkinson, C. L., and J. C. Comiso (2013), On the 2012 record low Arctic sea ice cover: Combined impact of preconditioning and an August storm, *Geophys. Res. Lett.*, **40**, 1356–1361, doi:10.1002/grl.50349.

Perovich, D. K., S. V. Nghiem, T. Markus, and A. Schweiger (2007), Seasonal evolution and interannual variability of the local solar energy absorbed by the Arctic sea ice–ocean system, J. *Geophys. Res.*, **112**, C03005, doi:10.1029/2006JC003558.

Pickart, R. S., and Coauthors (2009), Upwelling on the continental slope of the Alaskan Beaufort Sea: Storms, ice, and oceanographic response, *J. Geophys. Res.*, **114**, C00A13, doi:10.1029/2008JC005009.

Pickart, R. S., G. W. K. Moore, C. Mao, F. Bahr, C. Nobre, and T. J. Weingartner (2016), Circulation of winter water on the Chukchi shelf in earlySummer, *Deep Sea Res., Part II*, **130**, 46–75, doi: 10.1016/j.dsr2.2016.05.001.

Proshutinsky, A., and M. Johnson (1997), Two circulation regimes of thewind-driven Arctic Ocean, *J. Geophys. Res.*,**102**, 12,493–12,514.

Rainville, L., C. Lee, and R. Woodgate (2011), Impact of wind-driven mixing in the Arctic Ocean, *Oceanography*, **24**(3), 136–145, doi:10.5670/oceanog.2011.65.

Serreze, M. C., A. D. Crawford, J. C. Stroeve, A. P. Barrett, and R. A. Woodgate (2016), Variability, trends, and predictability of seasonal sea ice retreat and advance in the Chukchi Sea, *J. Geophys. Res. Oceans*, **121**, 7308–7325, doi:10.1002/ 2016JC011977.

Shimada, K., E. Carmack, K. Hatakeyama, and T. Takizawa (2001), Varieties of shallow temperature maximum waters in the Western Canadian Basin of the Arctic Ocean, *Geophys. Res. Lett.*, **28**, 3441–3444.

Shimada, K., and Coauthors (2006), Pacific Ocean inflow: Influence on catastrophic reduction of sea ice cover in the Arctic Ocean, *Geophys. Res. Lett.*, **33**, L08605, doi:10.1029/2005GL025624.

Simmonds, I., and K. Keay (2009), Extraordinary September Arctic sea ice reductions and their relationships with storm behavior over 1979–2008, *Geophys. Res. Lett.*, **36**, L19715, doi:10.1029/2009GL039810.

Simmonds, I., and I. Rudeva (2012), The great Arctic cyclone of August 2012, *Geophys. Res. Lett.*, **39**, L23709, doi:10.1029/2012GL054259.

Sorteberg, A., and J. E. Walsh (2008), Seasonal cyclone variability at 70°N and its impact on moisture transport into the Arctic. *Tellus A*, **60**, 3, 570–586, doi:10.1111/j.1600-0870.2008.00314.x.

Steele, M., and J. H. Morison (1993), Hydrography and vertical fluxes of heat and salt northeast of Svalbard in autumn, *J. Geophys. Res.*, **98**, 10,013, doi:10.1029/93JC00937.

Steele, M., J. Morison, W. Ermold, I. Rigor, M. Ortmeyer, and K. Shimada (2004), Circulation of summer Pacific haloclinewater in the Arctic Ocean, *J. Geophys. Res.*, **109**, C02027, doi:10.1029/2003JC002009.

Vihma, T. (2014), Effects of Arctic sea ice decline on weather and climate: a review, *Surv. Geophys*, **35**, 1175-1214, doi:10.1007/s10712-014-9284-0.

Weingartner, T. J., S. L. Danielson, and T. C. Royer (2005), Freshwater variability and predictability in the Alaskan Coastal Current, *Deep Sea Res., Part II*, **52**, 161–191.

Winsor, P., and D.C. Chapman (2004), Pathways of Pacific water across the Chukchi Sea: a numerial model study. *J. Geophys. Res.*, **109**, C03002. http://dx.doi.org/ 10.1029/2003JC0 01962.

Woodgate, R. A., K. Aagaard, and T. J. Weingartner (2005), A year in the physical oceanography of the Chukchi Sea: Moored measurements from autumn 1990-1991, *Deep Sea Res., Part II*, **52**(24–26), 3116–3149, doi:10.1016/j.dsr2.2005.10.016.

Woodgate, R. A., T. Weingartner, and R. Lindsay (2010), The 2007 Bering Strait oceanic heat flux and anomalous Arctic sea-ice retreat, *Geophys. Res. Lett.*, **37**, L01602, doi:10.1029/2009GL041621.

Woodgate, R. A., K. M. Stafford, and F. G. Prahl (2015), A synthesis of year-round interdisciplinary mooring measurements in the Bering Strait (1990-2014) and the RUSALCA years (2004-2011), *Oceanography*, **28**, 46–67, doi:10.5670/oceanog.2015.57.

Yamagami, A., Matsueda, M. and Tanaka, H. L. (2017), Extreme Arctic cyclone in August 2016. *Atmos. Sci. Lett.*, **18**: 307–314. doi:10.1002/asl.757.

Yang, J., J. Comiso, R. Krishfield, and S. Honjo (2001), Synoptic storms and the development of the 1997 warming and freshening event in the Beaufort Sea, *Geophys. Res. Lett.*, **28**, 799–802, 2001, doi:10.1029/2000JC000583.

Yang, J., J. Comiso, D. Walsh, R. Krishfield, and S. Honjo (2004), Storm-driven mixing and potential impact on the Arctic Ocean, *J. Geophys. Res.*, **109**, C04008, doi:10.1029/2001JC001248.

Yin, J. H. (2005), A consistent poleward shift of the storm tracks in simulations of 21st century climate, *Geophys. Res. Lett.*, **32**, L18701, doi:10.1029/2005GL023684.

Yoshizawa, E., K. Shimada, H. K. Ha, T. W. Kim, S. H. Kang, and K. H. Chung (2015), Delayed responses of the oceanic Beaufort Gyre to winds and sea ice motions: Influences on variations of sea ice cover in the Pacific sector of the Arctic Ocean, *J. Oceanogr.*, **71**, 187–197, doi:10.1007/s10872-015-0276-6.

Zeng, X., and A. Beljaars (2005), A prognostic scheme of sea surface skin temperature for modeling and data assimilation, *Geophys. Res. Lett.*, **32**, L14605, doi:10.1029/2005GL023030.

Zhang, J., R. Lindsay, A. Schweiger, and I. Rigor (2012), Recent changes in the dynamic properties of declining Arctic sea ice: A model study, *Geophys. Res. Lett.*, **39**, L20503, doi:10.1029/2012GL053545.

Zhang, X., J. E. Walsh, J. Zhang, U. S. Bhatt, and M. Ikeda (2004), Climatology and interannual variability of Arctic cyclone activity: 1948–2002, *J. Clim.*, **17**, 2300–2317.

Zhang, X., He, J., Zhang, J., Polyakov, I., Gerdes, R., Inoue, J., and Wu, P. (2013), Enhanced poleward moisture transport and amplified northern high-latitude wetting trend. *Nature Clim. Change*, **3**, 47-51, doi:10.1038/NCLIMATE1631.

2.11 Appendices

2.11.1 Surface Measurements Processing Steps

Our first task is to convert measurements from different platforms into a standard height via an iterative method described by Large and Yearger (2004). Through this step, we convert surface measurements collected at the foremast (21 m) to the level of radarmast (33 m) along with transfer coefficients by considering variations of the atmospheric stability.

The drag coefficient (C_D) and transfer coefficients for heat (C_H) and moisture (C_E) are given as a function of equivalent neutral 10 m wind speed (U_{N10m}).

$$1000 = \frac{2.7}{U_{N10m}} + 0.142 + \frac{U_{N10m}}{13.09} \tag{A1}$$

$$1000C_E = 34.6\sqrt{C_D} \tag{A2}$$

$$1000C_H = \begin{cases} 18.0\sqrt{C_D}, & SP > 0 \\ 32.7\sqrt{C_D}, & SP \leq 0 \end{cases} \tag{A3}$$

We first substitute the surface wind speed (U_{N10m}) collected at the level of radarmast ($z_u = 33\ m$) into Eq. A1 to calculate the guess values for C_{DG}, C_{HG}, and C_{EG}. The stability parameter is assumed to be neutral, SP $= \frac{z}{L} = 0$, in which L is the Monim-Obukhov length.

The initial turbulent scales are computed based on the guess values of the drag coefficients

$$u^* = \sqrt{C_{DG}}|U_{33m} - U_{0m}|, \tag{A4}$$

$$t^* = \frac{C_{HG}}{\sqrt{C_{DG}}}|\theta_{21m} - \theta_{0m}|, \tag{A5}$$

$$q^* = \frac{C_{EG}}{\sqrt{C_{DG}}}|q_{21m} - q_{0m}|, \tag{A6}$$

where $U_{0m} = 0\ m/s$. The surface air temperature $\left(\theta_{0m} = C \times \theta_{0m,ice} + (1 - C) \times \theta_{0m,ocn}\right)$ is weighted by the sea ice concentration (C). The ice concentration is based on ASI6k dataset and averaged within an arbitrarily selected analysis box (between 72 °N to 82 °N and 165 °E to 148 °W). The selection of the analysis box requires following considerations: (1) Since we combine all energy terms in estimating the net energy fluxes over the air-ice interface, daily averaged ship-borne measurements can be used to represent the mean properties within the analysis box, (2) the analysis box should be small enough that the CTD observations can represent the first-order approximation of the ocean properties within the box, (3) the analysis box should be large enough to include most CTD observations used in this analysis, and (4) the analysis box should also be large enough that sea ice dynamics should have a minimal impact on the averaged ice concentration during the storm period. According to our ice camp and the first level CTD observations, $\theta_{0m,ice}$ and $\theta_{0m,ocn}$ is set to equal 0 °C and -1.2 °C respectively. The surface air is assumed to be close to saturation (98%), and the specific humidity is given by

$$q_{0m,sat} = \frac{q_1 e^{(q_2/\theta_{0m})}}{\rho_a}, \tag{A7}$$

where $q_1 = 0.98 \times 640380\ kg/m^3$ and $q_2 = -5107.4\ K$.

The stability parameters at the level of radarmast (SP_{33m}) and foremast (SP_{21m}) are estimated separately by

$$SP(z) = \frac{\kappa g z}{u^{*2}}\left[\frac{t^*}{\theta_v} + \frac{0.608q^*}{0.608q(z)+1}\right], \tag{A8}$$

where the von Karman constant $\kappa = 0.4$ and g is the gravitational acceleration. Both θ_{21m} and q_{21m} are used to estimate the SP_{33m} and SP_{21m} at this step.

In a non-neutral condition ($\zeta \neq 0$), the integrated form of the dimensionless flux profiles of momentum

$$\psi_m(SP) = \begin{cases} -5 \cdot SP, & SP > 0 \\ 2ln\left(\frac{1+\chi^2}{2}\right) + ln\left(\frac{1+\chi^2}{2}\right) - 2\tan^{-1}(\chi) + \frac{\pi}{2}, & SP < 0 \end{cases} \tag{A9}$$

$$\psi_h(SP) = \begin{cases} -5 \cdot SP, & SP > 0 \\ 2ln\left(\frac{1+\chi^2}{2}\right), & SP < 0 \end{cases} \tag{A10}$$

where $\chi = (1 - 16 \cdot SP)^{1/4}$.

The 10m wind (U_{N10m}) is then calculated as

$$U_{N10m} = U_{33m} + \frac{u^*}{\kappa}\left[ln\left(\frac{33m}{10m}\right) - \psi_m(SP_{33m})\right]^{-1} \tag{A11}$$

We then substitute U_{N10m} into Eq. A1 to update the 10m neutral transfer coefficients and further shifted them to the same height as the radarmast.

$$C_{D,33m} = C_D \left[1 + \frac{\sqrt{C_D}}{\kappa}\left(ln\left(\frac{33m}{10m}\right) - \psi_m(\mathrm{SP}_{33m})\right)\right]^{-2} \quad \text{(A12)}$$

$$C_{H,33m} = C_H \frac{\sqrt{C_{D,33m}}}{C_D}\left[1 + \frac{C_H}{\kappa\sqrt{C_D}}\left(ln\left(\frac{33m}{10m}\right) - \psi_h(\mathrm{SP}_{33m})\right)\right]^{-1} \quad \text{(A13)}$$

$$C_{E,33m} = C_E \frac{\sqrt{C_{D,33m}}}{C_D}\left[1 + \frac{C_E}{\kappa\sqrt{C_D}}\left(ln\left(\frac{33m}{10m}\right) - \psi_h(\mathrm{SP}_{33m})\right)\right]^{-1} \quad \text{(A14)}$$

Both the temperature and the specific humidity at the level of foremast also shift to the level of the radarmast according to

$$\theta_{33m} = \theta_{21m} - \frac{t^*}{\kappa}\left[ln\left(\frac{33m}{10m}\right) + \psi_h(\mathrm{SP}_{33m}) - \psi_h(\mathrm{SP}_{21m})\right]^{-1} \quad \text{(A15)}$$

$$q_{33m} = q_{21m} - \frac{q^*}{\kappa}\left[ln\left(\frac{33m}{10m}\right) + \psi_h(\mathrm{SP}_{33m}) - \psi_h(\mathrm{SP}_{21m})\right]^{-1} \quad \text{(A16)}$$

The updated θ_{33m} and q_{33m} are used to replace θ_{21m} and q_{21m}, and the guess values for the transfer coefficients (C_{DG}, C_{HG}, and C_{EG}) with $C_{D,33m}$, $C_{H,33m}$, and $C_{E,33m}$ in Eq. A2 to recalculate the turbulent scales in the next iteration loop. Taking into account the possible stable conditions over the sea ice, we precede five iterations to obtain the U_{N10m}. Even over the sea ice, our calculation indicates three iteration loops is sufficient to obtain a steady U_{N10m}.

2.11.2 Surface Flux Estimation

To estimate the sea ice energy balance, we split the sea ice surface heat flux into seven terms, which are the downwelling/upwelling shortwave (F_{SWdn} and F_{SWup}) and longwave fluxes

(F_{LWdn} and F_{LWup}), sensible (F_s) and latent (F_l) heat fluxes, and the heat flux from ice/ocean interface (F_{io}). The sign convention is that positive heat fluxes correspond to energy gain of the sea ice.

Both F_{SWdn} and F_{LWdn} are directly measured from the foremast. The net shortwave (SW) and longwave (LW) radiations can be estimated from

$$F_{SW} = F_{SWdn}(1 - \alpha) \tag{A17}$$

$$F_{LW} = F_{LWdn} - \sigma(T_{stc}^4)\varepsilon \tag{A18}$$

The surface albedo ($\alpha = \alpha_{ice} \times C + \alpha_{ocn} \times (1 - C)$) is weighted by the ice concentration (C). The ocean and ice albedos are $\alpha_{ocn} = 0.06$ and $\alpha_{ice} = 0.7$ respectively. Variations on sea ice albedo, which ranges from 0.6 to 0.8 during the summer (Perovich et al., 2002; Perovich et al., 2007), does not play a significant role in our estimation of F_{SW} (Figure A1). The LW emissivity of the snow and sea ice (ε) equal to 1.0, and the Stefan-Boltzmann constant equals $\sigma = 5.67 \times 10^{-8}\ W/m^2/K^4$.

Both the sensible and latent heat fluxes are estimated according to the bulk formulae

$$F_S = \rho_{air} c_p C_{H,33m}(\theta_{33m} - \theta_{0m})|U_{33m}| \tag{A19}$$

$$F_l = \rho_{air} L C_{E,33m}(q_{33m} - q_{0m,sat})|U_{33m}| \tag{A20}$$

where $c_p = 1000.5\ J/kg/K$, and $L = 2.5 \times 10^6\ J/kg$ represent the air specific heat and the latent heat of vaporization respectively. Both Eq. A19 and Eq. A20 assume that the surface currents and sea ice motions can be neglected compared with the magnitude of $|\vec{U}_{\mathrm{N10m}}|$.

A comparison of surface energy terms from Araon observations and ERA-Interim reanalysis data averaged within the analysis box is shown in Figure A1. The ERA-Interim reanalysis data has larger net energy fluxes over the air-ice interface in general. Compared to the Araon observation, the ERA-Interim reanalysis data shows relatively good agreement in both the net shortwave and longwave fluxes, while both the sensible and latent heat fluxes show larger biases. Overall, this comparison gives us confidence when applying Araon observations to the entire analysis box.

To further quantify the ocean heat transport process, according to (Notz et al., 2003), the heat flux from ice/ocean interface F_{io} is parameterized as

$$F_{io} = \rho_w c_p c_h u_* (T_{SML} - T_f) \tag{A21}$$

where the seawater density ($\rho_w = 1025\ kg/m^3$), the heat capacity ($c_p = 4200\ J/kg/K$), the heat transfer coefficient ($c_h = 0.01$), and the frictional velocity ($u_* = 0.01\ m/s$) remained as constants. T_f represents the freezing temperature, which is estimated as a function of salinity and pressure from the CTD observation at the same level where we obtained the SML temperature as

$$T_f = -0.0575S + 1.710523 \times 10^{-3} S^{\frac{3}{2}} - 2.154996 \times 10^{-4} S^2 - 7.53 \times 10^{-4} p \tag{A22}$$

The T_f at SML is expected to be similar as the T_f near the ice/ocean interface. The salinity and pressure are represented by S and p respectively. A simple estimation of the sea ice bottom-melting rate can be obtained according to (Steele and Ermold, 2015)

$$\frac{\delta h_{io}}{\delta t} = \frac{F_{io}}{\rho_i L_i} \tag{A23}$$

where $\rho_i = 900\ kg/m^3$ is the density of sea ice and $L_i = 3 \times 10^5\ J/kg$ is the latent heat of fusion of the sea ice.

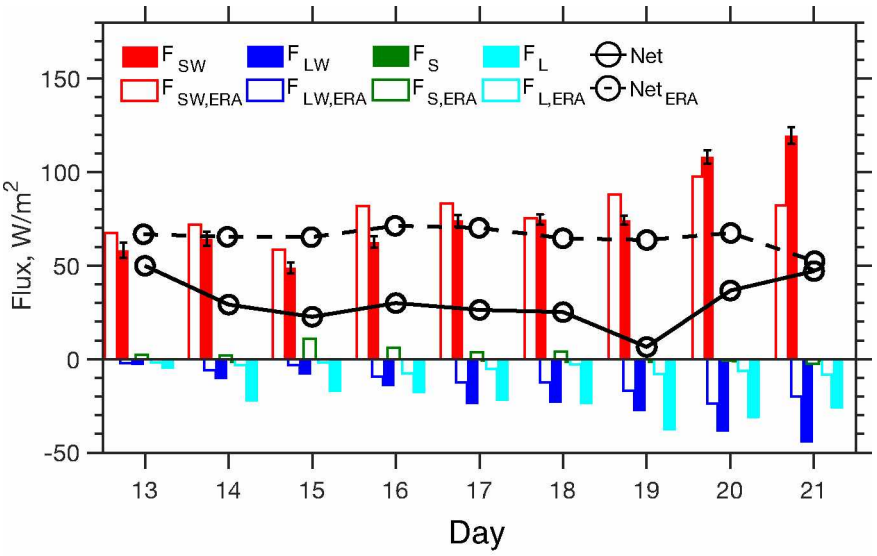

Figure A1. Comparison of measured energy fluxes to ERA-Interim reanalysis data for net shortwave flux (red), net longwave flux (blue), sensible heat flux (green), and latent heat flux (cyan). The solid and dash lines represent the net energy fluxes over the air-ice interface from measurements and ERA reanalysis data respectively. Filled and edged bars indicate fluxes from measurements and ERA reanalysis data respectively. Error bars represent the estimated uncertainties due to the sea ice albedo variations.

2.11.3 Estimation of the Ekman Depth

In a steady state, the horizontal equation of motion is

$$\frac{1}{\rho}\frac{\partial p}{\partial x} = fv + \frac{1}{\rho}\frac{\partial \tau}{\partial z} \tag{A24}$$

$$\frac{1}{\rho}\frac{\partial p}{\partial x} = -fu + \frac{1}{\rho}\frac{\partial \tau}{\partial z} \tag{A25}$$

where f is the planetary vorticity, and τ is the turbulent stress, which can be written as

$$\frac{\partial \tau}{\partial z} = K\frac{\partial^2 V}{\partial z^2} \tag{A26}$$

where the eddy viscosity (K) was assumed to vary with the surface wind speed (Pond and Pickard 2013) over the open water.

$$K = \frac{18.49\Omega\tau_0}{\rho_{air}C_d\pi^2} \tag{A27}$$

where the τ_0 represents the surface stress and Ω is the Earth's rotation rate. Equation A24 and A25 are satisfied for a steady, linear, and vertically homogeneous ocean. After canceling the geostrophic velocity components with the pressure gradient force, Equation A26 gives a homogeneous second-order linear differential equation of the ageostrophic Ekman velocity (V_E)

$$fV_E = -K\frac{\partial^2 V_E}{\partial z^2} \tag{A28}$$

The surface ($z = 0$) and bottom ($z = \infty$) boundary stresses are

$$\tau_{sfc} = C\tau_{ice} + (1 - C)\tau_{air} \tag{A29}$$

and

$$\tau_{bottom} = 0 \tag{A30}$$

respectively. In a short timescale and under the strong storm induce surface wind forcing; we only focus on the stress contributions from the air, which is simplified as

$$\tau_{air} = \rho_{air} C_D |U_{N10m}| U_{N10m} \tag{A31}$$

where C_D is the drag coefficient for the surface wind and ρ_{air} is the air density ($\rho_{air} = 1.22\ kg/m^3$). During the storm period, the values of U_{N10m} and C_D are based on Eq. 6 and Eq. 1 respectively.

The eddy viscosity (K) controls the Ekman depth (Ekman, 1905; Pond and Pichard, 1983), which was obtained by

$$D_E = \pi \sqrt{\frac{2K}{|f|}} \tag{A32}$$

for latitudes ϕ outside the tropical area ($|\phi| > 10°$). The magnitude of D_E can be regarded as the effective depth the wind driven current can reach.

In this study, we mainly focus on mechanisms causing rapid changes of D_E during the storm period. Generalized Ekman theory, which also considers the contribution of geostrophic currents to vertical shear, was developed and successively applied by several studies over lower latitudes (e.g. Cronin and Kessler, 2009, Wenegrat and Mcphaden, 2015). Over high latitudes, however, the geostrophic shear is expected to have less impact since it depends on a factor of 1/f (Cronin and Kessler, 2009). Regardless of the fact that there may have some evidences

shown by Figure A2 that mesoscale fronts (temperature gradient) may exist within both the SML and the level of halocline during the storm period, it is beyond the scope of this study and dataset to fully investigate vertical shear contributions associate with the thermal wind. Additionally, our study only considers K as a function of surface wind and remains a constant within the water column for simplicity.

2.11.4 General Hydrographic Patterns

The observational date of our CTD stations are summarized in Figure A2a. Overall, CTD detected temperature and salinity changes shown in Figure A2 combine both temporal and spatial variations. During the storm period, the ice pack and the prevailing surface wind direction move eastward (Section 4). The upstream SML temperature on the west flank of the ice pack was relatively cold and salty according to the CTD data collected around August 10^{th} (Figure A2bc). Before August 10^{th}, CTD stations extended from the Bering Strait northward into the Arctic through the Central Channel, which is one of three branches for the Pacific water entering the Arctic (Weingartner et al., 2005; Pickart et al., 2016). The other two main branches are the west and east branches for which the Pacific-origin water flow through the Hope Valley into Herald Canyon (Winsor and Chapman, 2004) and the coastline of Alaska into the Barrow Canyon (Paquette and Bourk, 1974) respectively. The observed SML temperature nearby Herald Canyon and the Central Channel are relatively warmer compared with its surroundings (Figure A2b).

The Pacific-origin warm water gradually deepens after it flows into the ice-covered area due to the fresh water released by the melting sea ice. We therefore define the Pacific-origin Temperature Maximum (PTM) as the first major temperature maximum underneath the SML.

The PTM was estimated for each CTD observation if it was present. A PTM is present if it satisfied the following four requirements: (1) The depth of PTM is below 7 m. (2) The difference between the depth of the PTM and the depth of the closest minimum temperature above the PTM is at least 5 m. (3) The temperature difference between the PTM and the minimum temperature above exceeds $0.2\ ^{o}C$. (4) The corresponding salinity at the level of PTM does not exceed 33 psu (Shimada et al., 2001), which ensures that the PTM we identified is not the Atlantic origin. Since our main purpose for defining PTM is to identify potential heat sources underneath the SML instead of the detailed constitution of water masses, the identified PTMs may include both the Alaskan Costal Water (ACW) and Chukchi Summer Water (CSW; Itoh et al., 2015; Gong and Pickart, 2016).

The spatial distribution of the temperature, salinity, and the depth of PTMs are shown in Figure A2def respectively. All PTMs are located over or toward the east flank of the MR and most of them are found where local sea ice concentrations exceed 15%. There is a clear temperature gradient of the PTMs from lower values in the southwest to higher in the northeast (Figure A2d). The PTMs over the northeast side of the ice edge were warmest and trapped within a depth between 50 and 60m (Figure A2f). The water mass near CTD station 28, 29, and 30 may originate from ACW after it swept anticyclonically by the Beaufort Gyre from the Barrow Canyon (Steele et al., 2004).

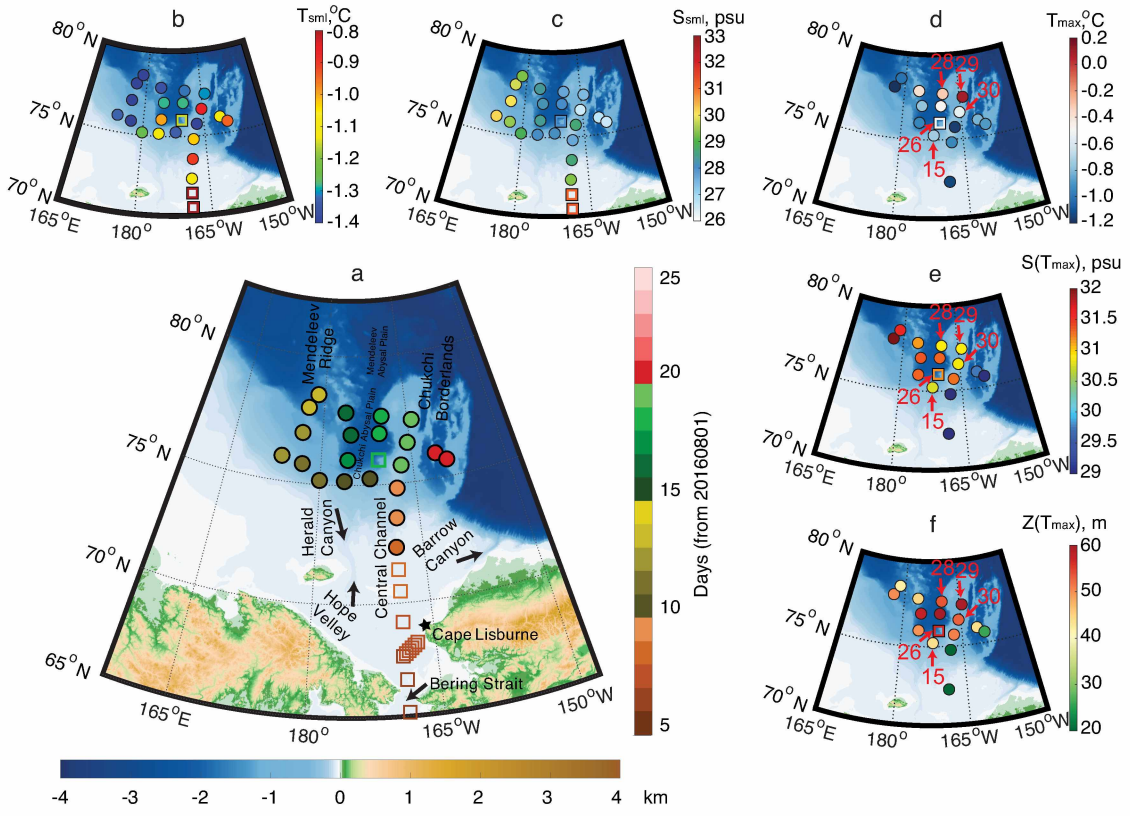

Figure A2. The locations of CTD stations used by this study were represented by a filled circle or an empty square if the corresponding ice concentrations exceed or less than 15% respectively. The colors of each points were coded on the right hand side of the figure as (a) the observational days, (b) the SML mean temperature, (c) the mean SML salinity, (d) the temperature at the PTMs, (e) the corresponding salinities at PTMs, and (d) the depth of PTMs. The CTD station numbers mentioned in the text are highlighted in panel d, e, and f.

2.11.5 References

Cronin M. F., and W. S. Kessler (2009), Near-surface shear flow in the tropical Pacific cold tongue front. *J. Phys. Oceanogr.*, **39**, 1200–1215.

Ekman, V. W. (1905), On the influence of the Earth's rotation on ocean currents, *Ark. Mat. Astron. Fys.*, **2**, 1 – 53.

Gong, D., and R. S. Pickart (2016), Early summer water mass transformation in the eastern Chukchi Sea. *Deep Sea Res., Part II*, **130**, 43–55. https://doi.org/10.1016/j.dsr2.2016.04.015.

Itoh, M., Pickart, and Coauthors (2015), Water properties, heat and volume fluxes of Pacific water in Barrow Canyon during summer 2010. *Deep Sea Res., Part I*, **102**(C), 43–54. https://doi.org/10.1016/j.dsr.2015.04.004.

Large, W. G., and S. Yeager (2004), Diurnal to decadal global forcing for ocean and sea-ice models: The data sets and flux climatologies, NCAR Tech. Note: NCAR/TN-460+STR, CGD Division of the National Center for Atmospheric Research, 105 pp., Boulder, Colo.

Notz, D., and Coauthors (2003) Impact of underwater-ice evolution on Arctic summer sea ice, *J. Geophys. Res.*, **108**(C7), 3223, doi:10.1029/2001JC001173.

Paquette, R. G., and R. H. Bourke (1974), Observations on the coastal current of Arctic Alaska. *J. Mar. Res.*, **32**, 195–207.

Perovich, D. K., T. C. Grenfell, B. Light, and P. V. Hobbs (2002), Seasonal evolution of the albedo of multiyear Arctic sea ice, *J. Geophys. Res.*, **107**(C10), 8044, doi:10.1029/2000JC000438.

Perovich, D. K., S. V. Nghiem, T. Markus, and A. Schweiger (2007), Seasonal evolution and interannual variability of the local solar energy absorbed by the Arctic sea ice–ocean system, J. *Geophys. Res.*, **112**, C03005, doi:10.1029/2006JC003558.

Pickart, R. S., G. W. K. Moore, C. Mao, F. Bahr, C. Nobre, and T. J. Weingartner (2016), Circulation of winter water on the Chukchi shelf in early Summer, *Deep Sea Res., Part II*, **130**, 46–75, doi: 10.1016/j.dsr2.2016.05.001.

Pond, S., and G. L. Pickard (1983), Introductory Dynamical Oceanography, 2nd ed., Pergamon, Boston.

Shimada, K., E. Carmack, K. Hatakeyama, and T. Takizawa (2001), Varieties of shallow temperature maximum waters in the Western Canadian Basin of the Arctic Ocean, *Geophys. Res. Lett.*, **28**, 3441–3444.

Steele, M., J. Morison, W. Ermold, I. Rigor, M. Ortmeyer, and K. Shimada (2004), Circulation of summer Pacific haloclinewater in the Arctic Ocean, *J. Geophys. Res.*, **109**, C02027, doi:10.1029/2003JC002009.

Steele, M., and W. Ermold (2015), Loitering of the retreating sea ice edge in the Arctic Seas, *J. Geophys. Res. Oceans*, **120**, 7699–7721, doi:10.1002/ 2015JC011182.

Weingartner, T. J., S. L. Danielson, and T. C. Royer (2005), Freshwater variability and predictability in the Alaskan Coastal Current, *Deep Sea Res., Part II*, **52**, 161–191.

Wenegrat, J. O., and M. J. McPhaden (2015), Dynamics of the surface layer diurnal cycle in the equatorial Atlantic Ocean (0°, 23°W), *J. Geophys. Res. Oceans*, **120**, 563–581, doi:10.1002/ 2014JC010504.

Winsor, P., and D. C. Chapman (2004), Pathways of Pacific water across the Chukchi Sea: a numerial model study. *J. Geophys. Res.*, **109**, C03002. http://dx.doi.org/ 10.1029/20 03JC0 01962.

Chapter 3 Source of Uncertainties in Simulating the Sea Ice Thickness and Motion[2]

Abstract

Changes in Arctic sea ice is a critical indicator of Arctic and global climate changes. Due to a lack of sufficient observational data and fully resolved feedback and interactive processes, realistic simulation of Arctic sea ice thickness distribution has been one of the most challenging problems in climate model development and climate studies for understanding physical processes. Through conducting a series of modeling experiments using the coupled sea ice-ocean components of the NCAR's Community Earth System Model version 1.2 (CESM 1.2), we examined sensitivities of sea ice thickness distribution to the collaborative effects between air-ice momentum flux and sea ice strength. We found that sea ice thickness distribution and associated volume and velocity are highly sensitive to perturbed air-ice momentum flux and sea ice strength. A decrease in sea ice strength results in a thicker basin-average ice and therefore a larger ice volume throughout the year since more kinetic energy is converted to the potential energy to build the sea ice ridges, instead of frictional loss. The differences of sea ice thickness between the experiments with a maximum and a minimum ice strength can be reduced as air-ice momentum flux decreases. A similar feature is also found in sea ice volume. The decrease in sea ice strength without changing air-ice momentum flux also causes a larger annual mean sea ice velocity, with no change of air-ice momentum flux. In the experiments where sea

---

[2] Peng L. and X. Zhang, In Preparation for Journal of Physical Oceanography, Sensitivity of Sea ice Simulations to Ice Dynamic Treatments.

ice strength remains unchanged, a decrease in air-ice momentum flux produces a weaker sea ice velocity throughout the year. To investigate upscaling impacts of these small-scale dynamic processes on shaping sea ice thickness distribution, we implemented tracers analysis in the modeling experiments. From the pathways of tracers, we showed the origin of tracked sea ice and its variation along the path. The results indicate that increased ice strength or decreased air-ice momentum flux cause a counter-clockwise rotation of the transpolar drift, resulting in an increase in sea ice export through the Fram Strait and therefore reduction of the pan-Arctic sea ice thickness. In contrast, clockwise rotation of the sea ice transpolar drift leads to more sea ice that circulates and accumulates in the central/western Arctic, instead of exporting through the Fram Strait.

3.1 Introduction

Significant reductions in sea ice coverage (Cavalieri and Parkinson, 2012; Comiso, 2012), multiyear sea ice (Maslanik et al., 2011), and sea ice thickness (Yu et al., 2004; Kwok and Rothrock, 2009) have been reported during recent decades. Sea ice thickness plays an essential role through its influence on modifying the sea ice growth rate (Bitz and Roe, 2004), energy exchanges between the overlying atmosphere and the underlying ocean (Holland et al., 2006), the large-scale atmospheric circulation, and deep water formation (Bitz et al., 2001). To properly understand the recent trends and to further predict the future Arctic climate change, there is an increasing demand for realistic capturing of the spatial distribution of the sea ice thickness (Day et al., 2014; Guemas et al., 2014). However, a number of recent studies show a substantial disagreement of the sea ice thickness distribution among model simulations (Stroeve et al., 2014; Chevallier et al., 2016) and between models and observations (Kreyscher et al., 2000; Rothrock et al., 2003; Miller et al., 2006). Thus, an improved understanding of the physical interaction processes controlling the sea ice thickness distribution is needed.

Previous studies found that changes in the atmospheric circulation, represented by different pressure patterns, were primarily responsible for the basin-scale sea ice thickness changes observed by submarine observations (Tucker et al., 2001; Holloway and Sou, 2002; Rothrock et al., 2003). Most regions over the Arctic have a moderate magnitude of ocean currents, and the surface winds are regarded as the primary source of kinetic energy for the basin-scale sea ice; therefore, the atmospheric circulation has a large influence on the sea ice flow pattern (Rigor et al., 2002; Wu et al., 2006) and the sea ice exportation (Rigor and Wallace, 2004; Watanabe et al., 2006).

External forces including air/ice drag, ocean/ice drag, Coriolis force, and sea surface tilting may change sea ice motion and cause sea-ice deformations. Both shearing and convergence deformations lead to ridge building, during which sea ice conducts deformation work and converts the sea ice kinetic energy into the potential energy by increasing sea ice thickness and causing energy loss due to friction. The sea ice strength is a function of the energy loss during the ridging, therefore describes the efficiency of sea ice energy conversion from kinetic to potential energy. Modeling studies proved that different parameters used in defining the sea ice strength can have significant impact on the simulated sea ice thickness distribution (Steele et al., 1997). Due to the complicated nature of the sea ice mechanical properties, direct measurements of the sea ice strength are very challenging to design and execute.

In this study, we investigate variations of the sea ice thickness distribution and sea ice motion via controlling both the source and sink of the sea ice kinetic energy. To exclude the impact of year-to-year variations on the surface wind circulation patterns, we simplified our experiments by using a repeated climatological forcing. A negative feedback mechanism between sea ice thickness and sea ice strength was proposed by previous studies (Hibler, 1984; Holland et al., 2006), in which over regions where sea ice experiences convergence, the sea ice thinning triggered by thermodynamic processes reduces the resistance towards dynamic thickening and therefore counteracts the thinning. This study investigates the impact of the sea ice strength on the sea ice thickness distribution via changing the magnitude of the air/ice drag at pan-Arctic scales. We show that changes in the magnitude of the sea ice strength and air/ice drag affect sea ice motion and, in turn, affect the sea ice thickness distribution.

In the next section, we briefly describe the theoretical basis for the model. The numerical settings and the experimental

designs are described in section 3.3. In section 3.4, we first compared our control simulation with observational data, and presented an analysis of the annual cycle differences among 25 sensitivity experiments. The impact of ice strength involving the thermodynamic and dynamic processes on ice thickness and ice motion is investigated in the later discussion. We further analyzed the variations of sea ice motion impact on the sea ice thickness distribution in section 3.5. In the last section, we summarize our major findings and conclusions.

3.2 Model Experiments and Forcing Data

The tensor form of the sea ice momentum equation describing the force balance used by the model (Hunke and Dukowicz, 1997; Hunke, 2001) is given by

$$\mathrm{m}\frac{\partial u_i}{\partial t} = \frac{\partial \sigma_{ij}}{\partial x_j} + \tau_{ai} + \tau_{wi} + \varepsilon_{ij3} m f u_j - \mathrm{mg}\frac{\partial H}{\partial x_i} \tag{1}$$

where u_i is the horizontal sea ice velocity vector, σ_{ij} is the two-dimensional sea ice internal stress tensor, m is the total mass of ice and snow per unit area, f is the Coriolis parameter, g is the gravitational acceleration, and H is the sea surface height. In Eq. 1, ε_{ij3} equals 0 for $i = j$, 1 for $i < j$, and -1 for $i > j$. According to McPhee (1986), the air stress (τ_{ai}) and the ocean stress (τ_{wi}) are

$$\tau_{ai} = c_a \rho_a |u_{ai}| (u_{ai} - u_i) \tag{2}$$

$$\tau_{wi} = c_w \rho_w |u_{wi} - u_i| (u_{wi} - u_i) \tag{3}$$

where c_a and c_w are air and ocean drag coefficients respectively, u_{ai} and u_{wi} are the air velocity and ocean currents respectively. The air and seawater density are ρ_a and ρ_w respectively. Based on the sea ice velocity, the strain rate $(\dot{\varepsilon}_{ij})$ is defined as

$$\dot{\varepsilon}_{ij} = \frac{1}{2}\left(\frac{\partial u_i}{\partial x_j} + \frac{\partial u_j}{\partial x_i}\right) \tag{4}$$

and the divergence (D_D), tension $(D_T)$and shearing (D_S) strain rates can be written as

$$D_D = \dot{\varepsilon}_{11} + \dot{\varepsilon}_{22} \tag{5}$$

$$D_T = \dot{\varepsilon}_{11} - \dot{\varepsilon}_{22} \tag{6}$$

$$D_S = 2\dot{\varepsilon}_{12} \tag{7}$$

Following the Elastic-Viscous-Plastic (EVP) rheology (Hunke and Dukowicz, 1997), by adding the elastic contribution to the classic Viscous-Plastic (VP) rheology (Hibler, 1979), the constitutive law, which bridges the strain rate to the sea ice stress, can be written as

$$\frac{1}{E}\frac{\partial \sigma_1}{\partial t} + \frac{\sigma_1}{2\zeta} + \frac{P}{2\zeta} = D_D \tag{8}$$

$$\frac{1}{E}\frac{\partial \sigma_2}{\partial t} + \frac{\sigma_2}{2\eta} = D_T \tag{9}$$

$$\frac{1}{E}\frac{\partial \sigma_{12}}{\partial t} + \frac{\sigma_{12}}{2\eta} = \frac{1}{2} D_S \tag{10}$$

where $E = \frac{\zeta}{T}$ is the elastic modulus, and T represents the damping scale for the elastic wave (Hunke, 2001). In Eq. 8-10, P is the sea ice strength. The non-linear bulk (ζ) and shear (η) viscosities in Eq. 8-10 are

$$\zeta = \frac{P}{2\Delta} \tag{11}$$

$$\eta = \frac{\zeta}{e^2} = \frac{P}{2\Delta e^2} \tag{12}$$

where Δ is the deformation function

$$\Delta = \sqrt{D_D^2 + (D_T^2 + D_S^2)/e^2} \tag{13}$$

In Eq. 13, the eccentricity ($e = 2$) describes the ratio of the principal axes of the ellipse yield curve (the ratio between the maximum compressive and shear strength).

The constitutive law is determined by an ellipse yield curve and a flow rule, which characterizing the relative partitioning of the shear to divergence strain rate along the yield curve. Normalized by the sea ice strength, the yield curve can be written as

$$F(\sigma_I, \sigma_{II}) = \left(\frac{2\sigma_I}{P} + 1\right)^2 + \left(\frac{2e\sigma_{II}}{P}\right)^2 \tag{14}$$

in terms of two invariants $\sigma_I = \frac{1}{2}(\sigma_1 + \sigma_2) = \frac{1}{2}(\sigma_{1p} + \sigma_{2p})$ and $\sigma_{II} = -\sigma_{11}\sigma_{22} + \sigma_{12}^2 = \frac{1}{2}(\sigma_{2p} - \sigma_{1p})$, where σ_{1p} and σ_{2p} are the principal stresses. Both σ_{1p} and σ_{2p} are the eigenvalues of the σ_{ij}. The flow rule $\dot{\varepsilon}_k = \lambda \frac{\partial F}{\partial \sigma_k}\Big|_{F=0}$ makes the strain rate vector normal to the yield curve, where $\lambda = \frac{\Delta}{P}$ and $k = I, II$. The sea ice strength determines the size of the non-

normalized yield curve (Eq. 14) and also describes the rate of energy dissipation per unit strain rate in compression. The deformation work done by the internal stress contributes either to form the ice ridge, which tends to change the gravitational potential energy, or to dissipate through the friction (Flato and Hibler, 1995) and can be written as

$$\sigma_I \dot{\varepsilon}_I + \sigma_{II} \dot{\varepsilon}_{II} = \left(\sigma_I + \frac{P}{2}\right)^2 + \left(e\sigma_{II} - \frac{P}{2}\right)^2 \tag{15}$$

Note here that $\dot{\varepsilon}_I = D_D$ and $\dot{\varepsilon}_{II} = \sqrt{D_T^2 + D_S^2}$.

Both thermodynamic and dynamic processes can change the sea ice thickness distribution (ITD), which is given by the balance equation

$$\frac{\partial G}{\partial t} = -\nabla \cdot (vG) - \frac{\partial}{\partial h}(fG) + \psi \tag{16}$$

The ITD function $G(h)$ is a function of the ice thickness h and is defined as the area fraction of the ice-covered region in the thickness range between h and $h + dh$. Thus, the integration of $G(h)$ at each grid point over all thickness ranges equal the total grid area covered by sea ice at that grid point. According to Eq. 16, the local time derivative of the thickness distribution is determined by the divergence of the horizontal thickness flux $-\nabla \cdot (vG)$, the thermodynamic growth rate function $\frac{\partial}{\partial h}(fG)$, and the mechanical redistribution function ψ, which redistribute sea ice between different thickness categories via deformation events (Thorndike et al., 1975) and can be written as

$$\psi = \dot{\varepsilon}_I \delta(h) + w_r M \tag{17}$$

where $\delta(h)$ is the Dirac delta distribution. If $h = 0$, $\delta(h) = 1$, otherwise, $\delta(h) = 0$. The normalized mechanical energy dissipation rate is given by

$$M = \frac{1}{2} C_s(\Delta - |\dot{\varepsilon}_I|) + min(\dot{\varepsilon}_I, 0) \tag{18}$$

where $C_s = 0.25$ represents the fraction of shear deformation energy contributing to the ridging process. In Eq. 17, the ridging mode is given by

$$w_r(h) = \frac{-a_P(h) + \int_0^\infty a_P(h_n)\gamma_n(h_n, h)dh_n}{N} \tag{19}$$

where $a_P(h)$ is the sea ice distribution participating in the ridging process, and can be written as

$$a_P(h) = b(h)G(h) \tag{20}$$

where the participation function $b(h)$ is a weighting function exponentially decreasing with sea ice thickness, and can be written as

$$b(h) = \frac{exp[-G(h)/a^*]}{a^*[1 - exp(-1/a^*)]} \tag{21}$$

where $a^* = 0.05$ represents the mean value of $G(h)$ for ice participating in ridging. The exponential form of the weighting function $b(h)$ promotes the numerical stability, which allows a maximum time step up to about 2 hours, compared with other options in the model (Lipscomb et al., 2007).

From Eq. 19, the ITD of ridges $\gamma_n(h)$ is given by

$$\gamma_n(h_n, h) = \begin{cases} \dfrac{exp[-(h_n - h_{min})/\lambda]}{k_n \lambda}, & h < h_{min} \\ 0, & h \geq h_{min} \end{cases} \tag{22}$$

where $\lambda = \mu\sqrt{h_n}$ is an e-folding scale. For ice thickness greater than 1 m, the corresponding minimum ridge thickness h_{min} is $h + h_{raft}$, otherwise, is $2h$. The maximum ice thickness allowed to raft (h_{raft}) is set equal to 1m. The factor $k_n = (h_{min} + \lambda)/h_n$ represents the ratio between the mean ridge thickness and the thickness of ridging ice.

Finally, the sea ice strength P is given by

$$P = C_f C_p \int_0^{\infty} h^2 \, w_r \, dh \tag{23}$$

The parameter $C_p = \frac{\rho_i(\rho_w - \rho_i)g}{2\rho_w}$, where ρ_w and ρ_i are the water and ice density respectively, and the parameter C_f represents the ratio of total energy losses to potential energy changes with a default value of 17. An estimation of C_f suggests this value should range from 2 to 10 (Hibler, 1980) and 10 to 17 according to (Hopkins and Hibler, 1994). Smaller magnitude of C_f represents larger faction of energy has been used by changing the potential energy instead of frictional dissipation and vice versa. Thus, a smaller C_f means the inter-floe sliding friction has been reduced.

3.3 Approach

We used the Community Earth System Model (CESM 1.2) to conduct our experiments. The CESM 1.2 is a fully coupled earth system model developed by the National Center for

Atmospheric Research (NCAR). The ocean component is based on the Parallel Ocean Program, version 2 (Danabasoglu et al., 2012), and the sea ice component is based on the Los Alamos National Laboratory sea ice model, version 4 (CICE4), which is also known as the Community Ice Code (Hunke and Lipscomb, 2008). The CICE4 model has five thickness categories (Lipscomb, 2001). The ocean model is configured with 60 vertical levels, and the vertical resolution spanned from 10 m at upper 150 m to 250 m in the deep oceans. The ocean model was initialized from Levitus initial conditions (Levitus and Boyer, 1994) and a state of rest. By integrating the model for a sufficiently long time, the model result is expected to be independent of initial conditions. Both components use the same horizontal grid, the one-degree displaced the North Pole in Greenland grid, which is uniform in the zonal direction but gradually decrease towards Greenland pole in meridional direction. Within the Arctic Ocean (latitude greater than 65°), the average grid size, defined as the square root of the grid area, is 41 km, with a minimum of 22.34 km near the East coast of Greenland and a maximum of 61.72 km over the Chukchi Sea.

We conduct experiments with 25 combinations of the air/ice drag and the sea ice strength conditions and multiply the default value of c_a in Eq. 2 and C_f in Eq. 23 by a constant ranging from 0.2 to 1 with a 0.2 interval (Table 1). The aim of these experiments is to control both the source and sink of the sea ice kinematic energy and to examine changes in sea ice properties under different conditions. The coupled ocean and sea ice model were integrated for 100 years, and the annual cycle of the ice volume and total area approached equilibrium with little variations between sequential years.

3.4 Data

The climatological atmospheric forcing data was derived from a ten-year period (1979-1988) averaged ERA-Interim data (Dee et al., 2011). This forcing data consists of five atmospheric state variables, which are the 10 m surface wind components, 2 m-air temperature, specific humidity, and the mean sea level pressure at a six-hourly resolution. The 6 hourly climatological mean surface wind components are estimated by first averaging the wind speeds and directions separately and decompose back into each component. The downward longwave and shortwave radiation and the precipitations are daily and monthly averaged respectively.

We used the sea ice concentration data derived by the NASA team (Cavalieri et al., 1995) and the Bootstrap algorithm (Comiso, 2017) to compare with the model results. Both records are projected on the polar stereographic grid with a grid size of 25x25 km. This data combined satellite-based measurements from the Scanning Multichannel Microwave Radiometer (SSMR), from Special Sensor Microwave/Imagers (SSM/Is), and from the Special Sensor Microwave Imager/Sounder (SSMIS). Both algorithms were applied to SSMR measurements, which span from 1978 to 1987 and provided data every other day. The NASA Team algorithm estimated the total ice concentration in terms of brightness temperatures derived from three SSM/I channels with an 5% accuracy in general and 15% accuracy during summer (Cavalieri et al., 1991; Steffen and Schweiger, 1991). The Bootstrap algorithm (Comiso, 1996) combines the brightness temperature measurements from multiple channels and assumes the ice concentration reached 100% during the winter over the central Arctic, while the open water tie points were derived based on daily values in May and October taken different weather conditions into account (Comiso et al., 2017). Due to better statistics, the accuracy of the derived ice concentration span from 5%-10% (Comiso, 2002).

The simulated ice thickness is compared with the Unified Sea Ice Thickness Climate Data Record (Lindsay, 2013). This dataset includes measurements based on submarines, moorings, airborne, and satellite observations. From 1988 onward, the thickness comparisons are only based on submarine measurements, which are spatially averaged approximately 50 km. A conversion from ice draft to ice thickness was conducted (Rothrock et al., 2008, hereafter R08) combining 34 submarine cruises collected from 1975 to 2000, an Ice Thickness Regression Procedure (ITRP) is used to construct the ice thickness interannual change and the annual cycle within the data release area (DRA). The combined bias of the ice draft measurements is 0.29 ± 0.25 m (Rothrock and Wensnahan, 2007). In comparison with the simulated ice thickness, this positive bias is removed as suggested by the R08 for both U.S. submarine data.

The daily gridded ice motion vectors (Tschudi et al., 2010) are derived based on Advanced Very High Resolution Radiometer (AVHRR), SSMR, SSM/I, SSMIS, Advanced Microwave Scanning Radiometer on the NASA Earth Observing System (EOS) platform (AMSR-E), International Arctic Buoy Program (IABP), and the US National Centers for Environmental Prediction/US National Center for Atmospheric Research (NCEP/NCAR) data. A maximum cross-correlation method (Emery et al., 2002) was applied to successive satellite images to derive the ice motion and further validated by the buoy data. In summer, contaminations due to clouds and lack of buoy measurements due to ice melting result in a data complement by using the NCEP 10m wind data (Thorndike and Colony, 1982).

3.5 Annual Mean Sea Ice Properties

The observed and simulated seasonal cycles of the total sea ice area are displayed in Figure 5a. It can be seen that all experiments show little impact on the simulated total sea ice area, and the

model well captures the timing of the maximum and minimum sea ice areal coverage. The maximum sea ice area occurs on March 10th, while the minimum takes place in September. The simulated sea ice area is, in general, smaller than the observed one derived from Bootstrap algorithm but larger than that provided by the NASA team algorithm. Previous studies suggested that the NASA team algorithm tends to underestimate the sea ice cover (Comiso et al., 2017). Therefore, both the magnitude of the air/ice drag and the sea ice strength do not play a dominant role in governing the total sea ice area. In contrast, the added variabilities on the air/ice drag and the sea ice strength lead to apparent variations on the sea ice volume (Figure 5b), thickness (Figure 5c), and velocity (Figure 5d). According to the R08, the averaged ice thickness within the DRA between 1979 and 1988 equals 3.14 m, and the simulated sea ice thicknesses within the same area span from 2.27 m to 7.08 m (Table 3). Additionally, more sea ice thickness/volume is associated with a larger amplitude of the annual oscillations (Figure 5bc). Variations of the sea ice velocity are prominent except for July to September. Through satellite-based sea ice velocity measurements, the average ice velocity equals to 2.80 cm/s, and simulated velocities span from 0.76 cm/s to 4.89 cm/s.

Comparing the model outputs with R08's sea ice thickness and satellite-based sea ice velocity, we therefore select the W04S04 experiment as the reference case. Comparison of the sea ice velocity between the reference case and observations in March and September is shown in Figure 6. In March, the Beaufort gyre is shown by a clockwise circulation and adjacent to a transpolar drift extending from the coast of Siberia to the passage of Greenland-Spitsbergen. The direction of ice velocities between model and observation agrees well but with a small underestimation of the magnitude especially over the western Arctic. The general counter-clockwise circulation pattern is also reasonably captured by the model during the September.

However, notable model biases can be found over the Chukchi Sea, East Siberian Sea, and the Barents Sea.

Detailed comparisons among sensitivity experiments suggest a potential linkage between variations on C_f and c_a. Decreasing C_f alone results in a thicker ice and therefore a larger sea ice volume throughout the year. Decreasing C_f also causes the ice velocity to become larger except for the August and September due to the inverse flow pattern. When we turn to experiments where C_f remains unchanged, decreasing c_a produces a smaller ice velocity throughout the year. However, both the ice thickness and ice volume show a peculiar feature. The ice thickness (Table 3) first decreases with decreasing c_a until a critical point is reached, after which further decreasing c_a results in an increasing ice thickness. The critical points start between $0.8 \cdot c_a$ and $0.6 \cdot c_a$ at $1.0 \cdot C_f$ condition decreasing to between $0.2 \cdot c_a$ and $0.4 \cdot c_a$ at $0.6 \cdot C_f$ condition. As the C_f further reduced below $0.4 \cdot C_f$, no critical points are found in our experiments and both ice thickness and volume decrease with decreasing c_a. In section 3.5, we will further explore the reason causing the critical points.

3.6 Sea Ice Force Balance

According to the sea ice force balance (Eq. 1), the sea ice motion is governed by the air/ice drag, the internal ice stress gradient force, the ocean/ice drag, the Coriolis force, and sea surface tilting force (Figure 7). The sea ice force balance varies strongly depending on the averaging periods (Steele et al., 1997). For the purpose of this study, we focused on analyzing the monthly average results. The acceleration term on the left-hand side of Eq. 1 has a small contribution and is not shown. According to the reference case (Figure 7h), the internal sea ice stress gradient

force has an opposite direction relative to the Coriolis force, and the ocean/ice drag has an inverse direction to the air/ice drag but with a smaller magnitude over most of the Arctic Ocean. The sea surface tilting force has a much smaller magnitude than the other four components. Additionally, both the Coriolis force and the internal ice stress gradient force have components acting to offset the air/ice drag for the reference case.

A larger air/ice drag corresponds to a more extensive kinematic energy gain by the sea ice and results in a larger magnitude of sea ice velocity (Figure 7be) compared with the reference case (Figure 7h). Over the same latitude, a larger sea ice velocity is also associated with a more substantial Coriolis force (Figure 7be) compared with the reference case (Figure 7h). As the air/ice drag decreased (from the top to the bottom row of the Figure 8) the most notable change is a decreasing sea ice velocity (Figure 8k) and, not surprisingly, the magnitude of the Coriolis force also decreased (Figure 7k). Meanwhile, the direction of Coriolis force turns counter-clockwise relative to the direction of the air-ice drag along the transpolar drift, and the sea ice velocity also rotates in a similar manner (Figure 8b-k). This rotation of the Coriolis force tends to have a less negative or even a positive component relative to the air-ice drag and acts to offset the counter-clockwise rotation of the internal stress gradient (Figure 7b-k), which result in a larger contribution to offset the air-ice drag. An increasing the sea ice strength (Figure 7 from right to left) results in a counter-clockwise rotation of the internal ice stress gradient force relative to the direction of the air-ice drag, and the partition of the internal ice stress gradient force becomes larger compared with other components. As a result of changing sea ice force balance, the sea ice velocity also rotates counter-clockwise (Figure 8 from right to left).

All experiments are forced by the same wind direction, therefore, can be regarded as applying the same atmospheric pressure pattern. Changes in either the magnitude of air-ice drag or the sea ice strength leads to variations on sea ice velocity. This is primarily due to the linkage between the Coriolis force and the sea ice velocity. A smaller magnitude of sea ice velocity corresponding to a weaker Coriolis force, which results in a counter-clockwise rotation sea ice velocity. Therefore, the sea ice velocity is not only controlled by the large-scale pressure pattern, but also impact by the wind speed.

3.7 Thermodynamic and Dynamic Processes Impacting on Sea Ice Growth Rate

The magnitude of sea ice growth rates due to both thermodynamic and dynamic processes differs substantially among the experiments. In January, sea ice forms over the east flank of the Beaufort and Chukchi Seas and over the Laptev and Kara Seas. Offshore surface winds drive divergence over those regions (Figure 8) and lead to an open water formation, which tends to produce thin ice due to atmospheric cooling. The relatively thicker ice over the central Arctic serves as a thermal insulator preventing heat exchanges between the ocean and the atmosphere, and thereby, corresponding to a moderate and homogeneously distributed sea ice growth rates.

Associated with an increasing air/ice drag or decreasing ice strength, the magnitude of both divergence and convergence increases, which results in an enhanced new sea ice formation and ridge building rate (Figure 8). The relatively large ridge building rates over coast area of the Barrow, the Chukchi Sea, the north coast of Greenland, and the transpolar drift belt (Figure 8b-r) are closely related to the strong local convergences (Figure 8). Additionally, a more substantial divergence leads to a significant increase of the open water, which facilitate new sea

ice formation over the Laptev and Kara Seas. As the air/ice drag increase, regions corresponding to the new ice formation extends further north towards the central Arctic.

3.8 Sea Ice Rheology

The sea ice rheology bridges the sea ice motion (deformation) and the force balance through its impacts on the sea ice internal stress. The internal ice stress is governed by both the sea ice strain rate and the sea ice strength through the constitutive law (Eq. 14), and the internal ice stress gradient is proportional to the sea ice strength gradient at the steady state (Eq. 8-10), and the ice strength is highly sensitive to variations on the sea ice thickness (Eq. 23). According to the Eq. 14, for points lying on the normalized ellipse curve, sea ice is in a state of plastic motion so that $F(\sigma_I, \sigma_{II}) = 1$, while points which are inside of the ellipse curve, define the state of viscous motion and $F(\sigma_I, \sigma_{II}) < 1$. The spatial distribution of F is shown in Figure 9. The size of the nonnormalized ellipse yield curve is controlled by the sea ice strength. In other words, if we normalize the sea ice internal stress by the sea ice strength, increasing the sea ice strength moves points inside ellipse yield curve, and F becomes less than 1.

Generally, as the sea ice moves from low to high sea ice thickness (strength) areas (across the sea ice thickness/strength contours uphill), the sea ice rheology gradually converts from a plastic into a viscous nature. Following the Beaufort Gyre, the thin ice over the East Siberian Sea corresponds to a small sea ice strength (Figure 8h) and behaves plastically (Figure 9h) with small sea ice internal and external stresses (Figure 7h). After the sea ice flow passes the East Siberian Sea, it starts to cut across the ice strength/thickness contour, thereafter, the flow gradually becomes viscous (Figure 9h). The air/ice drags have similar magnitudes at both points A and B (Figure 7h), however, the internal sea ice stress gradient increased significantly from

point A to point B due primarily to a larger sea ice strength gradient at point B (Figure 10h). Similarly, the thin ice formed over the Laptev Sea advects northwestward with a much larger cross ice strength contour components, which leads to an even smaller magnitude of F the north of the Severnaya Zemlya (Figure 9h). Following the transpolar drift, the direction of internal ice stress gradient always points to the left-hand side of the air-ice drag direction (Figure 7) due to the spatial sea ice thickness distribution (Figure 10). Therefore, a larger internal ice stress gradient results in a sea ice flow veer left compared to the upstream flow direction as the sea ice moves uphill across the sea ice strength contours. Increasing the air-ice drag or decreasing the sea ice strength results in more sea ice converting from plastic behavior into viscous behavior (Figure 9), and the overall impact on the transpolar drift is to turn counterclockwise relative to the air-ice drag direction. As the sea ice further moves downstream over the northern Laptev Sea, it behaves viscously (Figure 9h). The flow bifurcates into two branches as it approaches northern coast of Greenland. One branch of the flow causes sea ice export through the Fram Strait. The reverse flow, which recycles the sea ice back into the Beaufort Gyre, causes it to move from low ice strength region into high ice strength region ~400 km north of the Canadian Archipelago causing an extensive area of the sea ice to behave viscously (Figure 9h).

Following the westward sea ice propagation over the Beaufort and Chukchi Seas, another viscous area north of Barrow was found over the coastal areas. The thin ice formed over the Beaufort Sea during the winter associated with low ice strength transports sea ice westward towards regions corresponding to a higher ice strength. As the sea ice moved into the viscous area, the internal ice stress gradient has a larger component opposite to the air-ice drag (Figure 7c-s). It has a potential to reduce the sea ice drift speed and the Coriolis force as well, but an enhancement of the air-ice drag (Figure 7c-s) following this westerly flow exceeds the impact

due to the internal stress gradient, therefore, the corresponding sea ice velocity and Coriolis force increased accordingly. The enhanced Coriolis force prevents the sea ice flow from veering to its left-hand side compared with its upstream flow direction.

As the sea ice strength increases (e.g. Figure 7g-i), the magnitude of the internal sea ice stress gradient increases and gradually rotates counterclockwise towards the opposite direction of the air-ice drag. As a result, the sea ice velocity veers counter-clockwise (e.g. Figure 9g-i). A larger magnitude of the sea ice strength results in a smaller sea ice velocity due to a more substantial kinetic energy lost via the inter-floe friction. For a same strain rate, larger sea ice strength corresponds to a thinner sea ice (Figure 10) since less energy is available to build ridges. As the sea ice strength increases, the thick ice tends to confine within the north coast of the Canadian Archipelago instead of extending towards the central Arctic. The low sea ice strength case produces much thicker ice over the region controlled by the Beaufort Gyre.

In summary, large air/ice drag or smaller sea ice strength is able to support the sea ice motion over most regions as the sea ice behaves plastically. However, as the air/ice drag reduces or the sea ice strength increases, the sea ice over more extensive regions behaves viscously (Figure 9), which is also accompanied by decreasing sea ice speed and a counterclockwise rotation of the sea ice velocity. Such a behavior is not evenly applied over the entire Arctic. The sea ice over the western Arctic tends to behave more plastically and has less rotation of the sea ice velocity due to a larger air-ice drag compared with the eastern Arctic, and the sea ice over the central/eastern Arctic tends to behave more viscously and has a stronger impact to the axis of the transpolar drift.

3.9 Variations on Sea Ice Motion Impact on Sea Ice Thickness Distribution

We next ask how does the changing sea ice velocity impact on the spatial distribution of the sea ice thickness, and in general the sea-ice force balance. We start by introducing a tracer method. In Figure 11, we showed four tracers with two of them over the Beaufort Sea (pink and red pathways), one over East Siberian Sea (light blue pathway), and the last one over the Laptev Sea (cyan pathway). All tracers are released on December 1st since the magnitude of the sea ice velocity has the largest difference among sensitivity experiments (Figure 5d) over that month. We tracked the path of the tracer based on the monthly averaged sea ice motion field so that daily perturbations on the simulated sea ice velocity do not impact our analysis. The integration step is one day, which means we update the location of the tracer and the corresponding sea ice velocity every time step (one day) based on its new location. The integration continued for 8 years unless the path of the tracer reaches the continent. This method offers an opportunity to examine how thickness varies along the pathway and backtrack the dominant factors governing variations on sea ice thickness (distribution) along the pathway. Note that the pathways for all tracers show a significant change in its moving direction during the summer seasons each year due to the reversing flow pattern from anticyclonic during the winter to the cyclonic during the summer (Figure 6).

As shown by the reference case (Figure 11h), the time required for the sea ice to transport from the Beaufort Sea to the north coast of the Canadian Archipelago is at least 7 years, to the Chukchi Sea is only 1-2 years. Through this process, sea ice along the pathway closer to the interior of the Beaufort Gyre (shown by the red pathways in Figure 11) has to spend a longer

time than the periphery flow (shown by pink pathway in Figure 11) since the magnitude of the sea ice velocity is smaller for the interior flow.

Due to the complex coastal geometry over the Arctic, different sea ice velocity, and the annually inverse of the sea ice flow patterns, a nonlinear relationship is found between the sea ice thickness, the air-ice drag, and sea ice strength among the sensitivity experiments (Section 5.1). Sea ice tends to accumulate as it is blocked by coasts or islands. As shown by the reference case, the periphery pathway (the pink line in Figure 11h) stops at the East Siberian Sea after two years of westward propagation following the Beaufort Gyre. Decreasing the air-ice drag (Figure 11k) results in a shorter pathway but longer duration due to smaller sea ice velocity. Increasing the air-ice drag (Figure 11be) allows the tracers originate from the Beaufort Sea to further propagate westward through the East Siberian Sea and even export via the Fram Strait (Figure 11b). Over the western Arctic, sea ice following the periphery flow may be blocked by the north coast of Barrow (not shown), the Wrangel island (e.g. Figure 11g), the Lyakhovsky Islands (e.g. Figure 11i), and the coast region of the East Siberian Sea (e.g. Figure 11h). As the sea ice is blocked, it may either completely melt during the summer or attached to the coast and start to accumulate. Over the Laptev Sea, decreasing the sea ice strength results in the sea ice flows closer to the east coast of the Greenland (Figure 11de) due to the clockwise rotation of the transpolar drift. All experiments suggest that the sea ice formed over the Laptev Sea tends to export sea ice directly through the Fram Strait.

Following the interior flow, increasing air/ice drag or decreasing sea ice strength causes thicker ice to recycle and attach to the western Arctic (e.g. Figure 11bef) instead of exporting through the Fram Strait (Figure 11kj) or the north coast of Greenland (Figure 11gh). After the sea ice transports into the northern Laptev Sea and further propagates following the transpolar drift,

decreasing the air-ice drag or increasing the ice strength results in a counter-clockwise tuning of the pathway, while increasing the air-ice drag/decreasing the ice strength results in either more sea ice attached over the north coast of the Canadian Archipelago or recycled back through the Beaufort Gyre and therefore less ice is exported through the Fram Strait.

3.10 Thermodynamic/Dynamic Volume Changing Rate Along the Path of Tracers

Investigations of the physical processes that contribute to the sea ice thickness changes along the tracer pathway help us better understand the spatial sea ice thickness distribution. According to the reference case, as the sea ice gradually propagates towards the Chukchi Sea, over the 0-1 years for periphery pathway (pink line in Figure 11 and Figure 12) and 0-2 years for the interior pathway (red line in Figure 11 and Figure 12), the sea ice thickness gradually decreases (Figure 12a). This is primarily because of an excessive melting during the summer seasons (Figure 12b) especially the basal melt (not shown). The melting rate during the summer exceeds the freezing rate during the winter, as a consequence, the sea ice thickness decreases along the pathways. Meanwhile, the melting rate is larger for the periphery than the interior pathway. This decreasing trend becomes more profound for the lower air-ice drag experiment than for the higher air-ice drag experiments (not shown), since the low air-ice drag experiment corresponding to a smaller sea ice velocity, and therefore the sea ice has to spend a longer time within the Beaufort and Chukchi Seas.

After the sea ice enters the northern East Siberian Sea and further propagates following the transpolar drift, the sea ice thickness gradually increases (Figure 12a). Comparing the annual cycle of the volume tendency due to thermodynamic processes before and after entering the East Siberian Sea, the amplitude of the annual cycle reduced significantly. Unlike the volume

tendency due to thermodynamic processes, which has a well-defined seasonal cycle (Figure 12b), the volume tendency due to dynamic processes has much larger high frequency variations. Compared with the sea ice thickness variations along the interior pathways, the periphery pathway shows a larger high frequency variation (Figure 12a) especially for high air-ice drag experiments. As the sea ice flow through the East Siberian Sea and further transport via the transpolar drift, the high frequency variations on the annual cycle of the sea ice thickness becomes more pronounced.

As shown by the reference case, after the ice thickness approaches ~ 4 m, the sea ice thickness changing rate reduced significantly. Compared with the thick ice, as described by the Eq. 21, the thin ice is more likely to participate in the ridging process. The ice thickness distribution following the red pathway is shown in Figure 13. Within the first two years, the ice thickness distribution becomes broad due to the strong melting and thin ice production. During the year 3 and year 4, the ice thickness distribution gradually becomes single mode and switched from the third bin to the fourth bin (more than 50% of the fractional area covered by sea ice are categorized in the 4^{th} sea ice thickness bin) as the sea ice flow across the ice strength contour. Through dynamical ridging process, the thin ice is soon been consumed and the ice thickness distribution forms a strong peak at bin three. Lack of the thin ice supply, ice thickness increase due to the ridging process becomes less efficient after the year 6. Meanwhile, the thicker ice also acts to insulate heat, so that the overall ice thickness obtained a quasi-steady state as the tracer is surrounded by thick ice.

The dynamic ridging is expected to be larger for the periphery pathway. The seasonal cycle of the ice thickness gradually replaced by a double peak feature at the 4^{th} year for the light blue

pathway. Such double peak feature is not shown by the volume tendency due to thermodynamic processes (Figure 12b). A closer examination (not shown) shows both thermodynamic and dynamic processes contribute to the formation of the first peak, while the second peak is mainly due to the dynamic processes.

To examine variations of the force balances, Figure 12c-f shows the magnitude of the air-ice drag, ocean stress, internal stress, and Coriolis force along the tracer pathways. Periphery flow corresponds to a larger magnitude of the air-ice drag, while a smaller magnitude is found for the interior flow. Following tracers originated over the Beaufort Sea, the air-ice drag is strongest over the western Arctic, while the second peak is obtained over the Nansen Basin following the transpolar drift. For the reference case, when the sea ice approached the northern Laptev Sea (the 0-1 year for tracers originated from the East Siberian Sea and 3-4 year for tracers originated from the Beaufort Sea), the air-ice drag gradually increases. As the sea ice flow across the ice strength contour between 1 and 2 years following the light blue pathway, the internal stress increases. As the light blue pathway becomes parallel to the ice strength contour, the internal ice stress gradually decreases between the second and the third year. As the light blue pathway approaches to the pole (x=0, y=0), the Coriolis force increases dramatically, and the turning of the pathway results in a large cross ice strength contour component, which leads to an increase of the internal ice stress. The light blue pathway veers to its left-hand side and finally reaches to the north coast of the Ellesmere Island. Thick ice tends to accumulate over the east coast as shown by a large ice thickness increase (Figure 12a). Therefore, a large ice thickness gradient results in an enhanced internal ice stress.

3.11 Summary and Concluding Remarks

We have presented 12 out of 25 sensitivity experiments to investigate the impact of sea ice strength on sea ice thickness distribution considering different air-ice drag conditions. There is little difference between the total sea ice area among sensitivity experiments, but there is a significant variation of the sea ice thickness distribution. Depending on the magnitude of the air-ice drag and sea ice strength, there is an abrupt sea ice thickness change. Previous sensitivity studies arbitrary selected two or three sea ice strength values, which may not provide sufficient information about impact of the sea ice strength on the sea ice thickness distribution. In this study, we combined both the impact from ice strength and air-ice drag to provide a more comprehensive picture on their impact of the sea ice thickness distribution.

The results here indicate that the magnitude of sea ice strength has a large impact on sea ice thickness, not only on the total/average sea ice thickness, which is referred as the ice thickness-ice strength relationship by Holland et al., (2006), but also on its horizontal distribution via changing the sea ice velocity. Analyzing the sea ice force balance, our study found that when sea ice flow across the sea ice strength contour from a low sea ice strength area to a high sea ice strength area, such a flow is often associated with an increasing ice strength gradient as well, leading to an increasing internal ice stress gradient. Due to the anticyclonic flow pattern during the winter, the thicker ice is located on the right-hand side of the flow, therefore, the internal stress gradient pointing towards the left-hand side of the flow, which further causes the sea ice velocity veer to its left. Following the flow, as the ice strength increases, the sea ice tends to change its behavior from plastic to viscous over the aforementioned regions. For sensitivity experiments with high ice strength or low air-ice drag (Figure 14), the overall impact is to rotate the transpolar drift counter-clockwise, which results in more sea ice export through the Fram

Strait and therefore reducing the pan-Arctic sea ice thickness. On the other hand, increasing air-ice drag or decreasing ice strength result in a clockwise rotation of the transpolar drift and more sea ice being recycled instead of exporting from the Fram Strait. Therefore, we highlighted a negative ice strength-ice thickness feedback and a positive air-ice drag-ice thickness feedback mechanism.

Our study also has important applications in better understanding the long-term sea ice changes. The loss of sea ice has been linked to changes in the sea level pressure (SLP). The Arctic Oscillation (AO) also known as the Northern Annular Mode (NAM) is defined as the leading mode of SLP variability from an EOF analysis. A low AO index corresponds to a weaker Beaufort high, therefore a weaker Beaufort gyre and a westward shifted Transpolar Drift, compared with the high AO index condition. Under the high AO index condition, on the other hand, more sea ice tends to recirculate back to the Alaskan coast instead of export through the Fram Strait (Rigor and Wallace, 2004; Watanabe et al., 2006). The model study further shows a high North Atlantic Oscillation (NAO) index could explain most of the sea ice thinning due to a significant reduction of sea ice advection from the western Arctic into the eastern Arctic and enhanced sea ice export through the Fram Strait (Zhang et al., 2000). One of the underlying causes of the connection between variations in SLP and sea ice loss is the sea ice motion and its relation to the geostrophic wind. Parallel to the isobars, the geostrophic wind is highly correlated with the sea ice motion observed by drifting buoy data (Thorndike and Colony, 1982) and by sequential satellite images (Kimura and Wakatsuchi, 2000) except for coastal regions. We took advantages of using the Normal Year Forcing simulation by not including the impact of the decadal variations of the air flow patterns, the direction of surface wind is the same for all experiments. A larger momentum flux from the atmosphere into the sea ice (i.e. higher

surface wind speed) can results in changing sea ice velocity (both the direction and magnitude) as well as the pan-Arctic sea ice thickness distribution. If there is some event triggers a rapid increasing (decreasing) ice thickness during the winter, such events will also result in an increasing (decreasing) sea ice strength. As shown by Figure 14, the clockwise rotation of the sea ice velocity leads to more sea ice recycled and accumulated over the central/western Arctic instead of accumulated over the eastern Arctic and export through the Fram Strait. Depending on the interannual variations of the surface wind direction, this turning sea ice velocity can be either enhanced or inhibited and impact long-term sea ice variation.

3.12 Figures

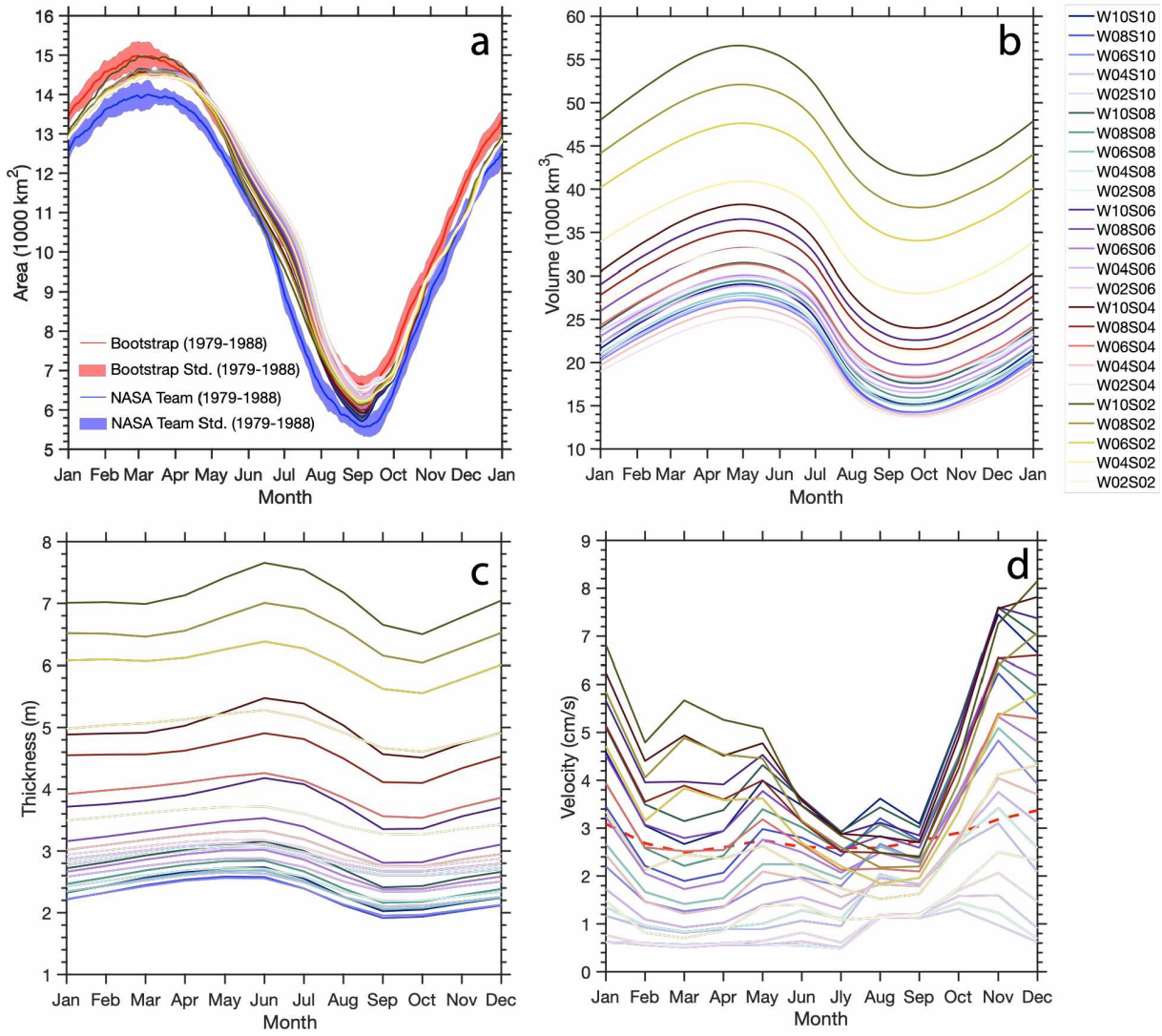

Figure 5. Comparison of the daily mean (a) total sea ice area and (b) sea ice volume for 25 sensitivity experiments. Satellite observed total sea ice area averaged between 1979 to 1988 using the Bootstrap (red) and the NASA team (blue) are also shown in panel a, while the shading area indicating the standard deviation. In panel d, the annual sea ice velocity based on satellite observations (Section 3.4) is shown by the red dash line. Thin solid lines represent model simulation results.

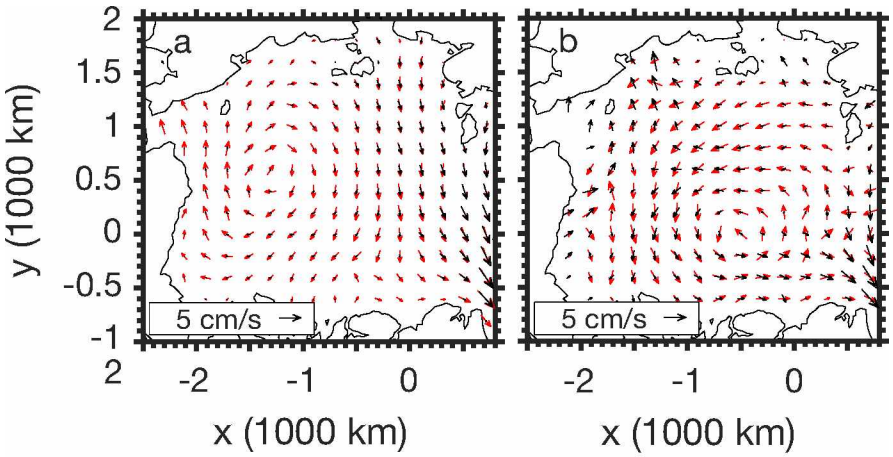

Figure 6. Average sea ice velocity from observation (red arrows) and reference case (black arrows) in (a) March and (b) September.

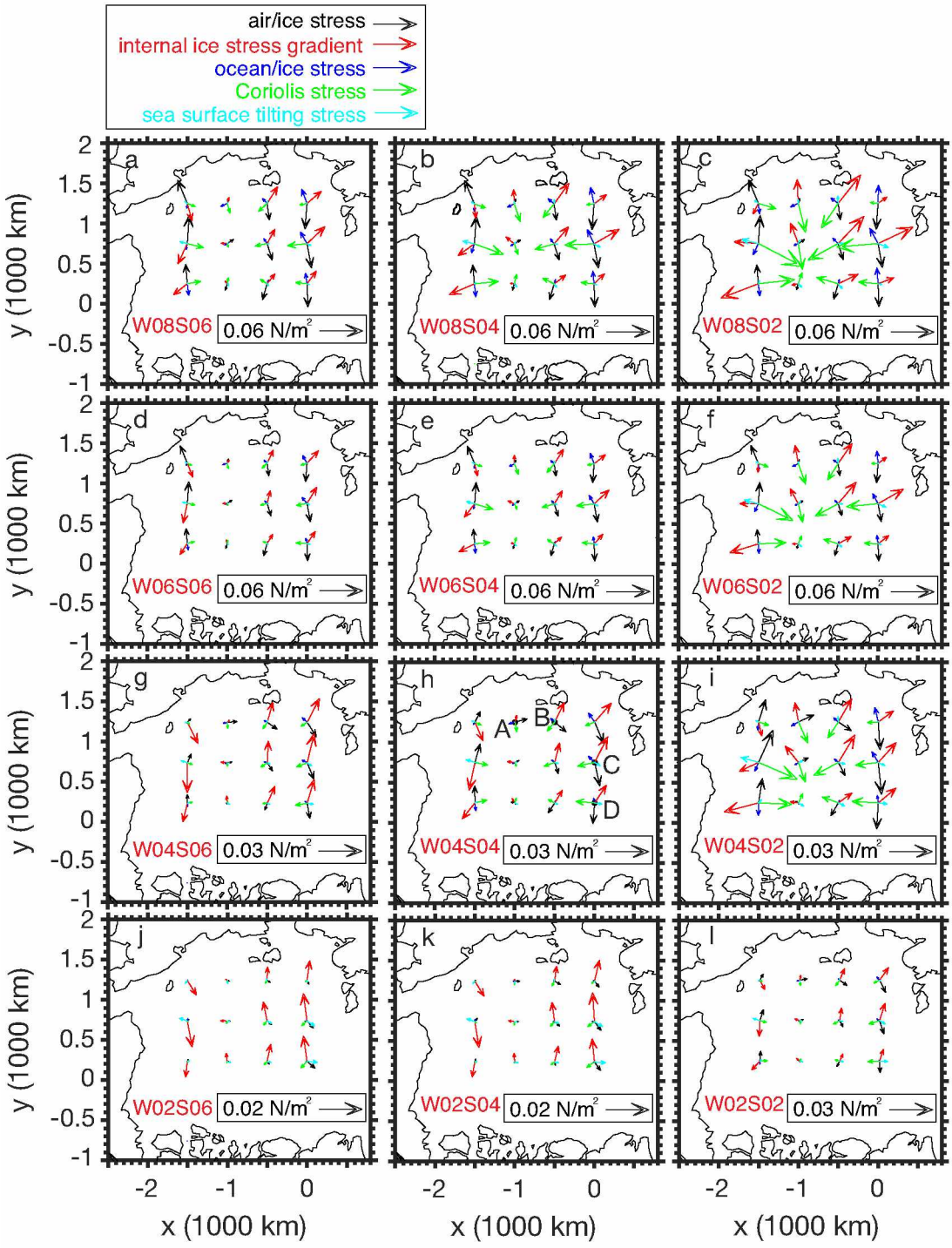

Figure 7. The January sea ice force balance for (a) W08S06, (b) W08S04, (c) W08S02, (d) W06S06, (e) W06S04, (f) W06S02, (g) W04S06, (h) W04S04, and (i) W04S02. Black arrows represent the air/ice drag, red arrows represent the internal ice stress gradient force, blue arrows represent ocean/ice stress, green arrows represent Coriolis stress, and the cyan arrows represent the sea surface tilting stress. In the experiment name, W represents wind and S

Figure 7. (Continued) represents sea ice strength. Numbers following W and S represents the coefficient used to modify the magnitude of C_f and c_a respectively.

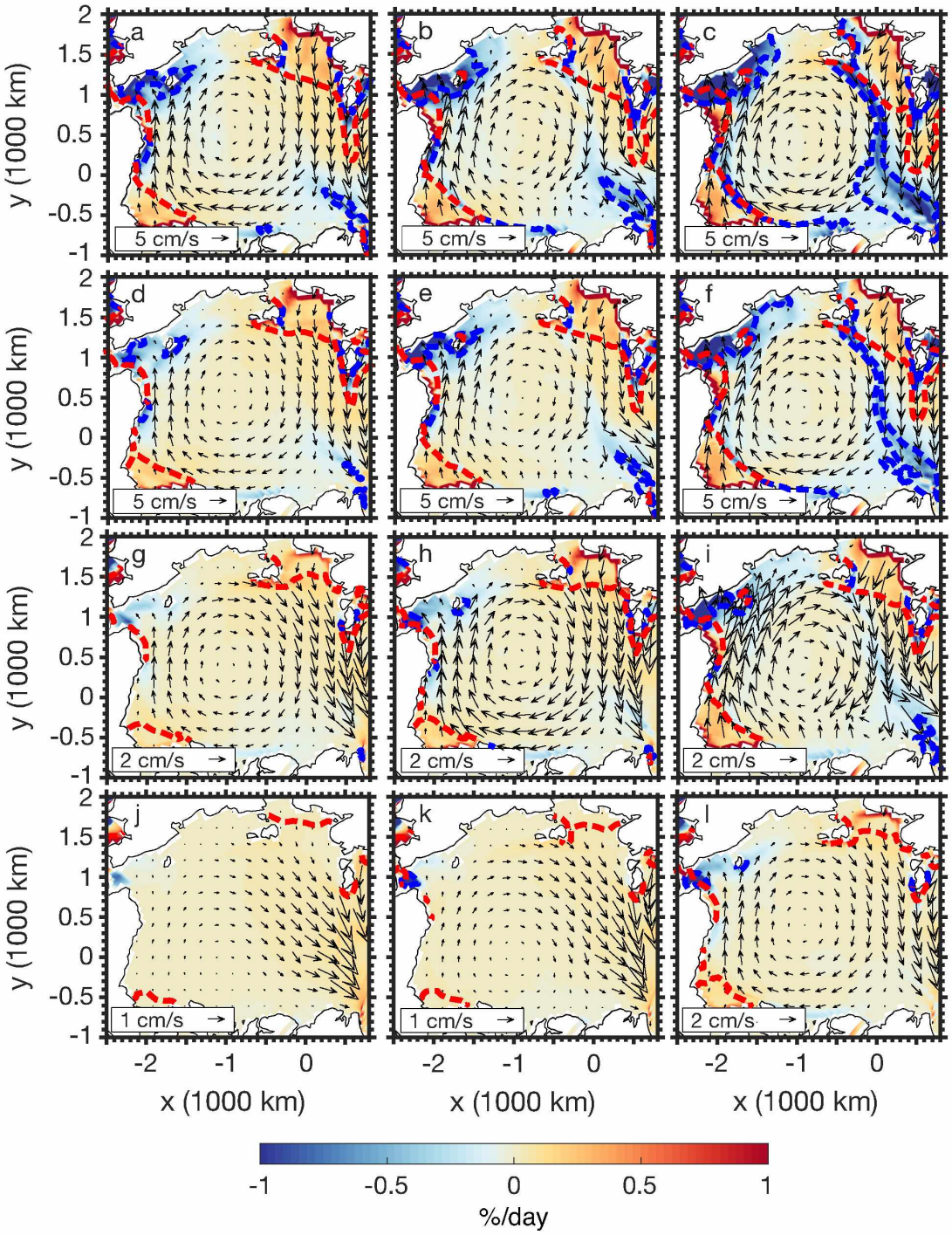

Figure 8. Same experiments as shown in Figure 7, but for the January sea ice convergence (blue) and divergence (red). Thick red lines represent the sea ice thickness growth rate due to

Figure 8. (Continued) thermodynamic processes exceed 0.8 cm/day. The thick blue dash lines represent the sea ice ridging rate exceed 0.8 cm/day.

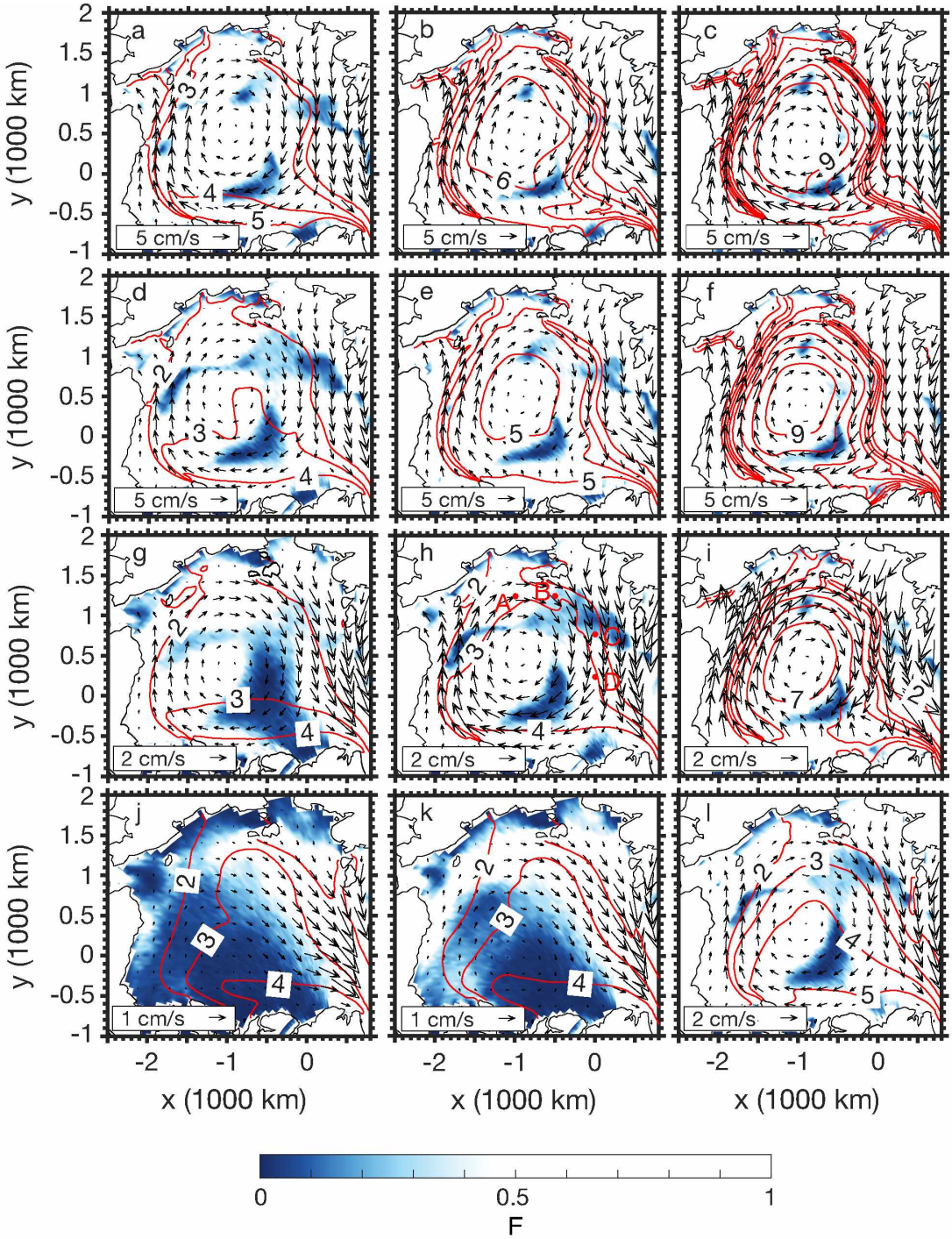

Figure 9. Same experiments as shown in Figure 7, but the color shading represents the magnitude of F in Eq. 14. Blue region represents viscous, while white region represents plastic. Red contours represent the sea ice thickness.

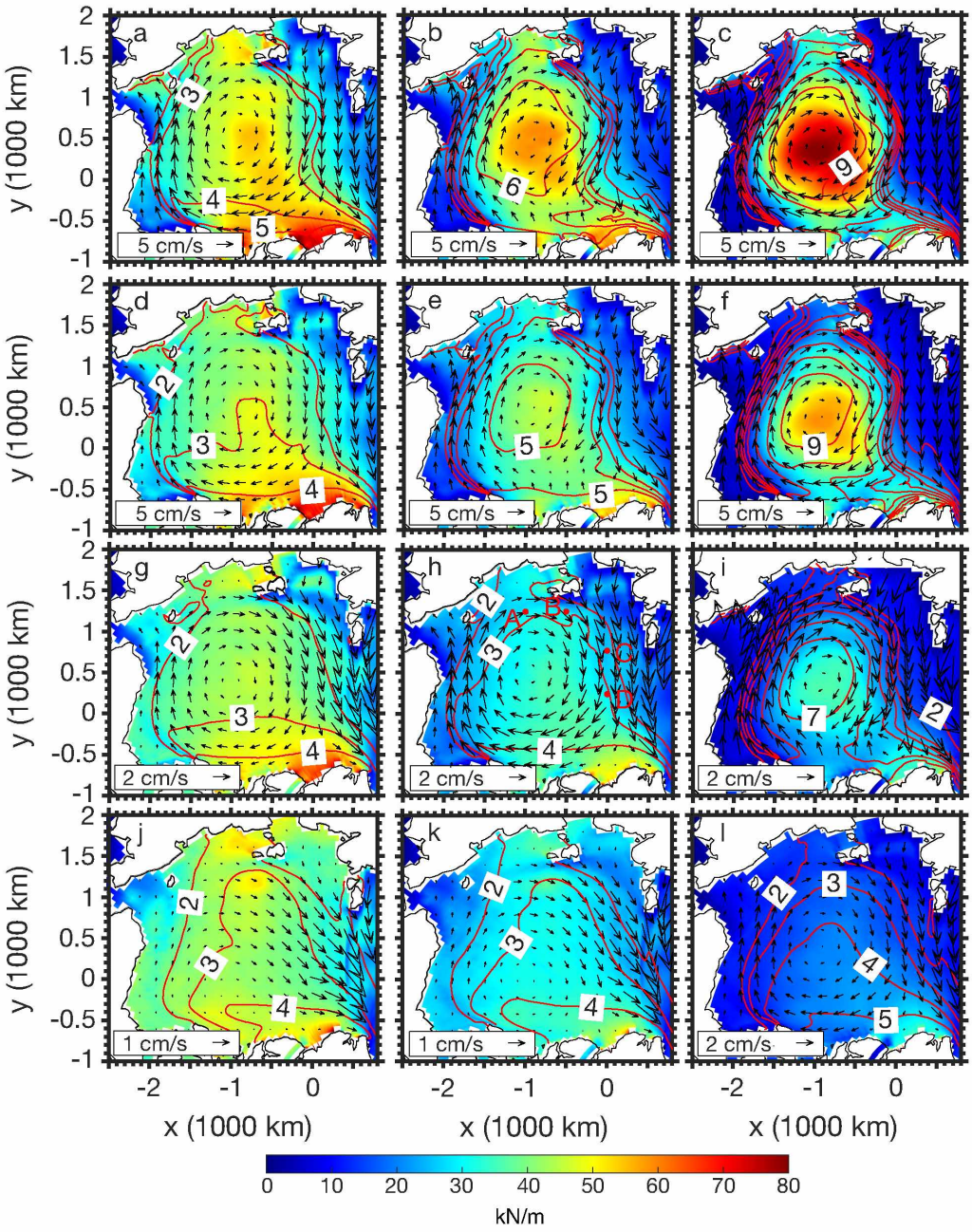

Figure 10. Same experiments as Figure 7, but the color shading represents sea ice strength, and red contours represent the sea ice thickness.

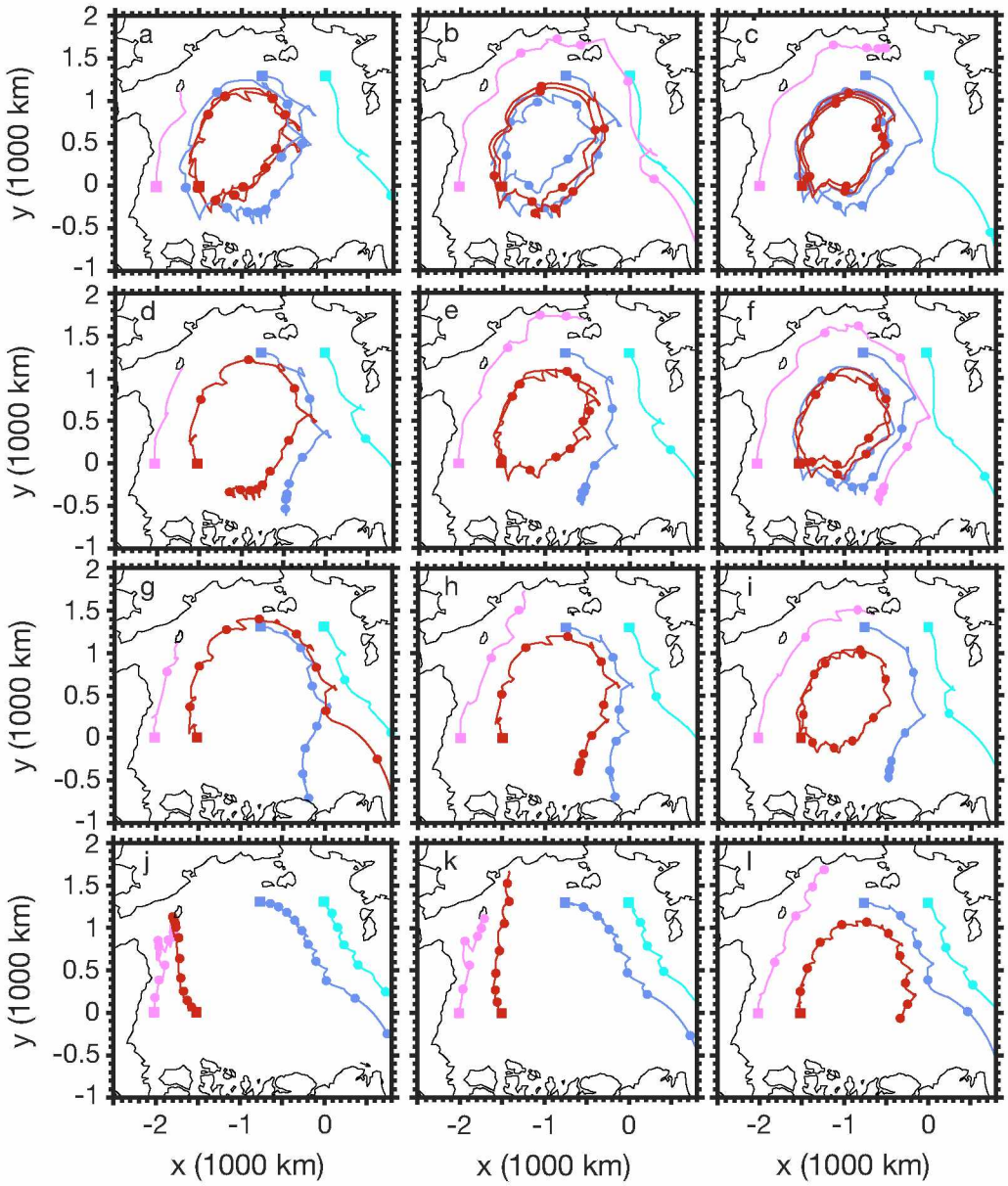

Figure 11. Same experiments as Figure 7, but pathways for four tracers are shown in pink, red, light blue, and cyan, integrated for up to 8 years. The filled squares represent the initial location of the tracer (December 1st), while the filled dots represent the beginning of each model year (January 1st).

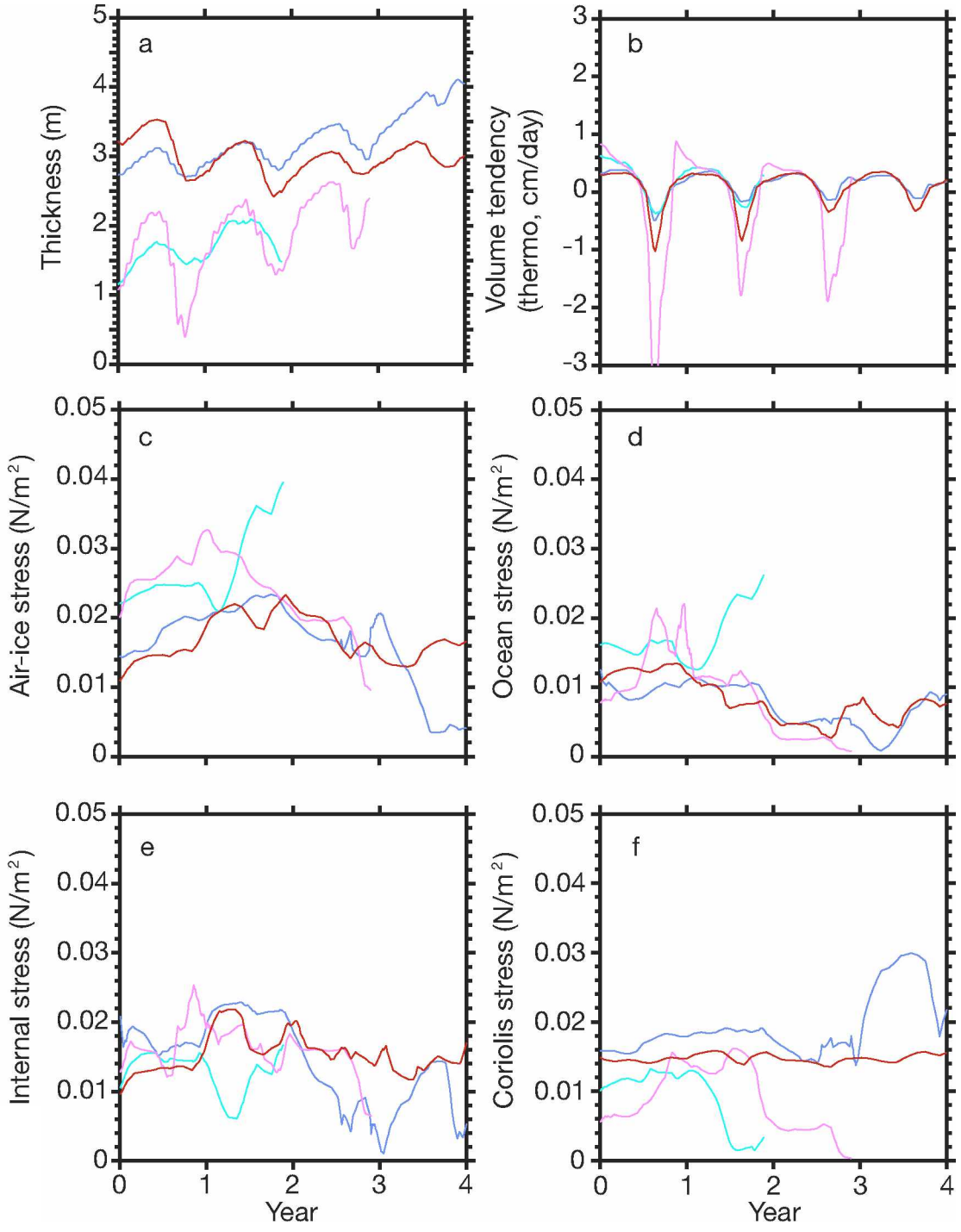

Figure 12. The sea ice properties following the four pathways from the reference case. (a) sea ice thickness, (b) volume tendency due to thermodynamic processes, (c) air/ice stress, (d) ocean stress, (e) Internal ice stress, and (f) Coriolis stress.

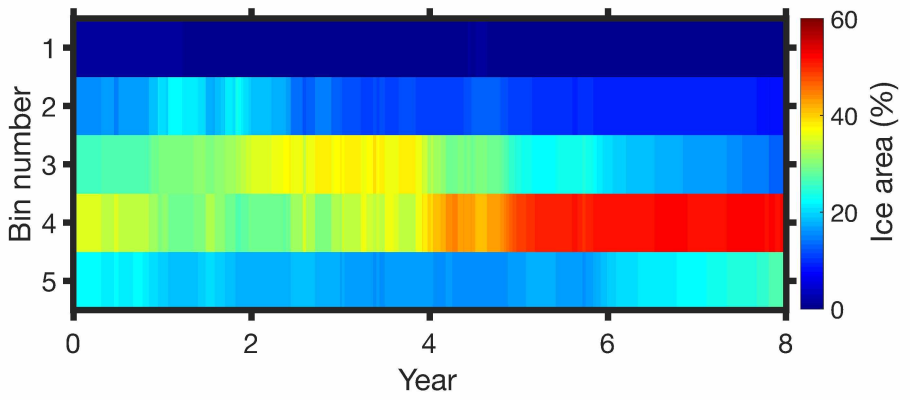

Figure 13. The sea ice thickness distribution following the red pathway from the reference case. The first bin represents the thinnest sea ice thickness category, while bin 5 corresponds to the thickest sea ice. Color represents the area fraction of the sea ice been categorized into each bin.

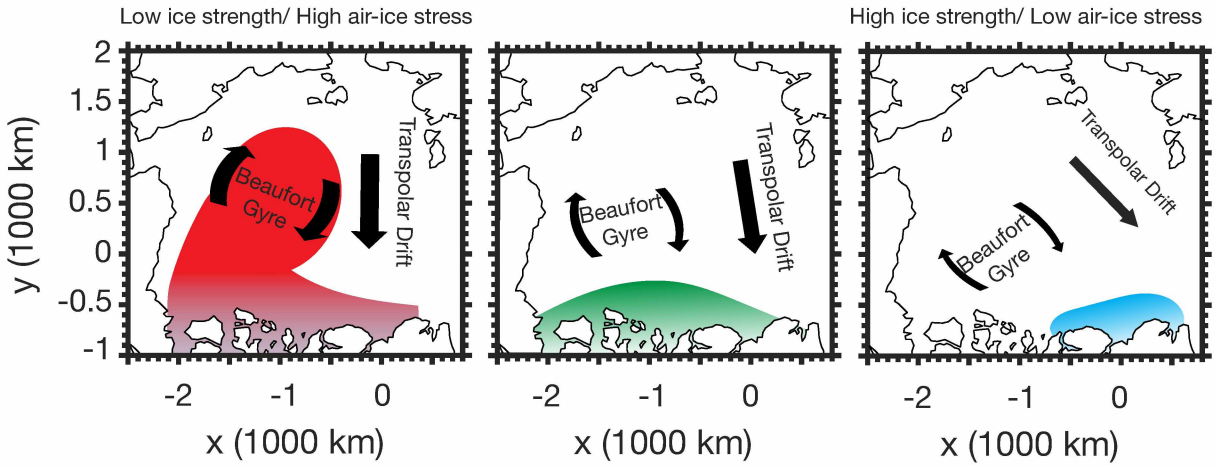

Figure 14. A schematic figure showing the sea ice velocity patterns under (a) low sea ice strength (high air-ice drag), (b) normal sea ice strength (air-ice drag), and (c) low sea ice strength (high air-ice drag) conditions. Red, green, and blue colors represent high, medium, and low sea ice thickness.

3.13 Tables

Table 2. A summary of 25 sensitivity experiment names. W represents wind and S represents sea ice strength. Numbers following W and S represents the coefficient used to modify the magnitude of C_f and c_a respectively.

	$1.0 \cdot C_f$	$0.8 \cdot C_f$	$0.6 \cdot C_f$	$0.4 \cdot C_f$	$0.2 \cdot C_f$
$1.0 \cdot c_a$	W10S10	W10S08	W10S06	W10S04	W10S02
$0.8 \cdot c_a$	W08S10	W08S08	W08S06	W08S04	W08S02
$0.6 \cdot c_a$	W06S10	W06S08	W06S06	W06S04	W06S02
$0.4 \cdot c_a$	W04S10	W04S08	W04S06	W04S04	W04S02
$0.2 \cdot c_a$	W02S10	W02S08	W02S06	W02S04	W02S02

Table 3. Sea ice thickness within DRA

	$1.0 \cdot C_f$	$0.8 \cdot C_f$	$0.6 \cdot C_f$	$0.4 \cdot C_f$	$0.2 \cdot C_f$
$1.0 \cdot c_a$	2.39	2.79	3.77	4.97	7.08
$0.8 \cdot c_a$	2.27	2.52	3.19	4.53	6.53
$0.6 \cdot c_a$	2.27	2.39	2.71	3.93	6.02
$0.4 \cdot c_a$	2.38	2.47	2.62	3.05	4.98
$0.2 \cdot c_a$	2.81	2.86	2.90	2.97	3.51

Table 4. Mean sea ice velocity

	$1.0 \cdot C_f$	$0.8 \cdot C_f$	$0.6 \cdot C_f$	$0.4 \cdot C_f$	$0.2 \cdot C_f$
$1.0 \cdot c_a$	4.14	4.35	4.54	4.76	4.89
$0.8 \cdot c_a$	3.32	3.55	3.78	4.01	4.28
$0.6 \cdot c_a$	2.44	2.65	2.91	3.17	3.51
$0.4 \cdot c_a$	1.53	1.67	1.87	2.19	2.59
$0.2 \cdot c_a$	0.76	0.80	0.87	1.01	1.38

3.14 References

Bitz, C. M., M. M. Holland, A. J. Weaver, and M. Eby (2001), Simulating the ice-thickness distribution in a coupled climate model, *J. Geophys. Res.*, **106**, 2441–2463.

Bitz, C. M., and G. H. Roe (2004), A Mechanism for the High Rate of Sea Ice Thinning in the Arctic Ocean, *J. Clim.*, **17**, 3623–3632.

Cavalieri, D. J., and C. L. Parkinson (2012), Arctic sea ice variability and trends, 1979–2010, *The Cryosphere*, **6**(4), 881–889, doi:10.5194/tc-6-881-2012.

Cavalieri, D. J., C. L. Parkinson, P. Gloersen, and H. J. Zwally (1995), Sea Ice Concentrations from Nimbus-7 SMMR and DMSP SSM/I-SSMIS Passive Microwave Data, Boulder–Colorado USA: National Snow and Ice Data Center. Digital media– 1996– updated 2008, doi:10.5067/8gq8lzqvl0vl.

Cavalieri, D. J., and Coauthors (1991), Aircraft active and passive microwave validation of sea ice concentration from the Defense Meteorological Satellite Program special sensor microwave imager, *J. Geophys. Res.*, **96**(C12), 21989–22008.

Chevallier, M., and Coauthors (2016), Intercomparison of the Arctic sea ice cover in global ocean–sea ice reanalyses from the ORA-IP project, *Clim. Dyn.*, **49**(3), 1107–1136, doi:10.1007/s00382-016-2985-y.

Comiso, J. C. (1996), SSM/I concentrations using the bootstrap algorithm, *NASA Tech. Rep.*, *1380*, 40 pp.

Comiso, J. C. (2002), A rapidly declining perennial sea ice cover in the Arctic, *Geophys. Res. Lett.*, **29**(20), 1956, doi:10.1029/2002GL015650.

Comiso, J. C. (2012), Large Decadal Decline of the Arctic Multiyear Ice Cover, *J. Clim.*, **25**(4), 1176–1193, doi:10.1175/JCLI-D-11-00113.1.

Comiso, J. C. (2017), *Bootstrap Sea Ice Concentrations from Nimbus-7 SMMR and DMSP SSM/I-SSMIS, Version 3.* (Indicate subset used). Boulder, Colorado USA. NASA National Snow and Ice Data Center Distributed Active Archive Center. doi: https://doi.org/10.5067/7Q8HCCWS4I0R. (Date Accessed).

Comiso, J. C., W. N. Meier, and R. Gersten (2017), Variability andtrends in the Arctic Sea ice cover:Results from different techniques, *J. Geophys. Res. Oceans*, **122**, 6883–6900, doi:10.1002/2017JC012768.

Danabasoglu, G., and Coauthors (2012), The CCSM4 Ocean Component, *J. Clim.*, **25**(5), 1361–1389, doi:10.1175/JCLI-D-11-00091.1.

Day, J. J., S. Tietsche, and E. Hawkins (2014), Pan-Arctic and Regional Sea Ice Predictability: Initialization Month Dependence, *J. Clim.*, **27**(12), 4371–4390, doi:10.1175/JCLI-D-13-00614.1.

Dee, D. P. and Coauthors (2011), The ERA-Interim reanalysis: configuration and performance of the data assimilation system, *Q.J.R. Meteorol. Soc.*, **137**(656), 553–597, doi:10.1002/qj.828.

Emery, W. J., C. W. Fowler, and S. L. Pfirman (2002), New Satellite Derived Sea Ice Motion Tracks Arctic Contamination, *Mar. Poll. Bull.*, **35**, 345–352.

Flato, G. M., and W. D. Hibler III (1995), Ridging and strength in modeling the thickness distribution of Arctic sea ice, *J. Geophys. Res.*, **100**(C9), 18611–18626.

Guemas, V. and Coauthors (2014), A review on Arctic sea-ice predictability and prediction on seasonal to decadal time-scales, *Q. J. R. Meteorol. Soc.*, **142**(695), 546–561, doi:10.1002/qj.2401.

Hibler, W. D. (1984), The role of sea ice dynamics in modeling CO_2 increases, *Climate Processes and Climate Sensitivity, Geophys. Monogr.*, **29**, 238–253.

Hibler, W. D., III (1980), Modeling a Variable Thickness Sea Ice Cover, *Mon. Weather Rev.*, **108**, 1943–1973, doi:10.1175/1520-0493(1980)108<1943:MAVTSI>2.0.CO;2.

Hibler, W. D., III (1979), A Dynamic Thermodynamic Sea Ice Model, *J. Phys. Oceanogr.*, **9**, 815–846.

Holland, M. M., C. M. Bitz, E. C. Hunke, W. H. Lipscomb, and L. L. Schramm (2006), Influence of the sea ice thickness distribution on Polar Climate in CCSM3, *J. Clim.*, **19**, 2398–2414.

Holloway, G., and T. Sou (2002), Has Arctic Sea Ice Rapidly Thinned? *J. Clim.*, doi:10.1175/1520-0442(2002)015<1691:HASIRT>2.0.CO;2.

Hopkins, M. A., and W. D. Hibler (1994), On the ridging of intact lead ice, *Ann. Glaciol.*, **99**(C8), 16351–16360, doi:10.3189/1991AoG15-1-81-86.

Hunke, E. C. (2001), Viscous–Plastic Sea Ice Dynamics with the EVP Model: Linearization Issues, *J. Comput. Phys.*, **170**, 18–38, doi:10.1006/jcph.2001.6710.

Hunke, E. C., and J. K. Dukowicz (1997), An Elastic–Viscous–Plastic Model for Sea Ice Dynamics, *J. Phys. Oceanogr.*, **27**, 1849–1867.

Hunke, E. C., and W. H. Lipscomb (2008), CICE: The Los Alamos Sea Ice Model. Documentation and software user's manual version 4.0, *Tech. Rep. LA-CC-06-012*, T–3 Fluid Dyn. Group– Los Alamos Natl. Lab.– Los Alamos–N. M.

Kimura, N., and M. Wakatsuchi (2000), Relationship between sea-ice motion and geostrophic wind in the northern hemisphere, *Geophys. Res. Lett.*, **27**(22), 3735–3738, doi:10.1029/2000GL011495.

Kreyscher, M., H. Harder, P. Lemke, and G. M. Flato (2000), Results of the Sea Ice Model Intercomparison Project: Evaluation of sea ice rheology schemes for use in climate simulations, *J. Geophys. Res.*, **105**, 11,299– 11,320.

Kwok, R., and D. A. Rothrock (2009), Decline in Arctic sea ice thickness from submarine and ICESat records: 1958-2008, *Geophys. Res. Lett.*, **36**, L15501, doi:10.1029/2009GL039035.

Levitus, S., and T. P. Boyer (1994), LEVITUS94 Ocean Climatology, *World Ocean Atlas Volume Temperature. NOAA Atlas NESDIS*, US Government Printing Office: Washington–DC. Available from: (Accessed 13 November 2018)

Lindsay, R. W. (2013), Unified Sea Ice Thickness Climate Data Record, http://psc.apl.washington.edu/sea_ice_cdr/, Polar Sci. Cent., Appl. Phys. Lab., Univ. of Wash., Seattle.

Lipscomb, W. H. (2001), Remapping the thickness distribution in sea ice models, *J. Geophys. Res.*, **106**(C7), 13989–14000.

Lipscomb, W. H., E. C. Hunke, W. Maslowski, and J. Jakacki (2007), Ridging, strength, and stability in high-resolution sea ice models, *J. Geophys. Res.*, **112**(C3), C06005–18, doi:10.1029/2005JC003355.

McPhee, M.G. (1986), The upper ocean, in The Geophysics of Sea Ice, edited by N. Untersteiner, pp. 339-394, Plenum, New York.

Maslanik, J., J. Stroeve, C. Fowler, and W. Emery (2011), Distribution and trends in Arctic sea ice age through spring 2011, *Geophys. Res. Lett.*, **38**(13), doi:10.1029/2011GL047735.

Miller, P., S. Laxon, D. Feltham, and D. Cresswell (2006), Optimization of a sea ice model using basinwide observations of Arctic sea ice thickness, extent, and velocity, *J. Clim.*, **19**, 1089–1108.

Rigor, I. G., and J. M. Wallace (2004), Variations in the age of Arctic sea-ice and summer sea-ice extent, *Geophys. Res. Lett.*, **31**, L09401, doi:10.1029/2004GL019492.

Rigor, I. G., J. M. Wallace, and R. L. Colony (2002), Response of Sea Ice to the Arctic Oscillation, *J. Clim.*, **15**, 2648–2663.

Rothrock, D. A., D. B. Percival, and M. Wensnahan (2008), The decline in arctic sea-ice thickness: Separating the spatial, annual, and interannual variability in a quarter century of submarine data, *J. Geophys. Res.*, **113**, C05003, doi:10.1029/2007JC004252.

Rothrock, D. A., and M. Wensnahan (2007), The Accuracy of Sea Ice Drafts Measured from U.S. Navy Submarines, *J. Atmos. Oceanic Technol.*, **24**(11), 1936–1949, doi:10.1175/JTECH2097.1.

Rothrock, D. A., J. Zhang, and Y. Yu (2003), The arctic ice thickness anomaly of the 1990s: A consistent view from observations and models, *J. Geophys. Res.: Oceans*, **108**(C3), doi:10.1029/2001JC001208.

Steele, M., J. Zhang, D. A. Rothrock, and H. Stern (1997), The force balance of sea ice in a numerical model of the Arctic Ocean, *J. Geophys. Res.*, **102**, 21061–21079.

Steffen, K., and A. Schweiger (1991), NASA team algorithm for sea ice concentration retrieval from Defense Meteorological Satellite Program special sensor microwave imager: Comparison with Landsat satellite imagery, **96**(C12), 21971–21987.

Stroeve, J., A. Barrett, M. Serreze, and A. Schweiger (2014), Using records from submarine, aircraft and satellites to evaluate climate model simulations of Arctic sea ice thickness, *The Cryosphere*, ***8***(5), 1839–1854, doi:10.5194/tc-8-1839-2014.

Thorndike, A. S., and R. L. Colony (1982), Sea ice motion in response to geostrophic winds, *J. Geophys. Res.*, **87**, 5845–5852.

Thorndike, A. S., D. A. Rothrock, G. A. Maykut, and R. L. Colony (1975), The Thickness Distribution of Sea Ice, *J. Geophys. Res.*, **80**(33), 4501–4513.

Tschudi, M., C. Fowler, J. Maslanik, and J. Stroeve (2010), Tracking the Movement and Changing Surface Characteristics of Arctic Sea Ice, *IEEE J. Sel. Top. Appl. Earth Observations Remote Sensing*, **3**(4), 536–540, doi:10.1109/JSTARS.2010.2048305.

Tucker, W. B., III, J. W. Weatherly, D. T. Eppler, L. D. Farmer, and D. L. Bentley (2001), Evidence for rapid thinning of sea ice in the western Arctic Ocean at the end of the 1980s, *Geophys. Res. Lett.*, **28**(14), 2851–2854.

Watanabe, E., J. Wang, A. Sumi, and H. Hasumi (2006), Arctic dipole anomaly and its contribution to sea ice export from the Arctic Ocean in the 20th century, *Geophys. Res. Lett.*, **33**, L23703, doi:10.1029/2006GL028112.

Wu, B., J. Wang, and J. E. Walsh (2006), Dipole Anomaly in the winter Arctic atmosphere and its association with Arctic sea ice motion, *J. Clim.*, **19**, 210–225.

Yu, Y., G. A. Maykut, and D. A. Rothrock (2004), Changes in the thickness distribution of Arctic sea ice between 1958-1970 and 1993-1997, *J. Geophys. Res.*, **109**, C08004, doi:10.1029/2003JC001982.

Zhang, J., D. A. Rothrock, and M. Steele (2000), Recent Changes in Arctic Sea Ice: The Interplay between Ice Dynamics and Thermodynamics, *J. Clim.*, doi:10.1175/1520-0442(2000)013<3099:RCIASI>2.0.CO;2.

Chapter 4 A Comprehensive Composite Study of the Storm Impact on Sea Ice[3]

Abstract

Combining the ERA-Interim reanalysis data and satellite observations, the storm impact on sea ice during 1979-2018 is examined based on a new composite analysis in a statistical manner. We split the Arctic into seven regions and categorized storms into different regions based on their pathway. This analysis is based on fixed composite frameworks with respect to sea ice instead of following storm tracks and provides a region-by-region discussion on how storms impact sea ice. Variations on the storm climatology and sea ice conditions are also examined within the same time periods and regions. Over the periphery seas, storms tend to reduce sea ice area compared with the climatological values starting from two days before the storm arrived and last for five to seven days in total. Sea ice tends to recover/exceed the climatological values within one or two weeks after the storm passed. Storms reaching the Central Arctic, on the other hands, tend to result in less sea ice area even two weeks after the storm passed. The total sea ice area over the Central Arctic is highly correlated with the number of storms. Overall, storms tend to cause sea ice area change within a radius of 400-500 km nearby the storm center with a maximum impact within 200 km.

---

[3] Peng L. X. Zhang, J. Zhang, Y. Yang, and J. H. Kim. In Preparation for Journal of Climate, Transient impacts of Arctic Storm on Sea Ice: Regional and Seasonal Analysis.

4.1 Introduction

Many studies have shown Arctic storms tend to have strong impacts on sea ice via both thermodynamic and dynamic processes. Storms transport heat and moisture into the Arctic (e.g. Overland and Turet, 1994; Sorteberg and Walsh, 2008) and may cause sea ice retreat (Boisvert et al., 2016). A higher amount of clouds induced by storms may enhance downward longwave radiation and reduce shortwave radiation, therefore, impact on the surface energy budget (e.g. Curry et al., 1993; Intrieri et al., 2002). Storms also lead to strong surface winds, which may enhance upward heat transport from the ocean (e.g. Pickart et al., 2009; Steele and Morison, 1993; Yang et al., 2001; Yang et al., 2004) causing rapid bottom sea ice melting (Zhang et al., 2013). Dynamically, storms often cause sea ice deformation, forming leads, cracks, and polynias and potentially more vulnerable towards external forcings (Parkinson and Comiso, 2013). Satellite and ice-drift buoy observations over the Canada Basin show the low pressure over the surface may cause sea ice divergence (Brümmer et al., 2008), and therefore, reduce the sea ice concentration (Maslanik and Barry, 1989) during the summer. Furthermore, sea ice export through the Fram Strait may also be enhanced by storms (Brümmer and Hoeber, 1999; Brümmer et al., 2001; Wei et al., 2019).

Storm case studies often focused on extreme storms, investigating either thermodynamic or dynamic processes over limited time and regions (e.g., Simmonds and Rudeva, 2012; Boisvert et al., 2016). It is difficult to draw general conclusions based on these sparse case studies. Due to complex air-ice-ocean interactions, direct linkage between storm (e.g. counts, duration, and intensity) and sea ice characteristics (e.g. sea ice area, extent, and concentration) via simple linear regression is also difficult to provide (Rae et al., 2017). Additionally, sea ice circulation

can be impacted by the large-scale atmospheric circulations (Rigor et al., 2002), therefore, differences of sea ice properties between high and low storm years are not a direct evidence showing the storm impact on sea ice since storms may also be impacted by large-scale atmospheric circulations (Serreze et al., 1997; Simmonds et al., 2008). Based on model simulations from 2006 to 2008, the composite analysis by Kriegsmann and Brümmer, (2014) provided the first 2-D composite fields around the storm center (without any rotation of the frame) to study storm impact on sea ice from both dynamic and thermodynamic processes from a statistical point of view. Three-year periods adapted by their study may include a sufficient number of storm samples to explain how storms impact sea ice via basic physical processes. However, it is still too short to explain further the long-term storm impact on sea ice keeping in mind changing sea ice and storm climatology. Additionally, storms usually travel for a long distance, and changes in composite sea ice conditions around the storm center are not based on the same location. Therefore, conclusions from this study could potentially be biased due to inhomogeneity of the horizontal sea ice concentration/thickness distributions, impact from different oceanography/landscape conditions, and even controlled by different air masses.

Our composite analysis is different from the previous studies in several ways. First, our composite framework does not move relative to sea ice, which gives us the opportunity to examine sea ice changes over the same location before, during, and after a storm's passage. Composite sea ice changes over the same region also assure that sea ice is facing similar climatological external forcing conditions, and we are more confident that the variations in sea ice properties are primarily due to the storm. Second, we composite storms and sea ice conditions into seven regions covering the entire Arctic. The selection of those regions has considered not only their geophysical locations but also the bathymetry. Therefore, we expect

the climatological external forcing for sea ice is similar within the selected regions. Third, our study includes all storms span from 1979 to 2018 and we continuously track variations of sea ice conditions, around all detected storm centers, one week before and two weeks after the storm passage. Inspired by many storm case studies, the pre-storm sea ice condition is an important reference in quantifying the storm impact along with the climatology sea ice decreasing rate. Therefore, in this study, we use a three-week time window to examine whether storm induced sea ice changes will have transient or long-term effects. The length of our time window prevents sea ice changes due to variations in the large-scale atmospheric circulations but only focusing on synoptic-scale storms. Forth, we assume sea ice change is quasi-symmetric relative to the center of the storm, therefore, instead of compositing fields into a 2-D horizontal plane and considering the orientations of the frame, we only look for sea ice changes in the radial direction. Five, we split storms into four ten-year windows and compare variations in the sea ice area during the storm period with their corresponding climatology, which is estimated every decade.

Through this study, we strive to answer the following questions:

a. Do storms have large short-term, mid-term, and long-term impact on sea ice area over different regions?
b. How long and how far can a storm impact sea ice area?
c. What type of storms tends to have large impacts on sea ice area?

This paper is divided into six sections. Specifically, Section 4.2 describes the data we used for this study. Section 4.3 provides details on the storm detection method and how we quantify the storm impact on sea ice via composite analysis. Section 4.4 examines the storm impact on sea

ice with respect to seasonal, interannual, and regional differences. Section 4.5 focuses on discussing specific physical processes relating storm impact on sea ice. The conclusion is given in Section 4.6.

4.2 Data

The observational sea ice area data sets were obtained from the National Snow and Ice Data Center (NSIDC). The daily averaged sea ice concentration used by this study covers October 26, 1978 to December 31, 2018. The data set has been derived from the Nimbus-7 Scanning Multichannel Microwave Radiometer (SMMR), the DMSP Special Sensor Microwave Imager (SSM/I), and the DMSP Special Sensor Microwave Imager and Sounder (SSMIS) Passive Microwave Data, Version 3 (abbreviated as SSM/I; Comiso, 2017) (https://nsidc.org/data/NSIDC-0079) and generated using the Advanced Microwave Scanning Radiometer - Earth Observing System (AMSR-E) Bootstrap Algorithm. The spatial resolution for these data sets is 25 km × 25 km.

4.3 Approaches

Storm track detection algorithm

Similar to previous storm detection algorithms (Serreze, 1995; Serreze et al., 1997), we applied our algorithm to sea level pressure (SLP) in the ERA-Interim reanalysis dataset. The spatial and temporal resolution of the reanalysis data is $0.75^{o}\times0.75^{o}$ latitude-longitude grid and 6-hourly respectively. We use the tracking algorithm to identify storms from 30^{o}N north span from 1979 to 2018. Briefly, we summarize our tracking algorithm in the following steps. We first plot the SLP over a square polar stereographic map and convert geographic locations (longitude and

latitude) to a planar, projected map coordinate system. In the following steps, we detect and track low centers based on the new coordinate system and convert back to geographic locations at the end. The main purpose of this step is to simplify treatments when storm tracks cross the pole or Greenwich line. In determining the low center candidates, we did not set restrictions on the minimum distance between two low centers. Instead, we search for local minimum SLP over adjacent points through each row and column and two diagonals crossing each element. Only local minimum SLPs smaller than the average SLP north of 60°N minus two standard deviations will be considered as low center candidates in the following step. This step successively filtered out thermal lows over the continents and gives us the potential to consider storm splintering and merging processes in the following analysis. We combine successive 6-hourly SLP maps to determine storm tracks. If a low center candidate is within a radius r of a low center's location at the previous time step, we consider the two low center candidates belong to the same storm track. Otherwise, we start another track for the new low center candidate. Different to previous storm track algorithms, the same low center candidate can belong to multiple storm tracks if it satisfies the condition mentioned above. This condition aims to describe the storm merging/splitting process. The threshold value for r was determined empirically (r = 650 km) by manually comparing storm track results from different settings. We tested and documented all storm tracks by using r span from 100 to 2000 km in a 50 km interval. In general, a larger magnitude of r corresponds to a smaller storm count but longer duration. Only storm durations exceeding two days have been taken into account for this study.

We categorized storms into four fixed periods: 1979-1988, 1989-1998, 1999-2008, and 2009-2018. Storms were detected starting from 1979 continuously to 2018. Therefore, if storms have been first detected by the end of one ten-year time period and span to the following time period,

that storm will be counted by both time periods. Within each time periods, we define four seasons as winter (December, January, and February), spring (March, April, and May), summer (June, July, and August), and autumn (September, October, and November). We used similar treatment as mentioned earlier if the storm spans two seasons/years.

Quantifying the storm impact on sea ice

To quantify the storm impact on sea ice, we group storms into seven regions (Figure 15) according to their center locations. The same storm can be categorized into different groups as it moves from one region to another during its lifetime. The selection of seven regions is based on the bathymetry and circulation of the surface water and intermediate Pacific and Atlantic origin water over the Arctic Ocean (Polyakov et al., 2012).

To quantify the storm impact on regional sea ice, we convert the Lagrangian perspective in terms of storm tracks to the Eulerian perspective in terms of averaged sea ice properties (Figure 16). According to the 6-hourly storm track information, we estimate the average sea ice/energy properties (e.g. sea ice area) nearby the storm center within a radius r^* spanning from 100 km to 1200 km with a 100 km interval along the storm track. According to the time when the storm moves to the location of the specific storm center, we start to record the averaged sea ice/energy properties at all r^* ranges from one week before to two weeks after the storm's arrival. We define the time relative to the storm's arrival as t_{lag}, which has negative and positive values before and after the storm's arrival in our framework respectively.

We define the sea ice area in a five-day interval starting from 7 days to 3 days before the storm's arrival ($t_{lag} = -7$ day to $t_{lag} = -3$ day) as the pre-storm sea ice condition (Pre-SC). The linear

trend of the climatological sea ice area was estimated during the Pre-SC using the least squares analysis (Figure 17). According to the sign of the trend (S_{Pre-SC}), storms are categorized into two groups: $S_{Pre-SC} > 0$ (G_1 group) and $S_{Pre-SC} < 0$ (G_2 group). Most storms categorized in the G_1 group occur during the autumn and early winter seasons, while in the G_2 group occur during the spring and summer seasons. When the ocean is fully covered by sea ice, sea ice area does not change during the Pre-SC, and storms are categorized neither into G_1 or G_2 groups. The standard deviation of the sea ice area difference ($\sigma_{\delta A}$) between the fitted and observed values during the Pre-SC are used to represents the natural variations of the local sea ice area before the storm arrives. As the storm approaches, we define the storm condition (SC) as a five-day period centered at the storm's arrival time ($t_{lag} = -2$ days to $t_{lag} = 2$ days). Following the same S_{Pre-SC}, we extrapolate the sea ice area to $t_{lag} = 2$ days. If the sea ice area difference (δA) is larger than $+2\sigma_{\delta A}$, we categorize storms into the positive phase group (G_1^+ or G_2^+). Similarly, storms are categorized into the negative phase group (G_1^- or G_2^-) if the δA is smaller than the $-2\sigma_{\delta A}$. The rest of the storm cases are categorized in the neutral phase group (G_1^0 and G_2^0). Finally, after the storms move away ($t_{lag} = 3$ day to $t_{lag} = 14$ day), we define the post-storm condition (Post-SC).

Additionally, we also compared the sea ice/energy properties under the Pre-SC, SC, and Post-SC with the climatological condition (CC) values (Pre-CC, CC, and Post-CC), which was estimated at each storm center within the circle corresponding to radius r^* ($r^* = 100. km\ to\ r^* = 1200\ km$). The CC values are estimated based on the time and location of the storm center. Excluding the storm year, CC sea ice/energy properties are averaged over nine years encompassed by the aforementioned ten-year window at the same time and location corresponding to the storm. Combining storms categorized into each groups (G_1^+, G_2^+, G_1^0, G_2^0, G_1^- and G_2^-), we have two

probability distributions functions (PDFs) at every t_{lag} and r^*, naming $PDF_{CC}(t_{lag}, r^*)$ and $PDF_{SC}(t_{lag}, r^*)$ corresponding to the climatology and storm condition respectively. Comparing PDF_{CC} and PDF_{SC} allows us to test the null hypothesis: the storm does not have a significant impact on sea ice/energy properties $(H_0: \mu_{PDF_{CC}} = \mu_{PDF_{SC}})$. We, therefore, consider the storm causing statistically significant changes compared with the CC if $p < 0.05$.

4.4 Storm Tracks Statistical Analysis

We examined the storm counts using ERA-Interim re-analysis over seven selected regions. Deep storms are separated from shallow storms if the minimum central mean sea level pressure along the storm track is below 990 hPa. From 1979 to 2018, the average total number of storms over all seven selected sectors is 564 (Table 5). Both GIN and the Chukchi Sea show a statistically significant increase in the storm number (2.74 and 0.40 per year respectively), especially during the winter season (0.17 and 0.97 per year respectively). The increasing storm counts over Chukchi Sea but no significant increase over Bering Sea suggest that storms are more likely to penetrate through the Bering Strait and enter the Chukchi Sea during the winter over recent decades. During the spring, a significant increasing trend can be found over the Barents and Kara Seas (0.28 per year), and during the summer over East Siberian and the Laptev Sea (0.17 per year).

In general, a higher percentage of storms occurring during the winter and fall are deep storms. More than 50% of storms over the GIN, Bering, and the Chukchi Seas are deep storms especially during the winter season (Table 6). Deep storms over the GIN Seas tend to increase throughout the year except for the summer season (Figure 19e). Overall, the increasing trend for deep storms is smaller than the trend for total storm counts.

4.5 Changes in Sea Ice

As shown by Figure 20, the sea ice area changes have large regional, seasonal, and interannual variabilities. The monthly trends of the sea ice area are summarized in Figure 21. Both figures are applied to seven regions mentioned in Section 4.3, spanning from 1979 to 2018 and following similar methods as Onarheim et al., (2018). In this section, we shed light on why we need to categorize storms into G_1 and G_2 groups (Section 4.4) when discussing the role of storms on sea ice over different regions.

Categorizing storms into G_1 and G_2 groups allow us to inherently consider seasonal variations of the regional sea ice conditions. Overall, storms categorized into the G_1 group occurred when regional sea ice area is on its increasing trends, while storms in the G_2 group exhibit decreasing trends. For example, the annual sea ice area shows a clear seasonal cycle over the GIN, Kara, and Barents Seas. The maximum sea ice area is obtained in March or April and slightly earlier over GIN Seas compared with Kara and Barents Seas. After the sea ice obtains the maximum sea ice area over Kara and Barents Seas, there is a sharp sea ice area decrease starting from April to August. Due to excessive sea ice area decrease during the winter in GIN Seas, sea ice decreases at a much slower rate until the end of June over recent decades. In both regions, the minimum sea ice area can be found in September. Therefore, most storms categorized into the G_1 group span from October to March/April, while the G_2 group spans from March to August in both regions.

Categorizing storms into G_1 and G_2 groups also help us to exclude storms that have less or no impact on sea ice area when the ocean is fully covered by sea ice or sea ice is completely melted. Over Chukchi, East Siberian, Laptev, Central Arctic, and Beaufort Seas, the ocean is fully covered by sea ice during the winter and spring and only opened through the summer and fall (Figure 20).

Over the Chukchi Sea, the sea ice area gradually decreases starting from May to August and reaches the annual minimum in September, after which the sea ice gradually increases until November or December. The sea ice area over the East Siberian and Laptev Seas show a much slower decreasing rate in June but decreases rapidly starting from July until August. The largest sea ice decreasing trends are found over the East Siberian, Laptev, and Barents Kara Seas. The former obtains the largest decreasing trends from August to October, while the later has a larger decreasing trend over the shoulder months (June, July, August, October, November, and December). Over the Bering Sea, sea ice becomes completely melted starting from July to September in 1979-1988, and the ice-free period extends to October for the following time periods (1989-1998, 1999-2008, and 2009-2018).

Therefore, grouping storms according to the increasing or decreasing sea ice area trends under Pre-SC provide a more objective way to explore the storm impact on sea ice compared to grouping storms according to seasons. Additionally, instead of four seasons, this method also simplified the situation into two conditions, either the sea ice area increases or decreases before the storm arrives.

4.6 Relationships between Storms and Sea Ice

In this section, we focused on exploring the short-term (five days) and mid-term (one to two weeks) storm impact on sea ice over seven regions.

a. Bering Sea

The PDF of the number of storms found in the Bering Sea categorized into G_1^+, G_1^0, and G_1^- are shown in Figure 22, while G_2^+, G_2^0, and G_2^- in Figure 23. An apparent seasonal difference is shown in Figure 22 and Figure 23. Under the Pre-SC, the sea ice area tends to increase (Figure 23) from November to the following March and decrease from February to June (Figure 23). Most storms

causing sea ice area increase slower than the Pre-SC (storms categorized into the G_1^- group) during the winter (Figure 22) and decrease faster than the Pre-SC in January to April. Generally, more storms are categorized in the G_2^- group before May, and the number of storms in the G_2^+ group tend to exceed G_2^- group starting from May.

Among the seven selected regions, storms passing through the Bering Sea are above 100 every year. Therefore, the climatology of the sea ice area is highly impacted by storms. The composite analysis shown in Figure 24 allows us to have a general picture on how storms impact sea ice at different r^* and t_{lag}. In this figure, we focused on the sea ice area difference between the storm condition (SC and Post-SC) and the climatology condition (CC and Post-CC) for all storms in G_1^+, G_1^-, G_2^+, and G_2^- groups from top to bottom. Positive values represent the total sea ice area within the circle of radius r^* and at the storm relative time t_{lag} in the SC or Post-SC is larger than CC or Post-CC for a certain group of storms. This difference is further divided by the total area of the circle with radius r^* and is shown as an area percentage in Figure 24.

Most sea ice area differences relative to the climatology are within a radius of 400 km. Sea ice variations induced by storms with a radius larger than 200 km relative to the storm center tend to recover to the climatology trends after about a week, while only changes within 200 km tend to produce a mid-term impact on sea ice area. Generally, storms may either cause larger or smaller sea ice area than the climatology within two days (SC), and such impact may reverse during the Post-SC.

b. Chukchi Sea

Less than half of the storms over the Bering Sea eventually go into the Chukchi Sea, and this number has tended to increase over recent years (Table 5). The PDF of the number of storms

categorized into G_1^+ and G_1^- are shown in Figure 25, while G_2^+ and G_2^- in Figure 26. Most storms are categorized into the G_1 group starting from September to December, while storms are categorized into G_2 groups starting from June to September. Due to the full sea ice coverage during the winter and spring (Figure 20), storms only have limited impact on sea ice area changes. However, as the total sea ice area decreased over the Chukchi Sea between 2009 and 2018, the sea ice area tended to have fluctuations during winter and spring, but the sea ice area still follows the same changing rate as the Pre-SC when storms approached.

Storms over the Chukchi Sea may have an impact on the seasonal sea ice decreasing trend through the phase shift between the number of storms categorized into G_2^+ and G_2^- group. During 1989-1998, more storms tend to cause sea ice decline faster (G_2^- group) or remain the same speed (G_2^0 group) as compared with Pre-SC (Figure 26) in May and June for r^* <400 km. During 2009-2018, only June shows such patterns. Starting from July to August, the number of storms in the G_2^+ group increases to balance or even exceed the number of storms categorized in G_2^-, meaning most storms tend to cause sea ice area larger than predicted according to the Pre-SC trends. During 1999-2008 and 2009-2018, this phase shift between the number of storms categorized into the group G_2^+ and G_2^- tended to diminish. The number of storms in both G_2^+ and G_2^- tended to reach maximum during July and August and the total number of storms in G_2 decreased sharply during October. The PDF also tended to extend into earlier months and become broader in the last ten-year period. However, storms did not show significant short-term impact on sea ice during early months during 2009-2018.

Starting from September (Figure 26), more storms are categorized in the G_1 group instead of G_2 group, and the PDF becomes narrower compared with the G_2 group. The maximum number of

storms in G_1^+ and G_1^- are obtained in October/November. During the early half of the periods 1979-1988 and 1989-1998, the majority of storms in the G_2 group are found in October. As the total sea ice area decreased over the Chukchi Sea during the second half of the periods 1999-2008 and 2009-2018, more storms in the G_2 group are found in November and the distribution becomes broader. As shown in Figure 20, a larger sea ice area in September corresponds to a smaller sea ice increasing rate until October, which explains why more storms in G_1 group are found in October in 1979-1988. As sea ice area in September becomes smaller in 2009-2018, a much larger sea ice increasing rate in earlier months result in a broader PDF and the mode of the PDF shifted to November.

As shown by Figure 27, storms can either cause larger or smaller sea ice area compared with climatological values, and the storms' impact on sea ice show large interannual and seasonal variations. As a storm moves towards the sea ice, its impact gradually increases from a larger distance at $t_{lag} = -2$ day to a smaller r^* at $t_{lag} = 0$ day and later time period. In 1979 to 1988, storms categorized in the G_1^+ group caused a strong sea ice decrease before the storm center arrived, and the sea ice area increases faster than the Pre-SC afterward. During SC, the sea ice area is still much lower than the CC but nearly equals or exceed to the CC one week after the storm passed. Similarly, from 1999 to 2008, storms in the G_1^+ group cause sea ice area to become significantly larger than the CC two days after storms moved away. In 1989-1998 and 2009-2018, storms in the G_1^+ group have a much smaller impact on sea ice area, but storms still cause sea ice area larger than the CC. A more profound impact comes from the G_1^- group. Most storms result in much smaller sea ice area compared with the CC and extend their impact to seven days or even longer periods.

Storms over the Chukchi Sea tend to cause rapid sea ice changes within the circle of radius less than 500 km, and their maximum impacts often occur within a radius less than 200 km. Autumn storms (G_1^+ and G_1^- group) tend to have a larger and longer impact on sea ice compared with summer storms (G_2^+ and G_2^- group).

c. East Siberian and Laptev Seas

Over the East Siberian and Laptev Seas, more storms tend to cause sea ice area to decrease faster than the Pre-SC (G_2^- group) during June and July (Figure 28), and a balance tends to be established during August. After that, more storms are categorized into the G_2^+ group during September. Within the same month, the sea ice area starts to increase in the Pre-SC, and the number of storms in the G_1^+ group is larger than in the G_1^- group, meaning more storms tend to cause sea ice area to increase faster than Pre-SC (Figure 29). In October, storms in the G_1^- group become more numerous compared with September storms. In 1979-1988 and 1989-1998, more storms caused sea ice area decreases faster than Pre-SC in October, but the opposite is true starting from 1999 to 2018. A larger fraction of storms tended to cause sea ice increase (G_1^+ group) during 2009-2018. Compared with the Chukchi Sea, storms tended to have a larger impact on sea ice over the East Siberian and Laptev Seas compared with the climatological conditions (Figure 30).

d. Barents and Kara Seas

Storms passing over the Barents and Kara Seas can have impacts on sea ice area throughout the year. As sea ice area increases during the winter and spring seasons in the Pre-SC, more storms tend to cause sea ice increase faster than the Pre-SC during October and November and slower during December (Figure 31). Sea ice area starts to consistently decrease from May, and most storms tend to slow down the sea ice area decreasing rate during March, April, and May. An

increase in the number of storms in the G_2^- group in June, July, and August indicates that storms tend to cause more sea ice decrease compared with the Pre-SC (Figure 32).

The composite analysis (Figure 33) shows that during the first ten-year period (1979-1988), storms in all four groups tend to cause sea ice area above the climatology value. Starting from 1989 to 2018, storms in the G_1^+ group tend to cause sea ice area less than the climatology value, but the impact tends to reverse two-day after the storm passed. Storms categorized in the G_2^+ and G_2^- groups tend to cause sea ice larger than the climatology value, and their impact reduced during recent years (2009-2018).

e. GIN Seas

Similar to the Bering Sea, the magnitude of the storm impact on sea ice over the GIN seas is relatively small compared with other regions. The PDF for storms in the G_1 and G_2 groups almost spans for the entire year and does not have significant variations with different magnitude of r^*. A multi-mode distribution can be found for storms categorized in the G_2 group (Figure 34). The largest mode can be found during in March (1989-1998 and 2009-2018) and February (1999-2008). The second mode appears during July and August. The number of storms in the G_2^+ and G_2^- groups generally balance each other during the winter season, while G_2^- groups tends to exceed G_2^+ groups during the summer. Storms categorized in the G_1 groups only have one mode during the winter or spring (Figure 35).

The composite analysis suggests storms tend to have small impact on sea ice compared with their climatology. This is also due primarily to the large number of storms passing over the GIN Seas, which already impact on the climatological values, therefore, individual storms in the ten-year window do not show significant impact on sea ice.

f. Beaufort Sea

Compared with other regions, storms passing over the Beaufort Sea have the smallest counts each year. Therefore, the composite analysis includes many fewer storm cases compared with other regions. The PDF for storms categorized in G_1^+ and G_1^- groups peaked during the autumn of 1979-1988 and summer of 2009-2018, but not enough storm cases are categorized in G_1^+ and G_1^- groups during 1989-1998 and 1999-2008 period (Figure 37).

g. Central Arctic

Unlike the periphery seas mentioned above, storm impact on sea ice over the Central Arctic show different features. When the sea ice close to its annual minimum in autumn, storms tend to have a large impact on sea ice for both the G_1 and G_2 groups (Figure 40 and Figure 41). As sea ice decreased over recent decades, the PDF for storm counts in different groups become broader. Composite analysis further indicates that storms consistently causing the sea ice less than the climatology within and after two weeks of the storms' passage (Figure 42).

4.7 Discussions

How does storm impact sea ice under the SC?

As an example, Figure 43 shows the composite fields of the surface wind, temperature, and energy terms for storms passing through the Chukchi Sea. As shown by the previous section, storms in all four groups tend to cause sea ice area decrease by the end of SC. Most storms over the Chukchi Sea come from lower latitudes penetrating through the Bering Strait. As they approach the edge of the sea ice, a large sea ice opening forms on the western flank of the storm track near the sea ice edge (usually over the Russian side of the Chukchi Sea). On the eastern flank of the storm track,

northerly wind causes limited sea ice retreat due to the strong sea ice resist towards convergence (Chapter 3), while the divergence on the western flank tends to generate leads, open water, and ice fragments, which makes sea ice over this region become vulnerable to external forcing.

As shown by Figure 43, storms are associated with two strong wind bands during the SC. The first strong wind bands occur 1-2 days before the storm center arrived, while the second strong wind band can be found 1 day after the storm center arrived. Storms in the G_1^+ group gradually transport warm/moist air from lower latitudes, which results in a significant temperature increase compared with the climatological value. Both sensible and latent heat flux show significant increase as storm approaches. Clouds tend to reduce the net SW and enhance LW during the SC. Therefore, the sea ice rapidly decreases during the early SC. As storms further move northward into higher latitudes, strong and consistent cold air advection due to southerly wind is evidenced by the cold temperature anomaly gradually increasing from larger r^* to a smaller r^* as storms move away. The cold air advection refreezes the sea ice and further increases the sea ice area over the Chukchi Sea. Storms in the G_1^- group induce strong dry air advection at $t_{lag} = 0$ day, and the overall cloud impact on the surface energy budget is smaller compared with the G_1^+ group.

During the summer and early fall, storms in both G_2^+ and G_2^- groups tend to induce much weaker wind speeds. Storms in both G_1^- and G_2^- groups did not cause strong temperature advection, therefore, temperatures around the composite center stay nearly constant during the SC. On the other hand, a strong temperature advection but in an opposite sign can be found for storms in both G_1^+ and G_1^-.

A similar process occurs over other periphery seas, therefore, storms transport not just heat and moisture into the Arctic but serve as a mechanism to cause energy exchange between low and high

latitudes over periphery seas. During the energy exchange process, storms tend to cause statistically significant variations on the regional sea ice area.

What is the overall storm long-term impact on sea ice?

In the previous chapter, we categorized storms into G_1^+, G_1^-, G_2^+ and G_2^- groups based on their short-term impact on sea ice. In this section, we try to explore their long-term impact on the sea ice by estimating the temporal correlation over 1979-2018 between storm counts and the total sea ice area over seven regions. As shown by the previous section, storms passing the periphery seas often result in sea ice decrease during SC, while a rapid recovery to or even exceeds the climatology value under the Post-SC. Not surprisingly, the correlation coefficients over periphery seas are small, which suggest storms do not have a significant long-term impact on sea ice over those regions. Except for the Bering and Chukchi Seas, storm counts in all four groups tend to have a negative correlation with the total sea ice area, and no significant differences among different groups of storms. Both Bering and GIN seas have the smallest magnitude of the correlation coefficients between the total storm counts and the sea ice area. Over the Central Arctic, on the other hand, storms tend to cause sea ice area to fall below the climatology value for all four groups for at least two weeks after the storm passed. The storm counts have the largest correlation coefficients, which range from -0.69 to -0.79 with the total sea ice area over the entire Central Arctic for $r^* \leq 200$ km (Table 11 to Table 14), and the correlation decreases with increasing r^*. Through this comparison, we found short-term storm impacts on sea ice may not be a good indicator of the long-term storm impact on sea ice especially over periphery seas.

Do storms coming from continents or the ocean impact sea ice differently?

As an example, we focus on storms passing through the East Siberian and Laptev Seas and define the average continental life time fraction (F_{cont}) as the time fraction between the total time storms spent over the Eurasia continents before they move over the sea ice surface and the entire time period before they move over the sea ice surface at various r^*. If storms spend most of their time over the continental area ($F_{cont} > 0.6$), we categorize those storms into the continental storm group, otherwise into the ocean storm group ($F_{cont} < 0.4$).

During 1979-1988, the significant sea ice increase under the post-SC for storms in the G_1^+ group (Figure 30) is primarily due to storms moving from the ocean surface (Figure 44). Continental storms in this group lead to a larger sea ice decrease during the SC, but much less impact during the Post-SC. During 1989-1998, storms from both the continental and ocean surface result in a larger sea ice decrease during the SC, but slightly recovered or exceed the climatological value one week after storms moved away. A weaker but longer range and longer time period storm impact on sea ice can be found during 1999-2008 compared with 1989-1998, and storms had much less impact on sea ice during 2009-2018. Overall, there is no significantly different patterns compared with storms coming from the continent and ocean surface over the East Siberian and Laptev Seas.

If we extend our calculation of F_{cont} to span over the entire storm lifetime period, results show storms spent most of their time over the ocean (Table 7 to Table 10) in all four groups. Longer time over the ocean/sea ice surface (smaller magnitude of F_{cont}) does not suggest a larger magnitude of the sea ice difference between the SC/Post-SC and CC/Post-CC, but they do correspond to a longer and more consistent storm impact on sea ice causing sea ice to be either

larger or smaller than the CC/Post-CC. The sea ice difference between SC/Post-SC and CC/Post-CC also covers a larger range of r^*.

4.8 Conclusions

In this study, we have investigated the storm impact on sea ice area over seven regions spanning from 1979 to 2018 by using a new composite analysis concerning local sea ice changes before, during, and after the storm. We split these 40 years into four fixed 10-year windows (1979-1988, 1989-1998, 1999-2008, and 2009-2018) and compared sea ice area in SC and Post-SC with CC and Post-CC. Additionally, we categorize storms into four groups according to the Pre-SC sea ice area changing rate naming G_1^+, G_1^-, G_2^+, and G_2^-.

In summary, the major findings are:

1. The storm impact on sea ice varies depends on locations, time of the year, and the local sea ice conditions. Autumn storms tends to have a larger short-term and mid-term impacts on sea ice area over most regions compared with summer storms.
2. Over periphery seas, storms tend to cause less area compared with the climatological values during the SC. Such changes in sea ice area usually starts from two days before and ends two days after the storm passed. Within one or two week(s) after the storms passed, the sea ice area tends to recover or exceed the climatological values. Storms have a stronger short-term and mid-term impact on sea ice area over the western Arctic (Chukchi, E. Siberian and Laptev Seas) than eastern Arctic (Barents and Kara Seas).
3. Over the Central Arctic, storms tend to cause sea ice smaller than the climatology condition, and such storm induced sea ice changes tends to continue for at least one or two

weeks after storms moved away. Only over the Central Arctic are storm counts highly correlated ($r>0.75$) with the sea ice area.

4. Storms over both the Pacific and Atlantic entrances have less impact on sea ice area compared with the periphery seas. Storms over the Bering Sea have a larger impact on sea ice area than GIN Seas.

4.9 Figures

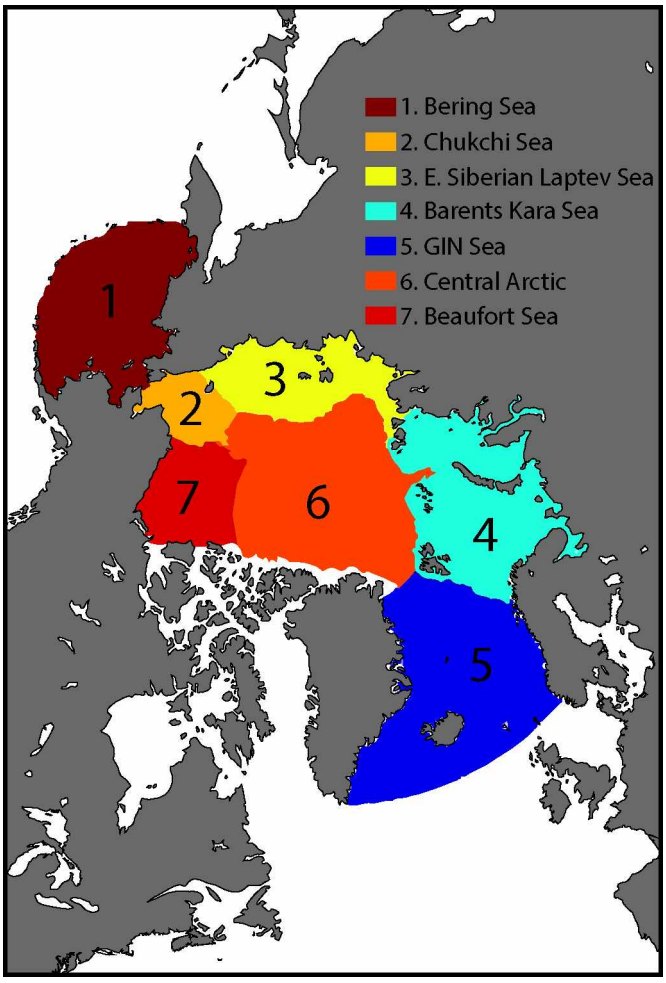

Figure 15. The regional Arctic Ocean mask. It includes Bering Sea, Chukchi Sea, East Siberian (E. Siberian) and Laptev Sea, Barents and Kara Seas, Greenland, Iceland, and Norwegian (GIN) Sea, Central Arctic Ocean, and Beaufort Sea.

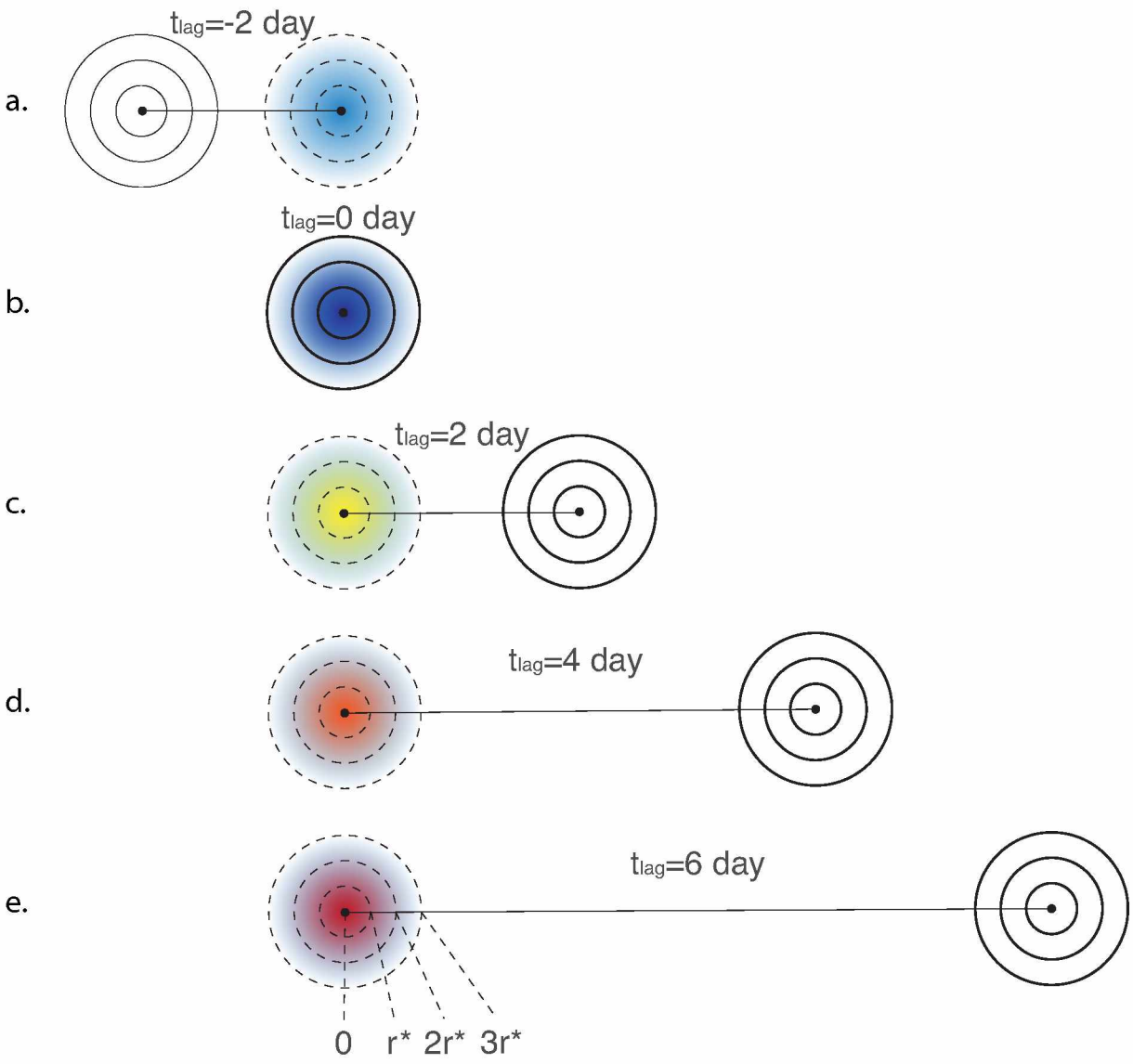

Figure 16. Schematic diagram showing the storm composite analysis. The SC is defined starting from (a) $\boldsymbol{t_{lag} = -2}$ days to (b) $\boldsymbol{t_{lag} = 2}$ days. The post-SC starts from (c) $\boldsymbol{t_{lag} = 2}$ days, and also shown (d) $\boldsymbol{t_{lag} = 4}$ days, (e) $\boldsymbol{t_{lag} = 6}$ days.

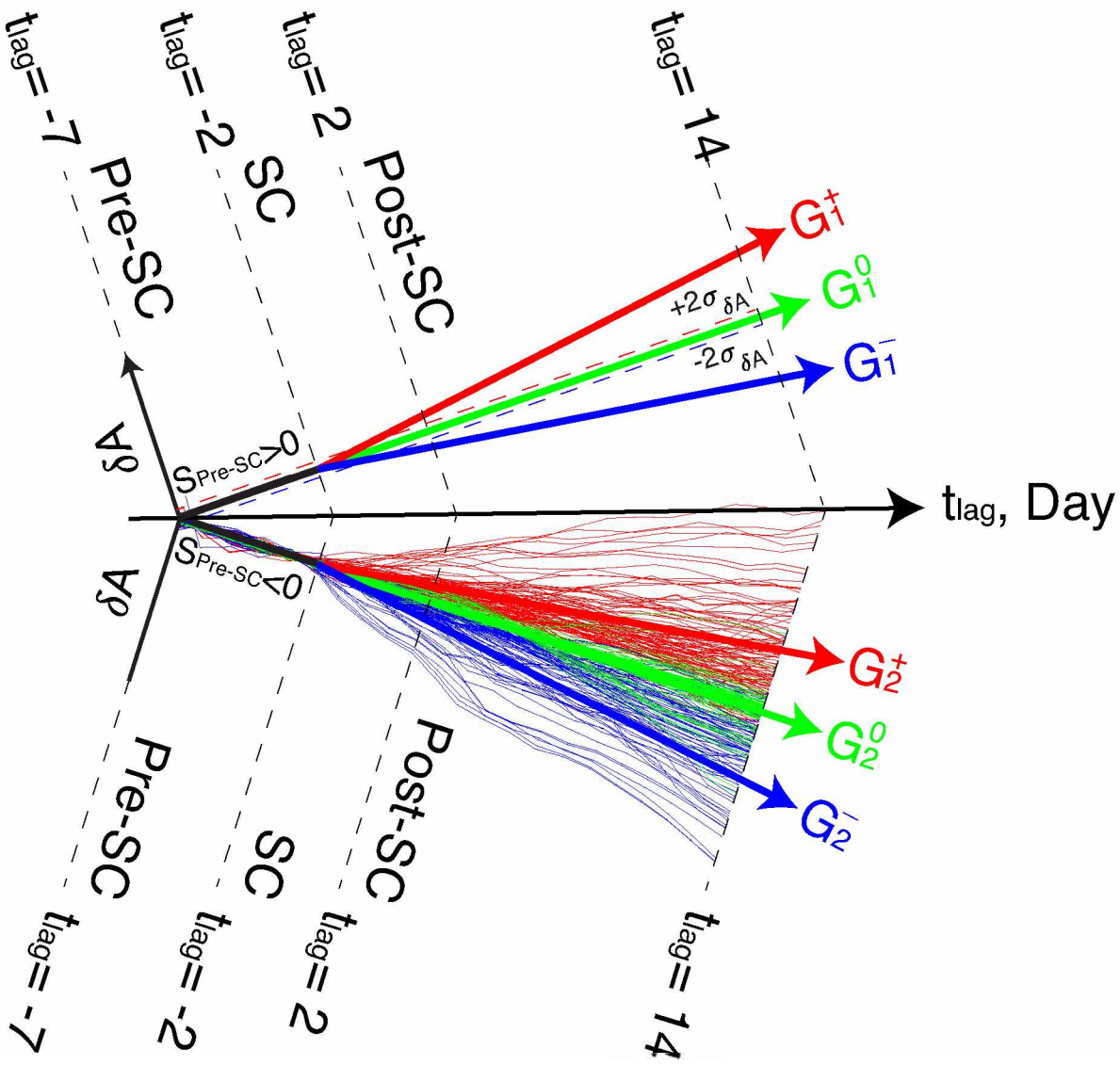

Figure 17. An example shows the difference between the fitted and observed sea ice area ($\boldsymbol{\delta A}$). Red lines represent storms categorized into $\boldsymbol{G_1^+}$ ($\boldsymbol{G_2^+}$), green lines represent storms categorized into $\boldsymbol{G_1^0}$ ($\boldsymbol{G_2^0}$), and blue lines represents storms categorized into $\boldsymbol{G_1^-}$ ($\boldsymbol{G_2^-}$) groups. Thin lines under $\boldsymbol{S_{Pre-SC} < 0}$ condition is a real case example shown how $\boldsymbol{\delta A}$ changes as a function of $\boldsymbol{t_{lag}}$.

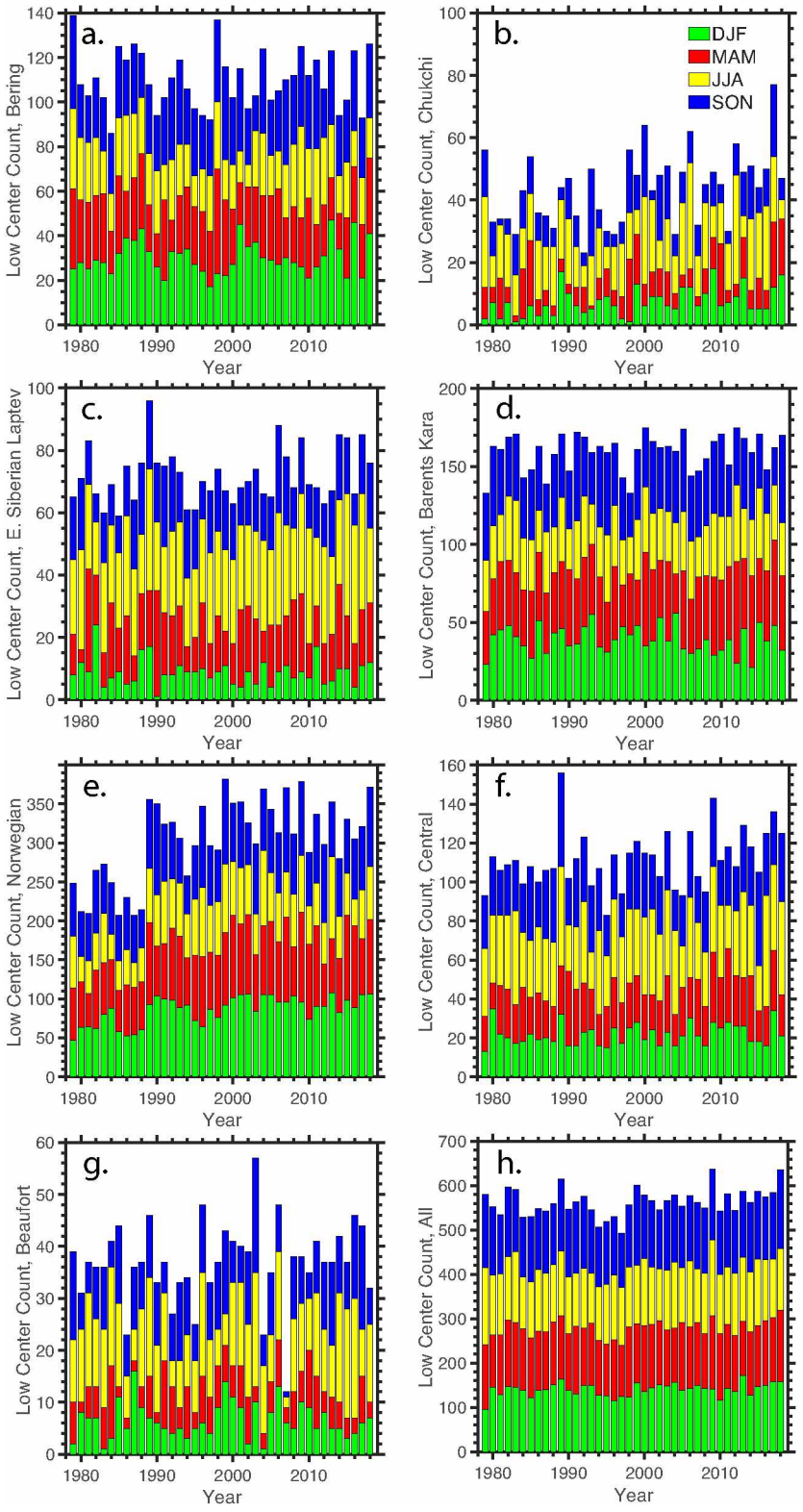

Figure 18. Stacked bar plot summarizing the storm track counts over (a) Bering Sea, (b) Chukchi Sea, (c) East Siberian and Laptev Sea, (d) Barents and Kara Seas, (e) Greenland,

Figure 18 (continued) Iceland, and Norwegian Sea, (f) Central Arctic Ocean, (g) Beaufort Sea, and (h) the total counts. Green, red, yellow, and blue represent the number of storms occurred in winter (December, January, and February), spring (March, April, and May), summer (June, July, and August), and autumn (September, October, and November) every year respectively.

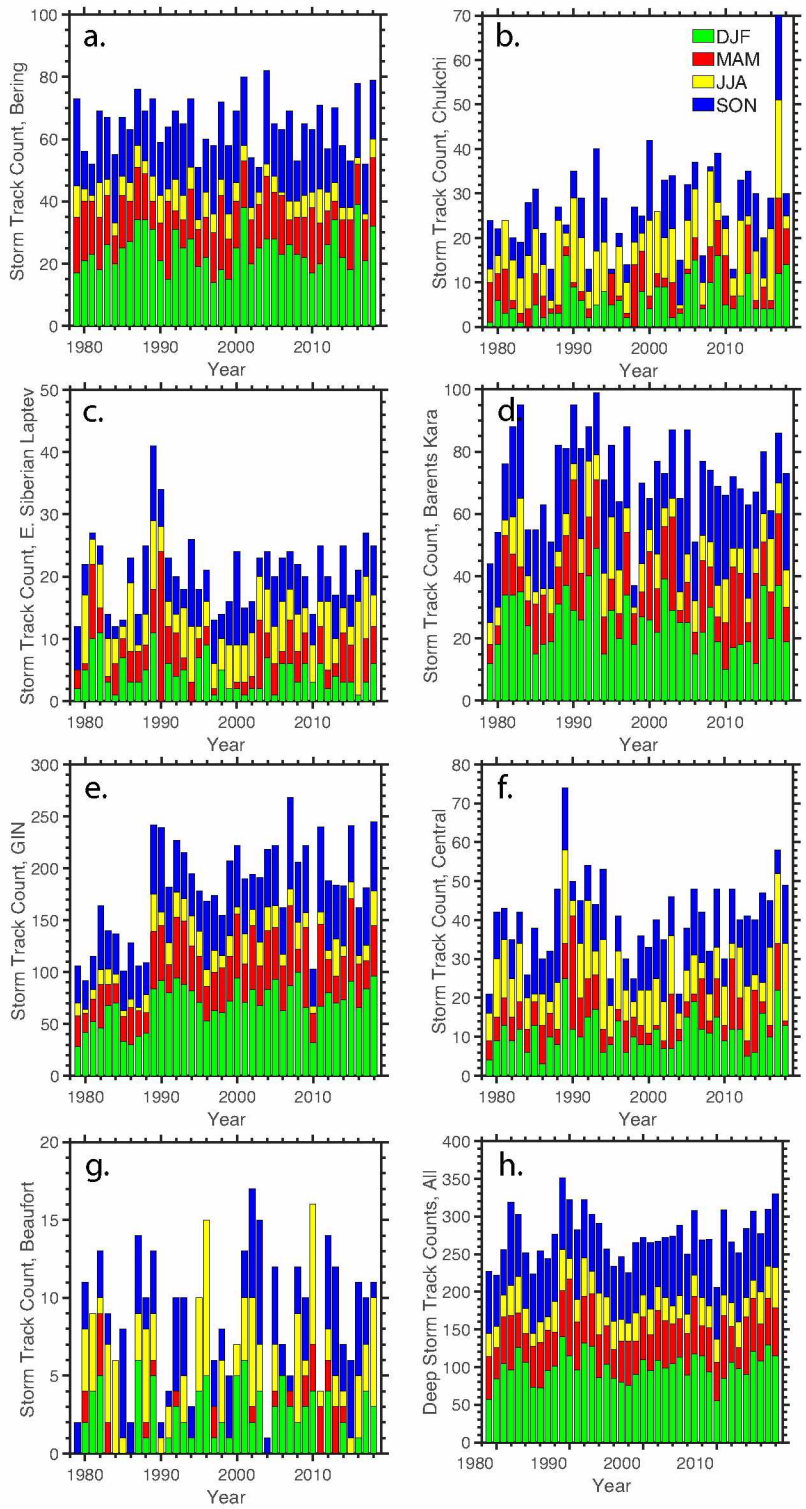

Figure 19. Same as Fig. 18 but for deep storms counts over (a) Bering Sea, (b) Chukchi Sea, (c) East Siberian and Laptev Sea, (d) Barents and Kara Seas, (e) Greenland, Iceland, and Norwegian Sea, (f) Central Arctic Ocean, (g) Beaufort Sea, and (h) the total counts.

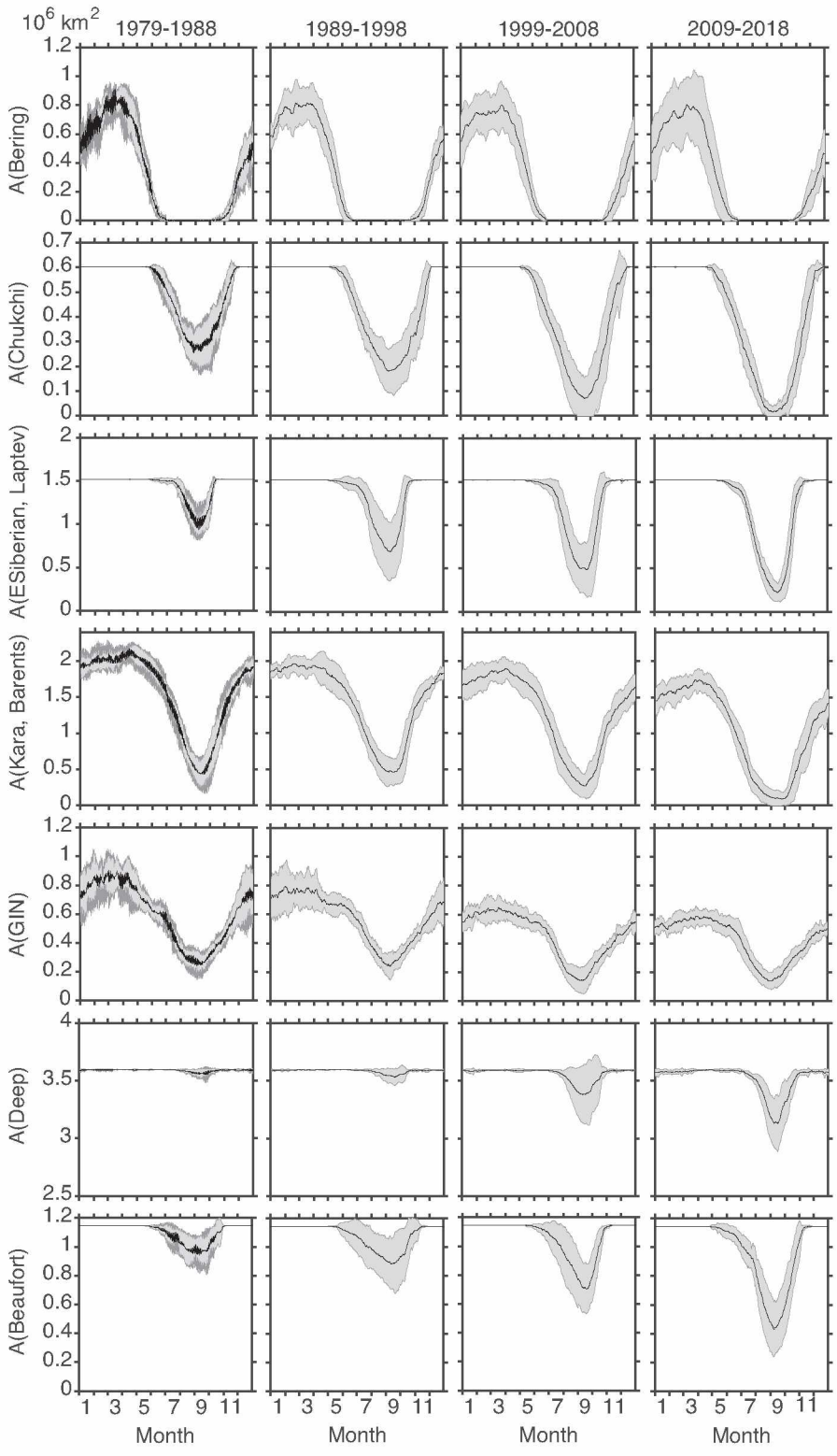

Figure 20. Daily averaged sea ice area for seven regions shown in Figure 15 in successive 10-yr periods from 1979 to 2018.

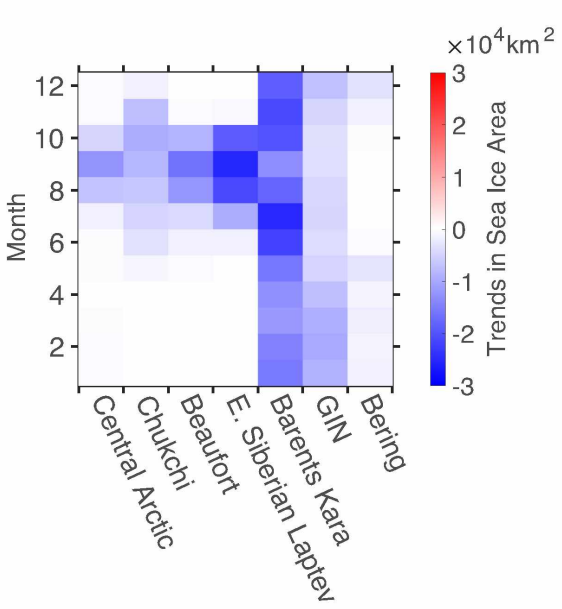

Figure 21. Monthly sea ice area trends (1979-2018) for seven regions shown in Figure 15.

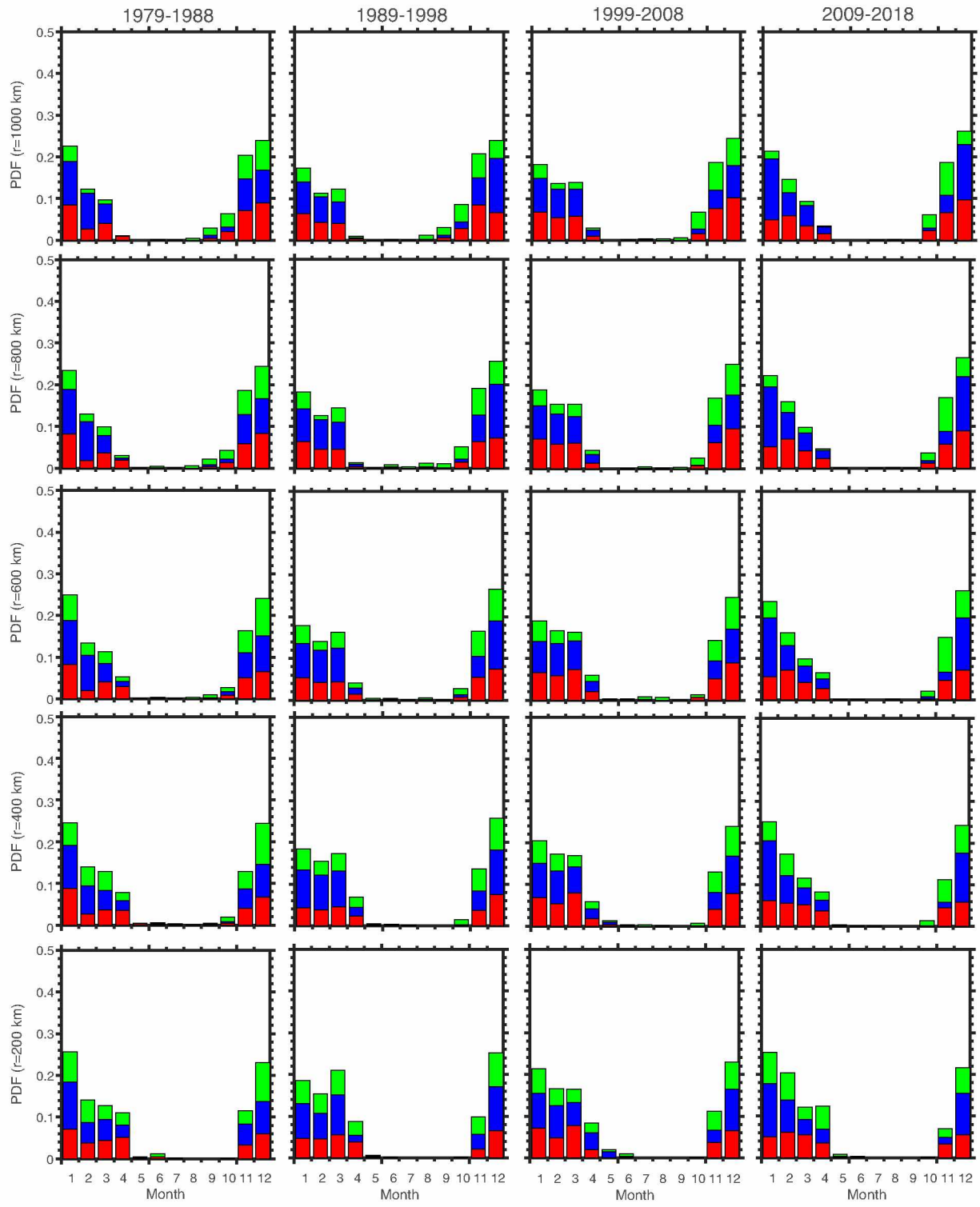

Figure 22. Stacked bar charts shown the propability distribution function (PDF) of storm counts over the Bering Sea. Blue, green, and red sectors represent storms from $\boldsymbol{G_1^-}$, $\boldsymbol{G_1^0}$, and $\boldsymbol{G_1^+}$ respectively.

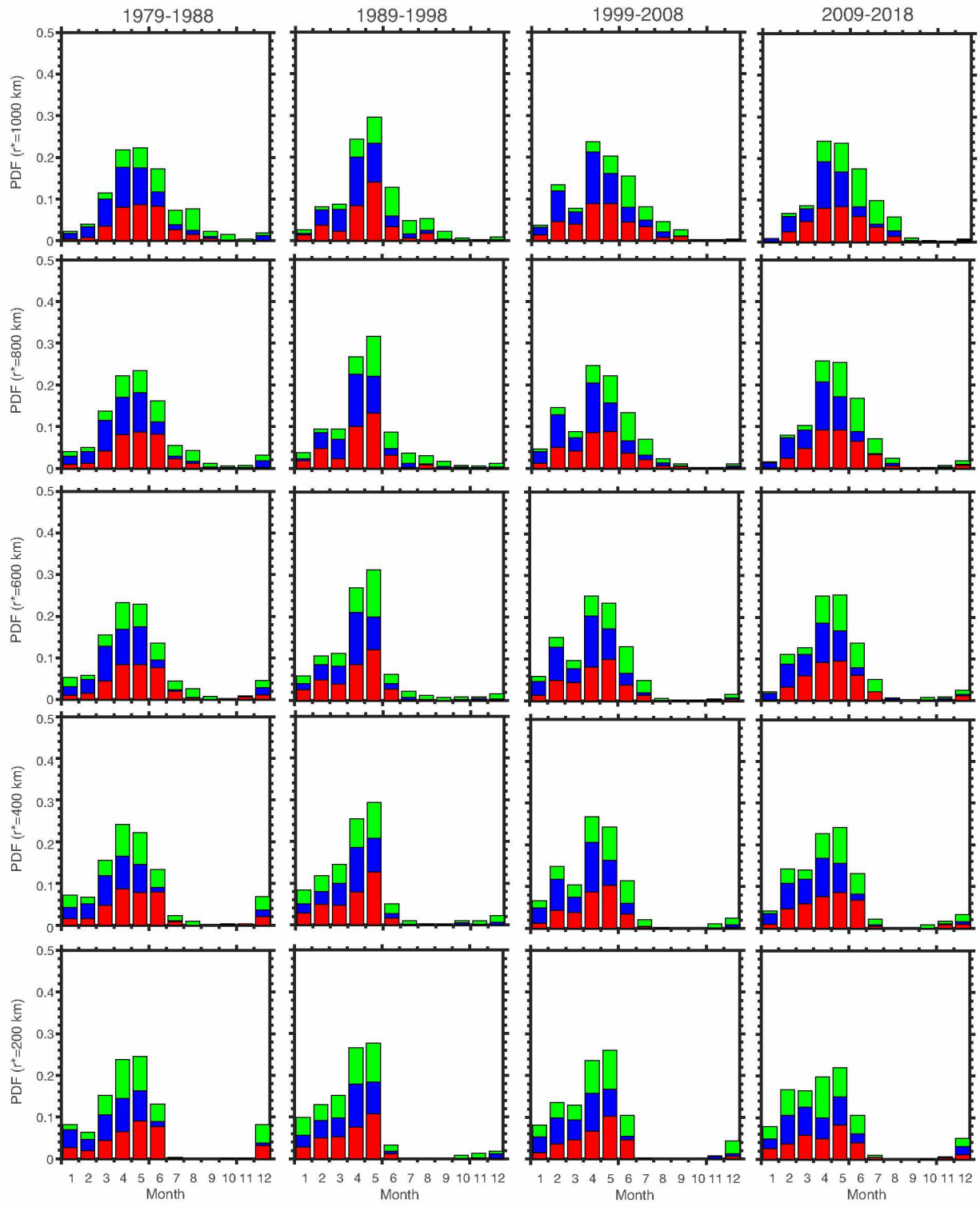

Figure 23. Stacked bar charts shown the propability distribution function (PDF) of the storm counts over the Bering Sea. Blue, green, and red sectors represent storms categorized into $\boldsymbol{G_2^-}$, $\boldsymbol{G_2^0}$, and $\boldsymbol{G_2^+}$ groups respectively.

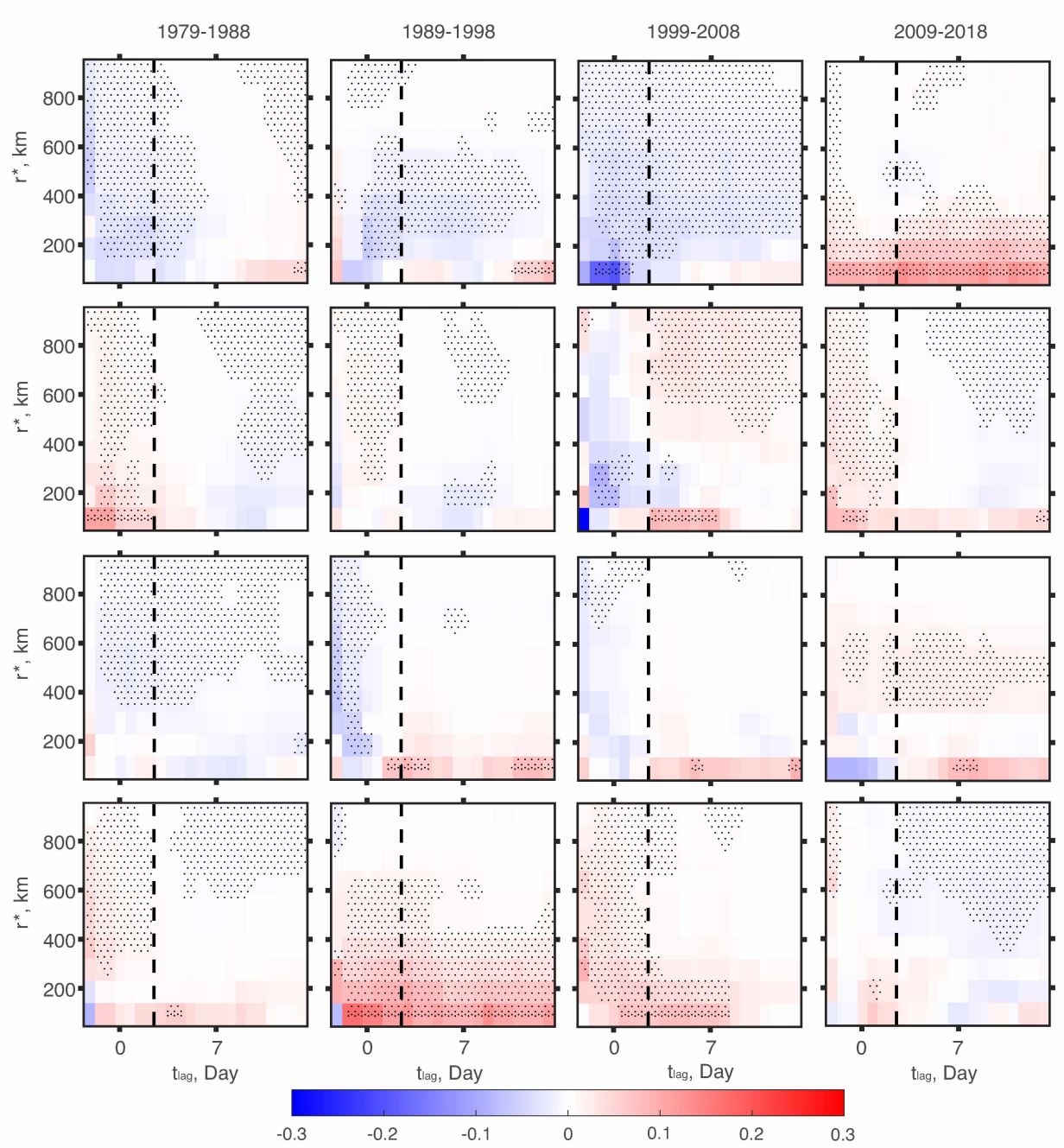

Figure 24. The ratio between sea ice area difference between SC/Post-SC and CC/Post-CC and the total area with radius $\boldsymbol{r^*}$ for $\boldsymbol{G_1^+}$ (top), $\boldsymbol{G_1^-}$, $\boldsymbol{G_2^+}$, and $\boldsymbol{G_2^-}$ (bottom) span from 1979-1988 (left), 1989-1998, 1999-2008, and 2009-2018 (right) over the Bering Sea. The thick black dashed line represents $\boldsymbol{t_{lag} = -2}$ days.

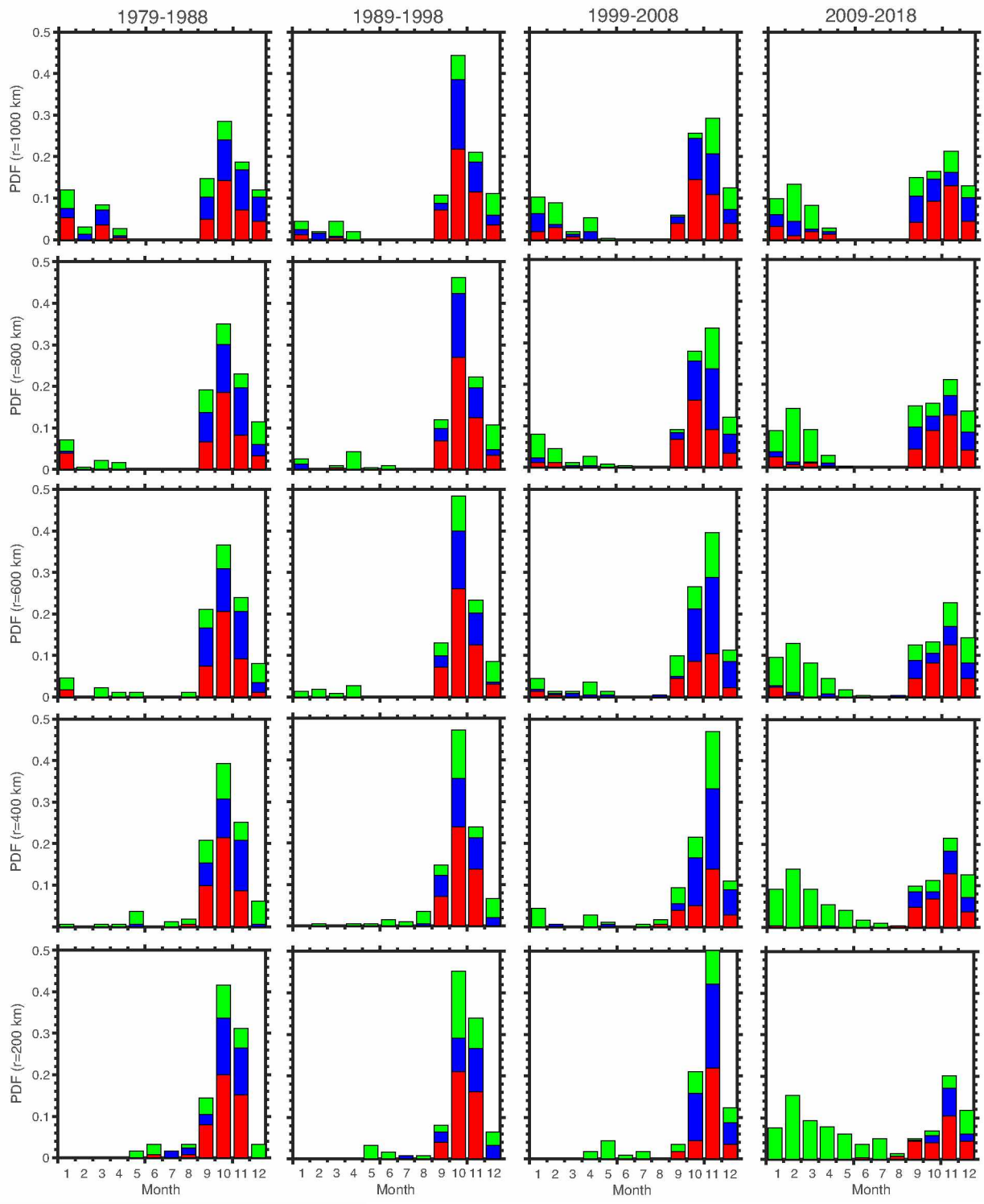

Figure 25. Stacked bar charts shown the propability distribution function (PDF) of storm counts over the Chukchi Sea. Blue, green, and red sectors represent storms from $\boldsymbol{G_1^-}$, $\boldsymbol{G_1^0}$, and $\boldsymbol{G_1^+}$ respectively.

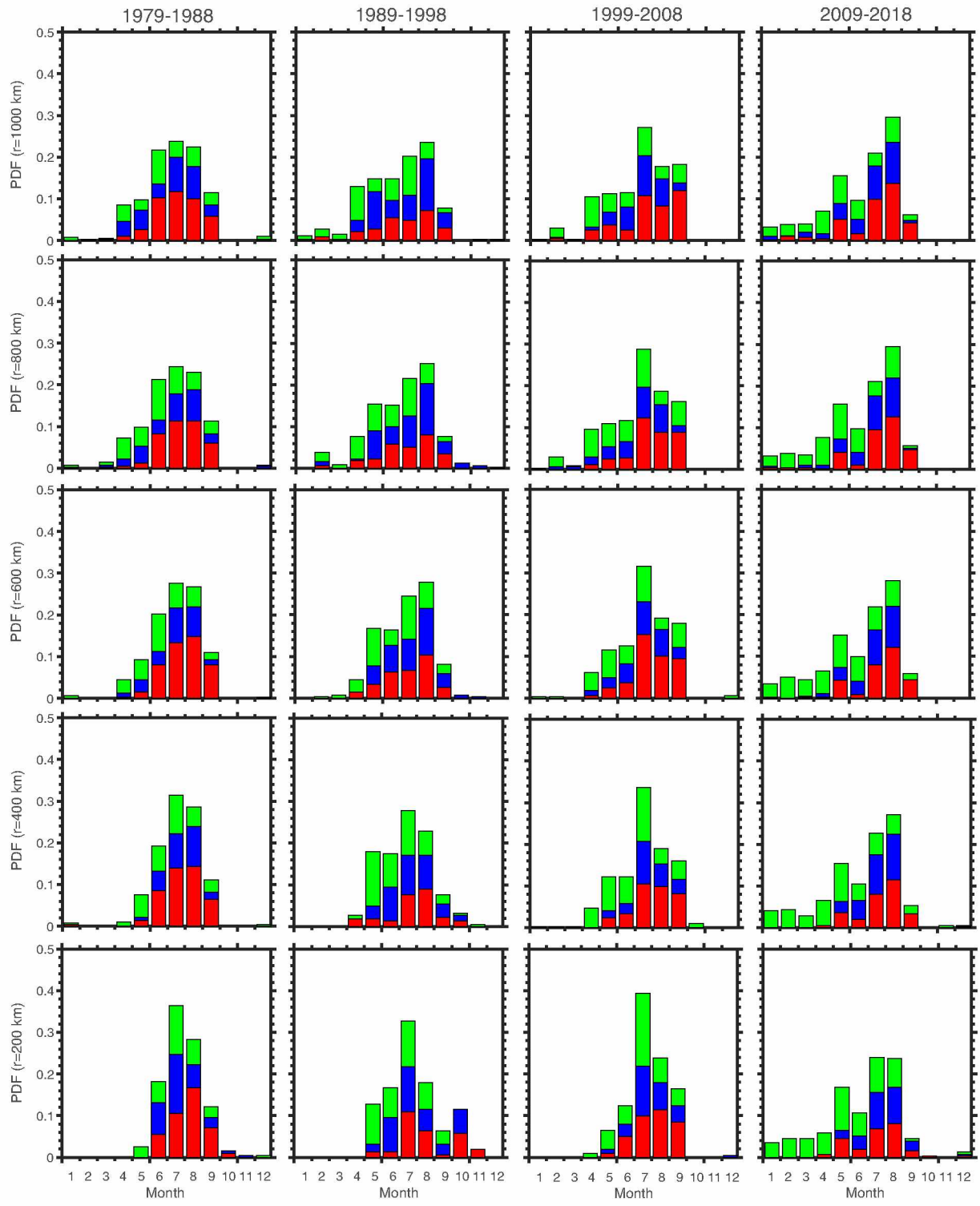

Figure 26. Stacked bar charts shown the propability distribution function (PDF) of the storm counts over the Chukchi Sea. Blue, green, and red sectors represent storms categorized into $\boldsymbol{G_2^-}$, $\boldsymbol{G_2^0}$, and $\boldsymbol{G_2^+}$ groups respectively.

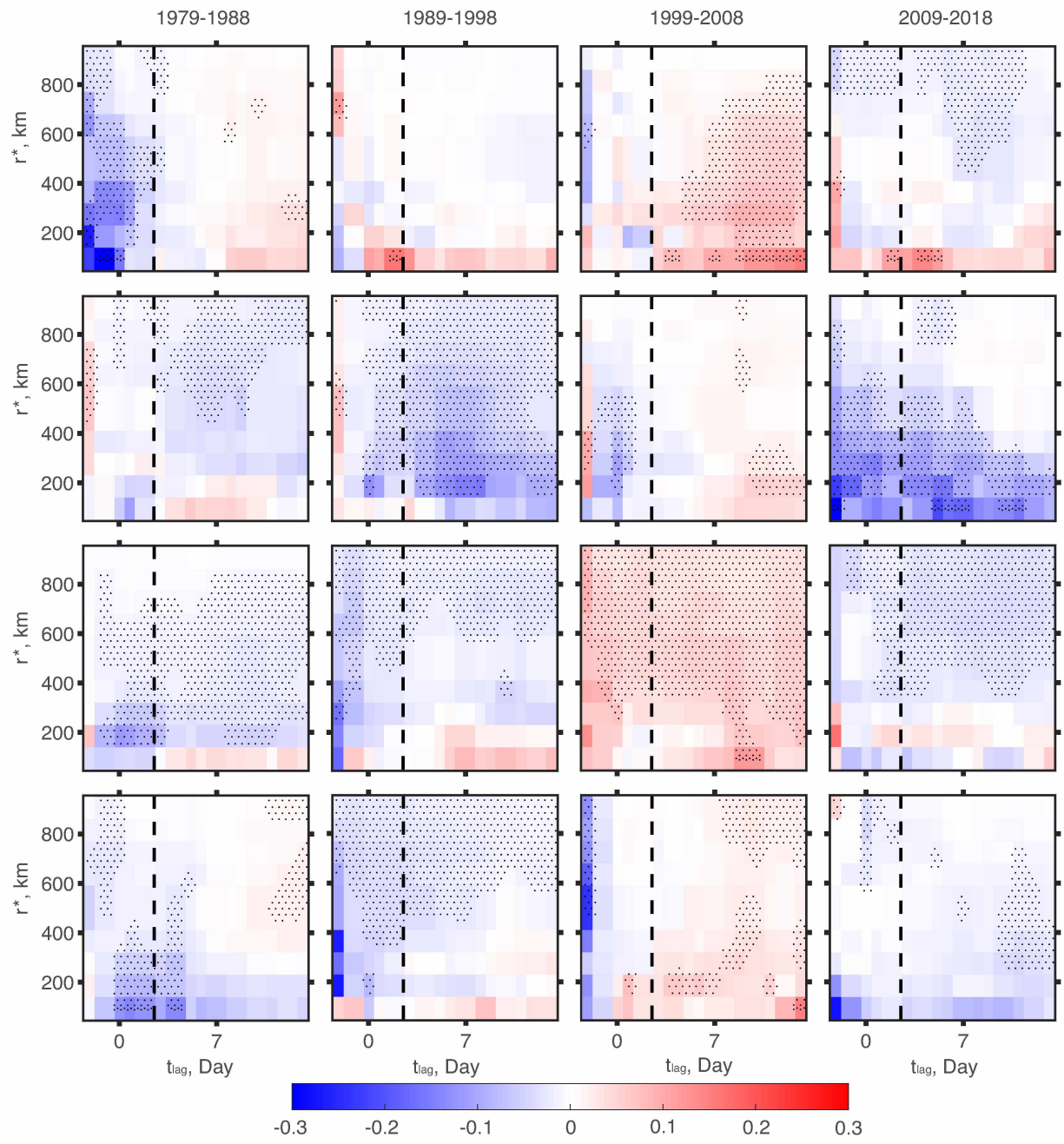

Figure 27. The ratio between sea ice area difference between SC/Post-SC and CC/Post-CC and the total area with radius $\boldsymbol{r^*}$ for $\boldsymbol{G_1^+}$ (top), $\boldsymbol{G_1^-}$, $\boldsymbol{G_2^+}$, and $\boldsymbol{G_2^-}$ (bottom) span from 1979-1988 (left), 1989-1998, 1999-2008, and 2009-2018 (right) over the Chukchi Sea. The thick black dashed line represents $\boldsymbol{t_{lag} = -2}$ days.

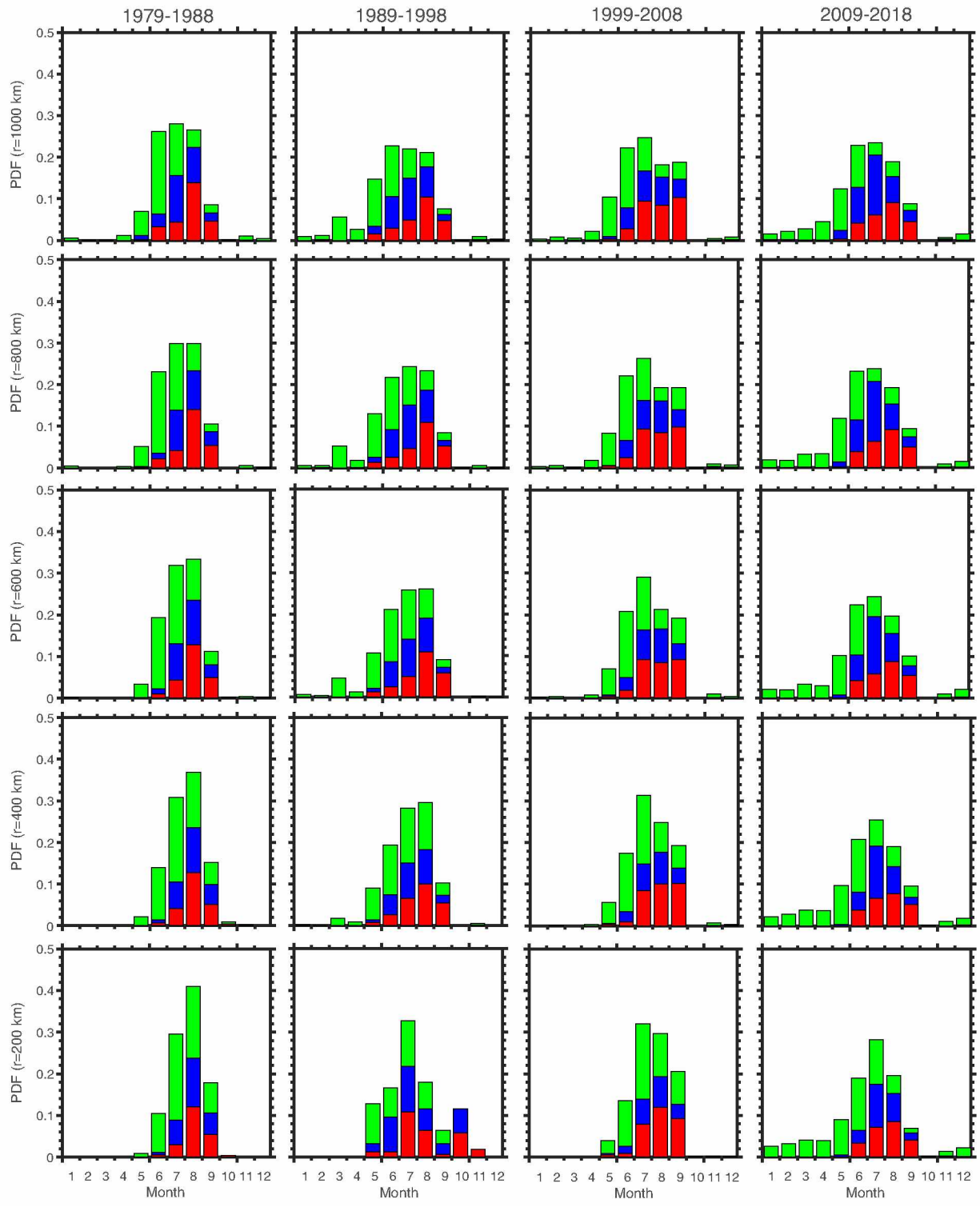

Figure 28. Stacked bar charts shown the propability distribution function (PDF) of storm counts over the East Siberian and Laptev Seas. Blue, green, and red sectors represent storms from $\boldsymbol{G_1^-}$, $\boldsymbol{G_1^0}$, and $\boldsymbol{G_1^+}$ respectively.

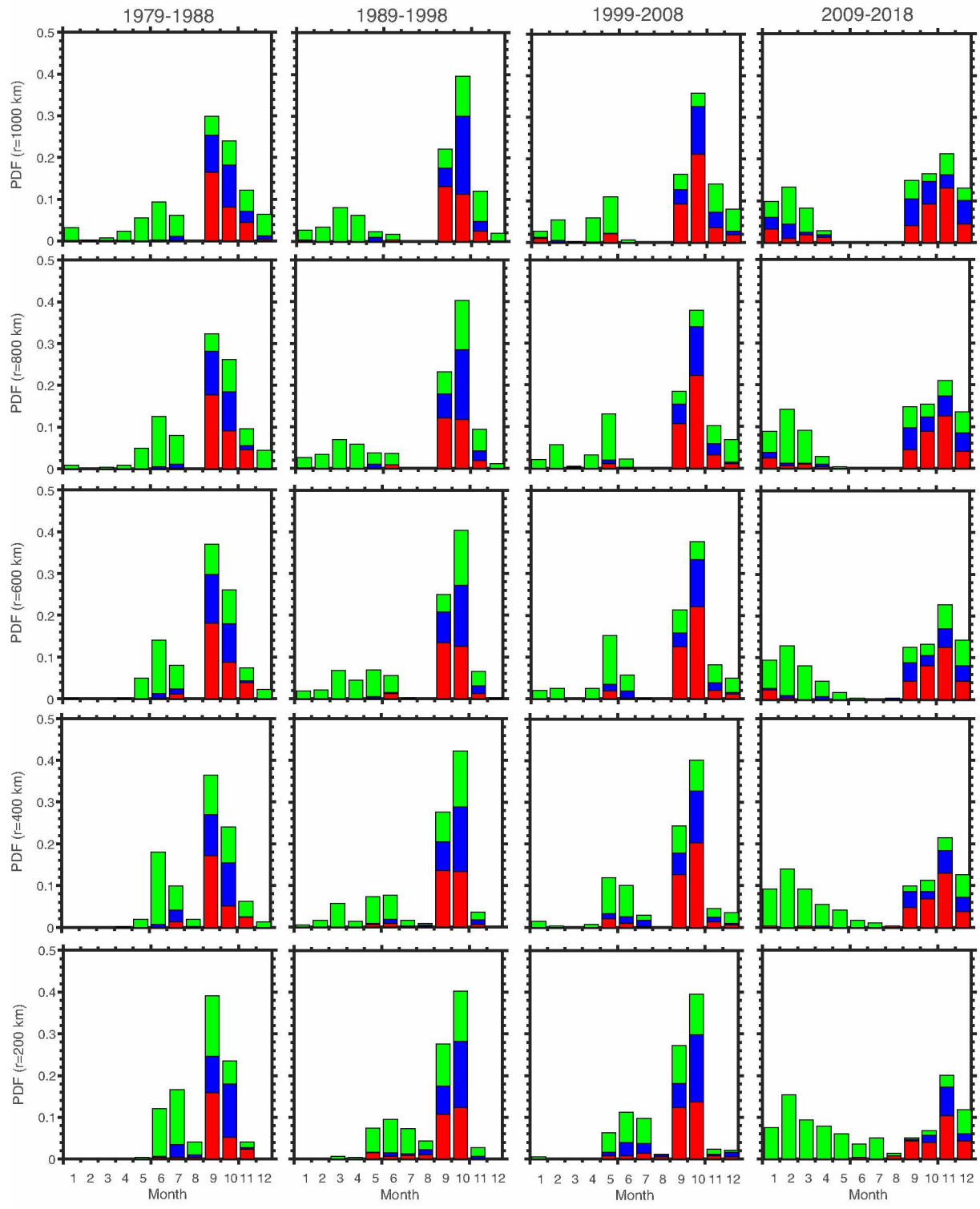

Figure 29. Stacked bar charts shown the propability distribution function (PDF) of the storm counts over the East Siberian and Laptev Seas. Blue, green, and red sectors represent storms categorized into $\boldsymbol{G_2^-}$, $\boldsymbol{G_2^0}$, and $\boldsymbol{G_2^+}$ groups respectively.

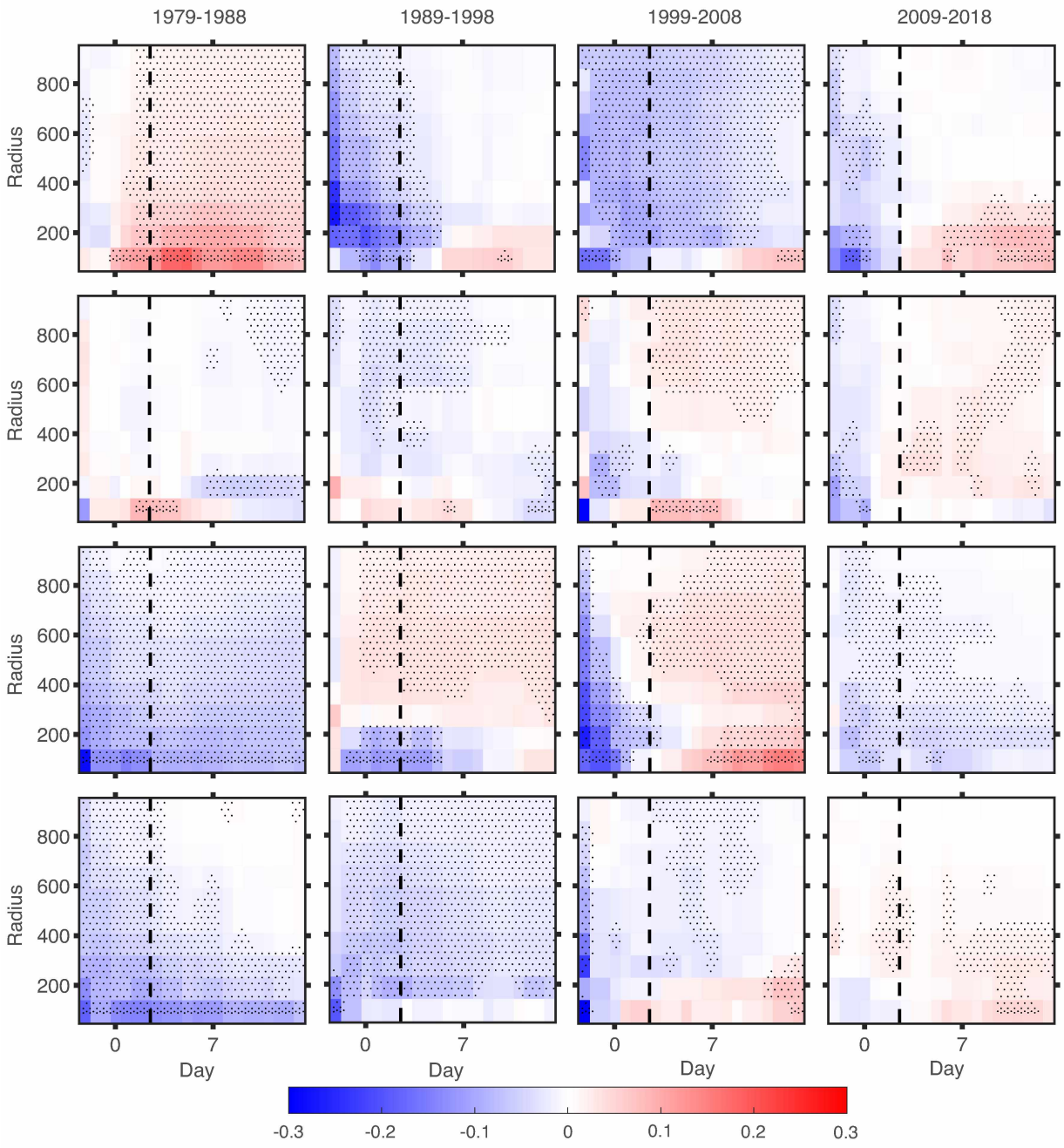

Figure 30. The ratio between sea ice area difference between SC/Post-SC and CC/Post-CC and the total area with radius r^* for G_1^+ (top), G_1^-, G_2^+, and G_2^- (bottom) span from 1979-1988 (left), 1989-1998, 1999-2008, and 2009-2018 (right) over the East Siberian and Laptev Seas. The thick black dashed line represents $t_{lag} = -2$ days.

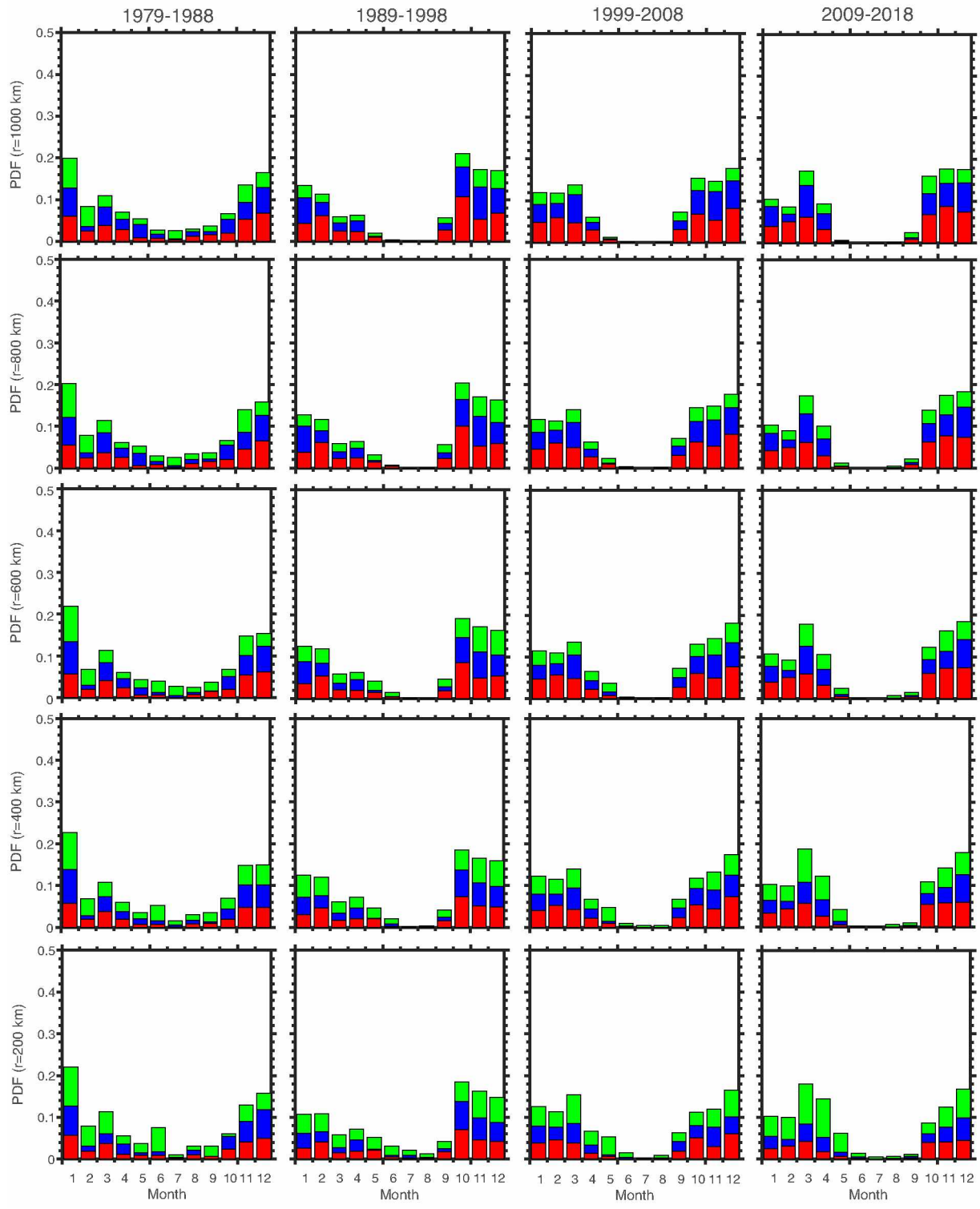

Figure 31. Stacked bar charts shown the propability distribution function (PDF) of storm counts over the Barents and Kara Seas. Blue, green, and red sectors represent storms from $\boldsymbol{G_1^-}$, $\boldsymbol{G_1^0}$, and $\boldsymbol{G_1^+}$ respectively.

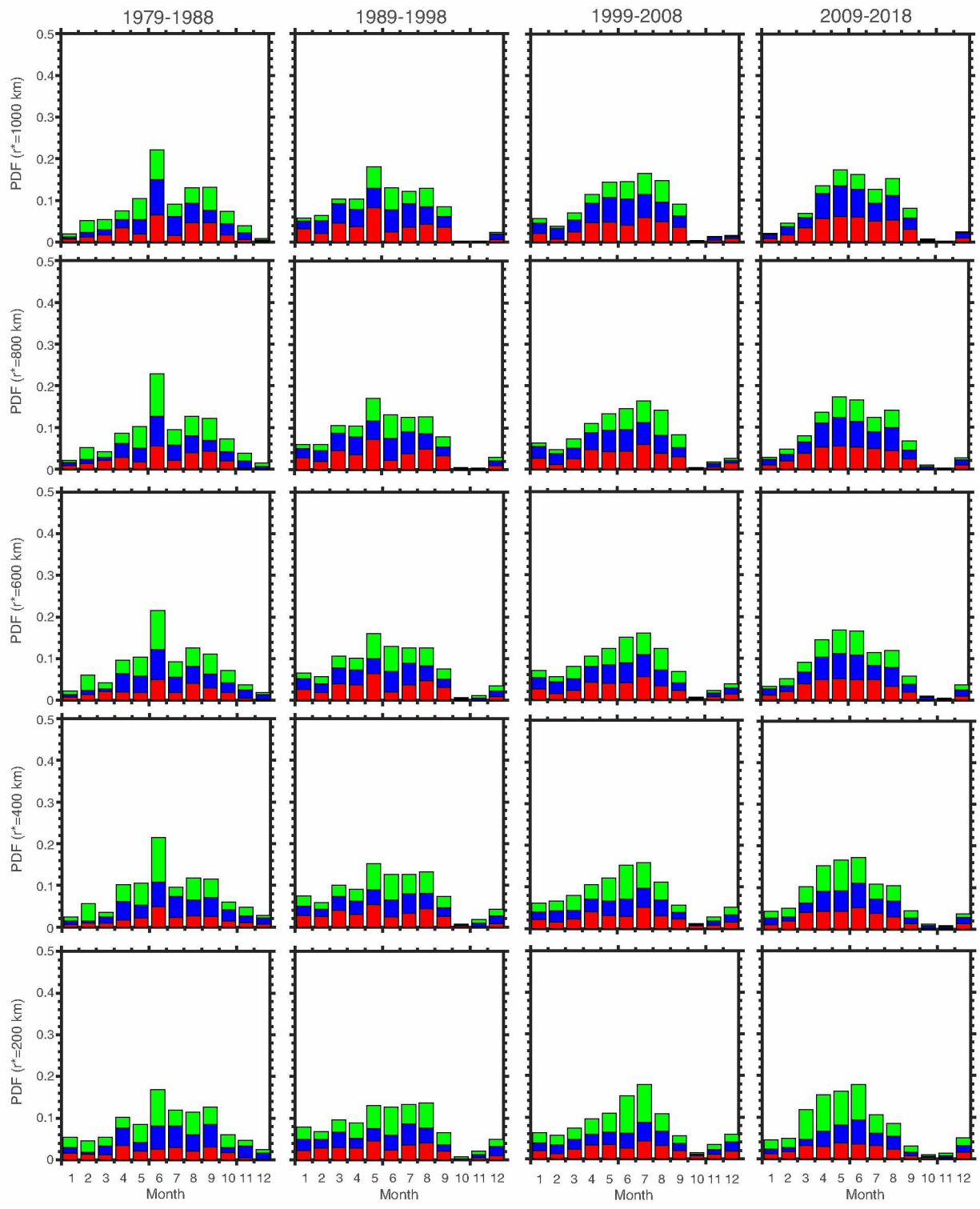

Figure 32. Stacked bar charts shown the propability distribution function (PDF) of the storm counts over the Barents and Kara Seas. Blue, green, and red sectors represent storms categorized into $\boldsymbol{G_2^-}$, $\boldsymbol{G_2^0}$, and $\boldsymbol{G_2^+}$ groups respectively.

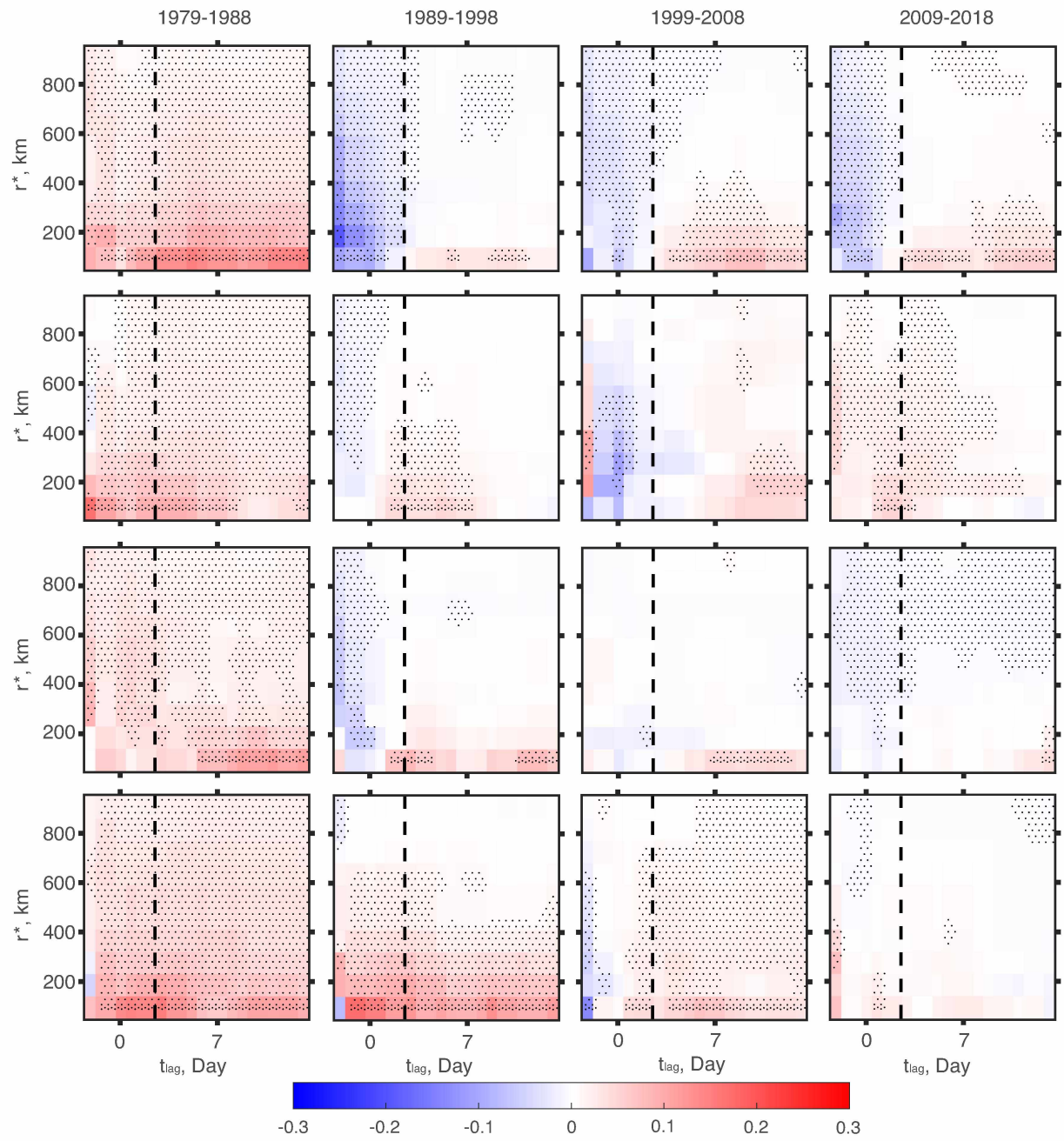

Figure 33. The ratio between sea ice area difference between SC/Post-SC and CC/Post-CC and the total area with radius $\boldsymbol{r^*}$ for $\boldsymbol{G_1^+}$ (top), $\boldsymbol{G_1^-}$, $\boldsymbol{G_2^+}$, and $\boldsymbol{G_2^-}$ (bottom) span from 1979-1988 (left), 1989-1998, 1999-2008, and 2009-2018 (right) over the Barents and Kara Seas. The thick black dashed line represents $\boldsymbol{t_{lag} = -2}$ days.

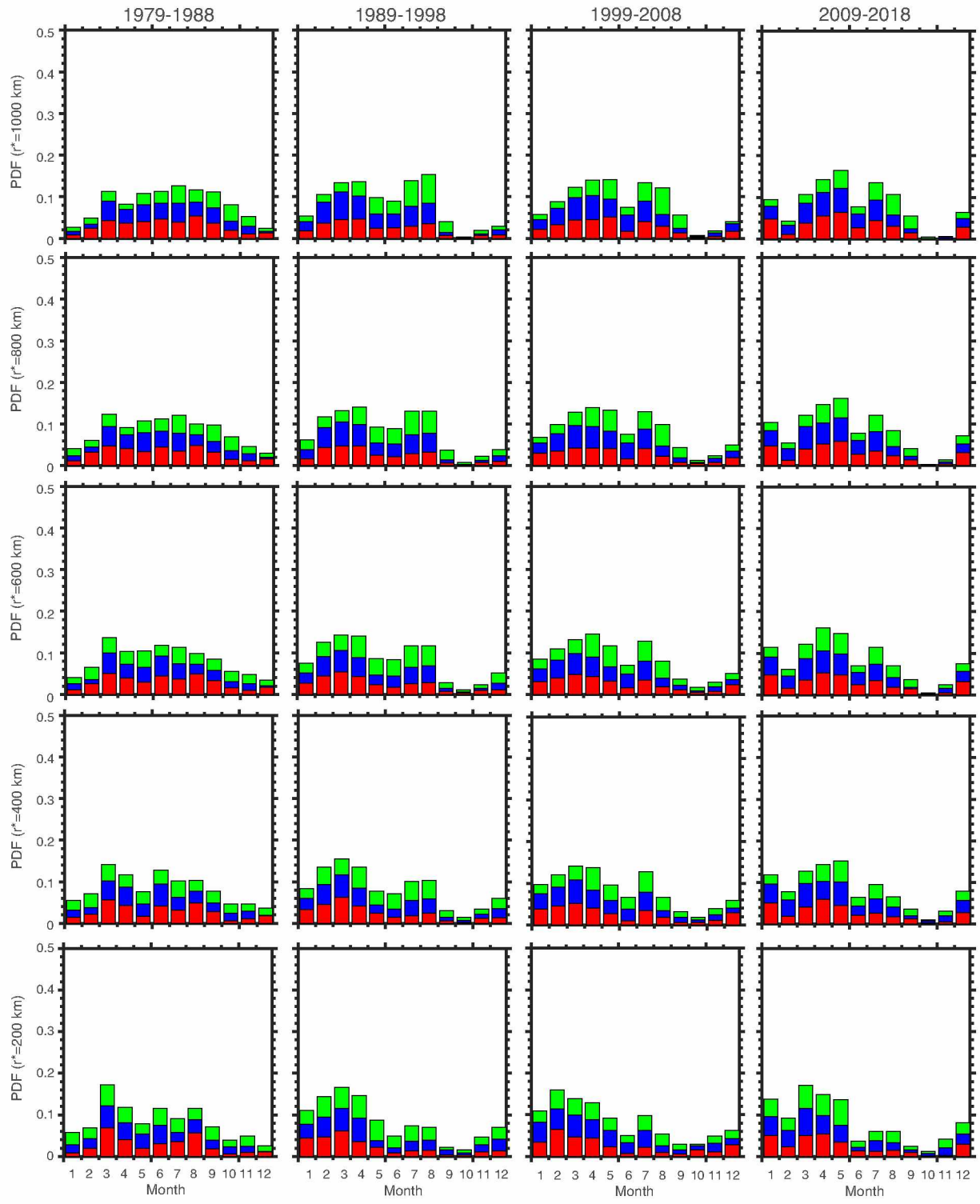

Figure 34. Stacked bar charts shown the propability distribution function (PDF) of storm counts over the GIN Seas. Blue, green, and red sectors represent storms from $\boldsymbol{G_1^-}$, $\boldsymbol{G_1^0}$, and $\boldsymbol{G_1^+}$ respectively.

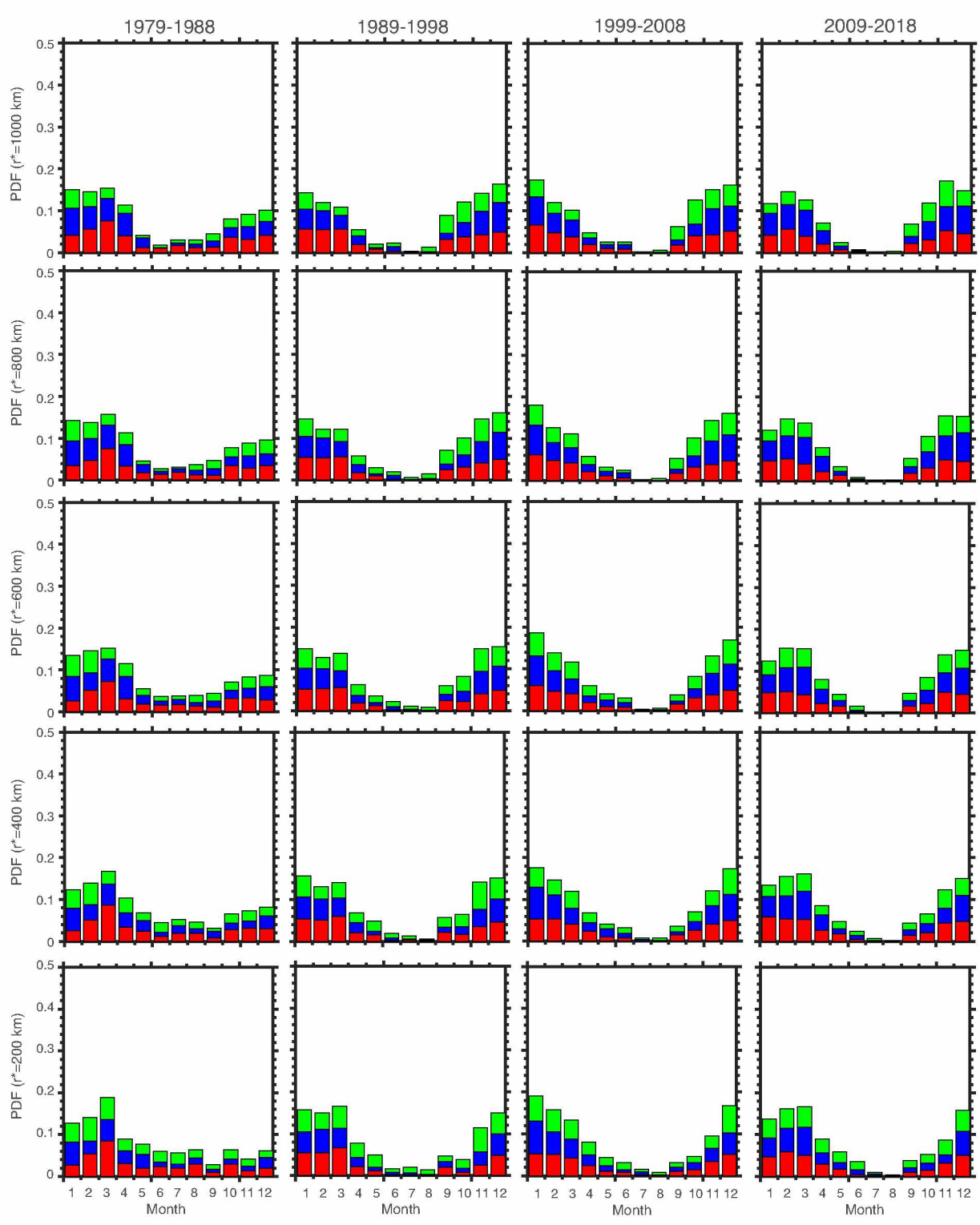

Figure 35. Stacked bar charts shown the propability distribution function (PDF) of the storm counts over the GIN Seas. Blue, green, and red sectors represent storms categorized into $\boldsymbol{G_2^-}$, $\boldsymbol{G_2^0}$, and $\boldsymbol{G_2^+}$ groups respectively.

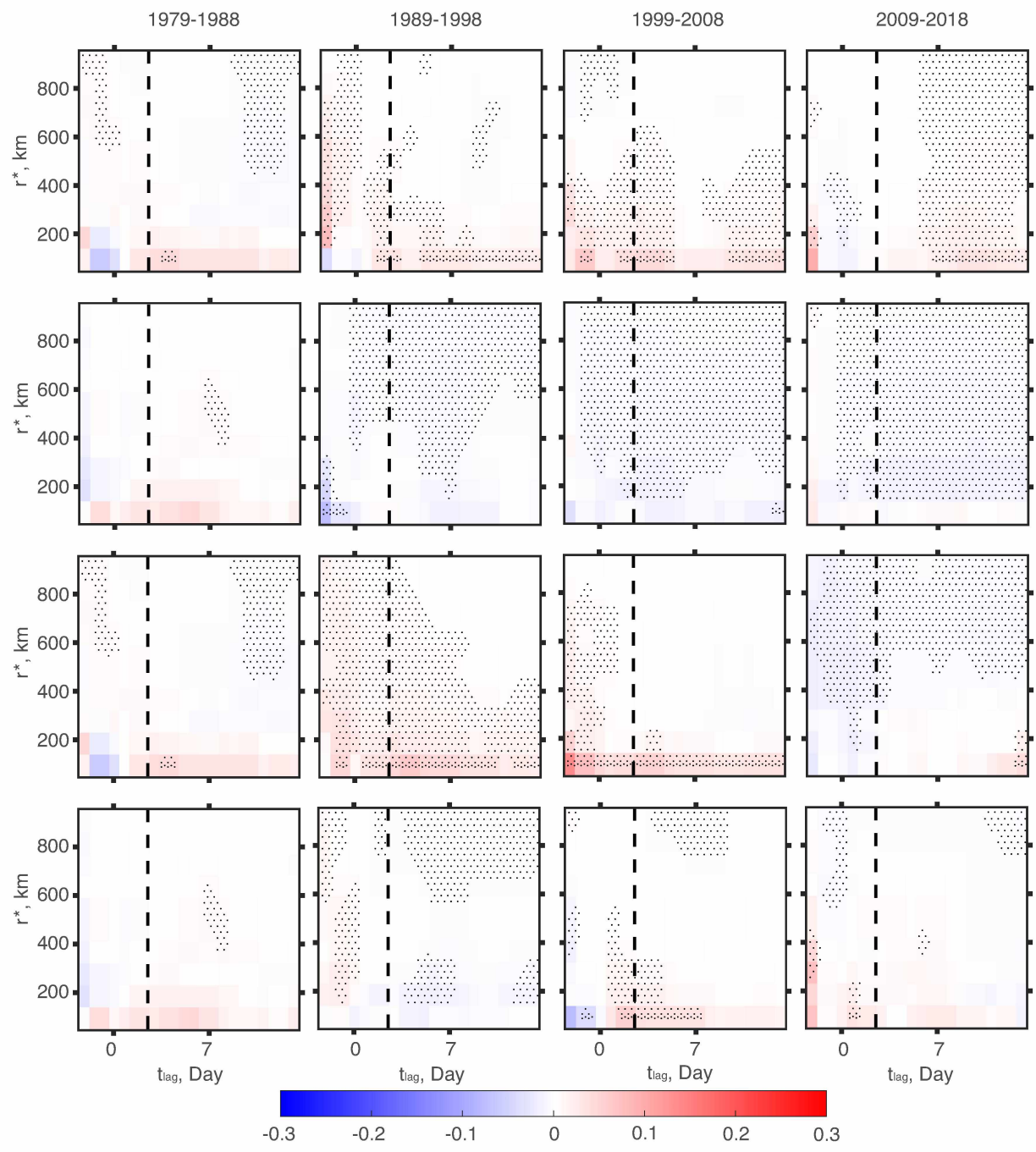

Figure 36. The ratio between sea ice area difference between SC/Post-SC and CC/Post-CC and the total area with radius $\boldsymbol{r^*}$ for $\boldsymbol{G_1^+}$ (top), $\boldsymbol{G_1^-}$, $\boldsymbol{G_2^+}$, and $\boldsymbol{G_2^-}$ (bottom) span from 1979-1988 (left), 1989-1998, 1999-2008, and 2009-2018 (right) over the GIN Seas. The thick black dashed line represents $\boldsymbol{t_{lag} = -2}$ days.

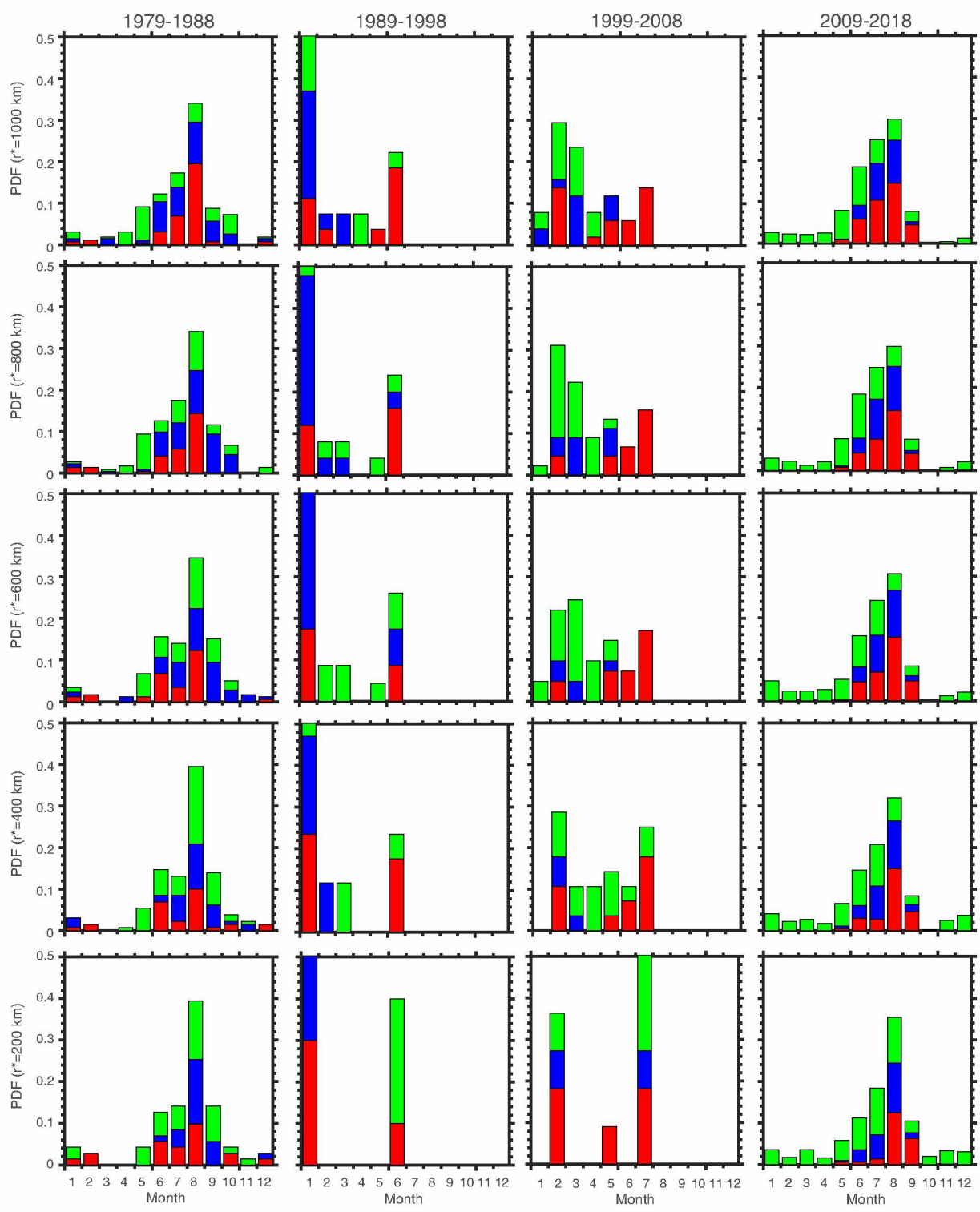

Figure 37. Stacked bar charts shown the propability distribution function (PDF) of storm counts over the Beaufort Sea. Blue, green, and red sectors represent storms from $\boldsymbol{G_1^-}$, $\boldsymbol{G_1^0}$, and $\boldsymbol{G_1^+}$ respectively.

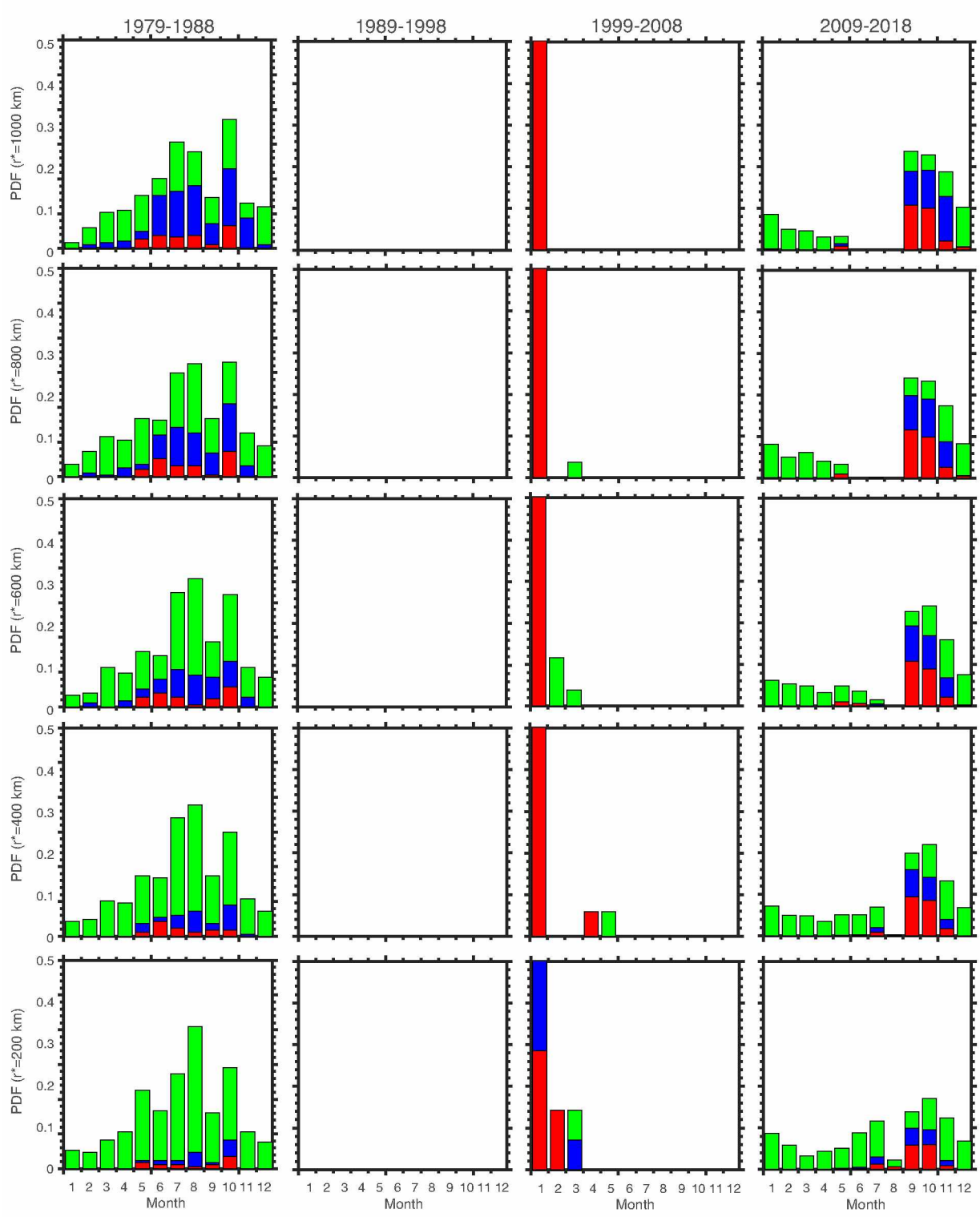

Figure 38. Stacked bar charts shown the propability distribution function (PDF) of the storm counts over the Beaufort Sea. Blue, green, and red sectors represent storms categorized into $\boldsymbol{G_2^-}$, $\boldsymbol{G_2^0}$, and $\boldsymbol{G_2^+}$ groups respectively.

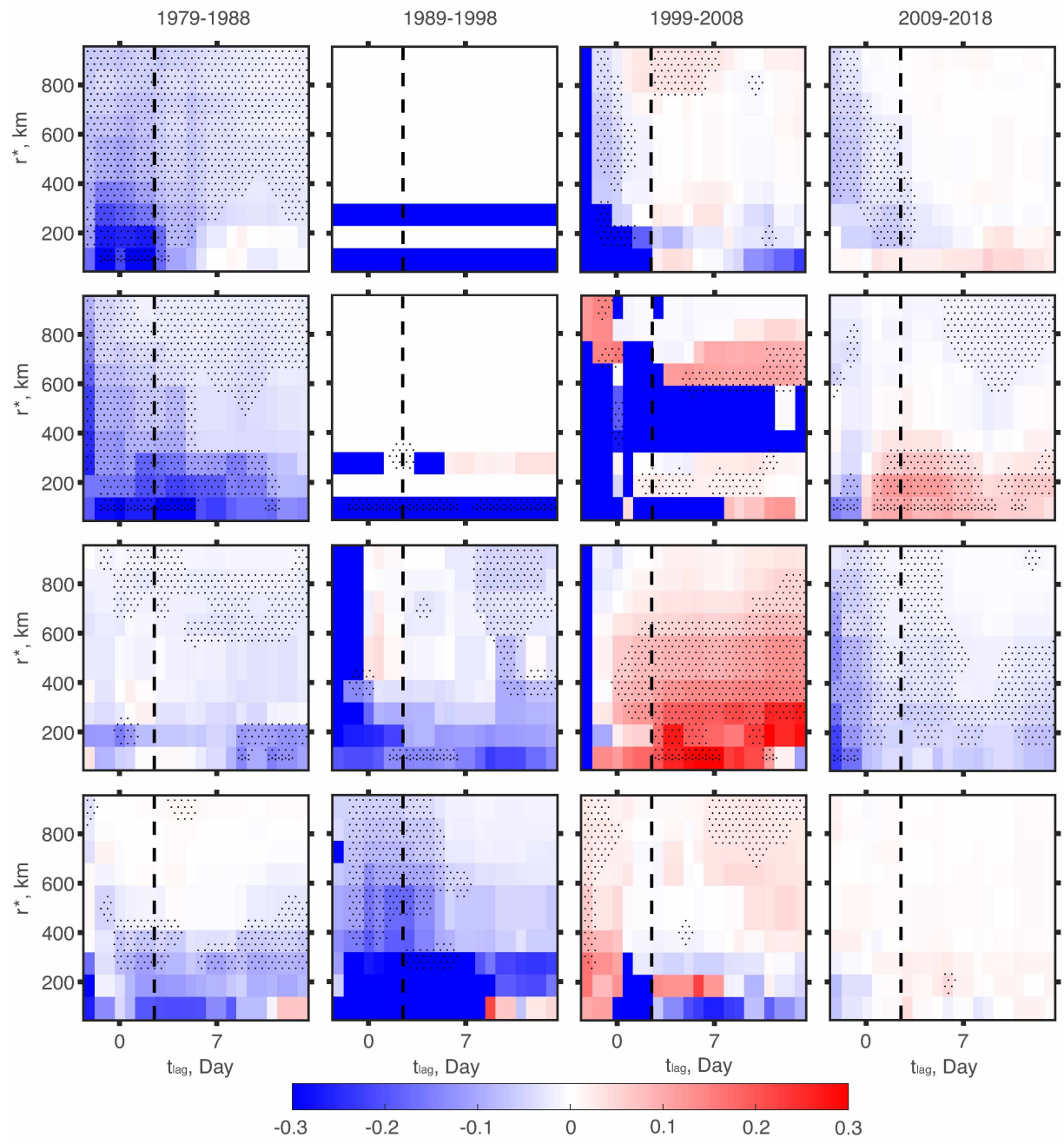

Figure 39. The ratio between sea ice area difference between SC/Post-SC and CC/Post-CC and the total area with radius $\boldsymbol{r^*}$ for $\boldsymbol{G_1^+}$ (top), $\boldsymbol{G_1^-}$, $\boldsymbol{G_2^+}$, and $\boldsymbol{G_2^-}$ (bottom) span from 1979-1988 (left), 1989-1998, 1999-2008, and 2009-2018 (right) over the Beaufort Sea. The thick black dashed line represents $\boldsymbol{t_{lag} = -2}$ days.

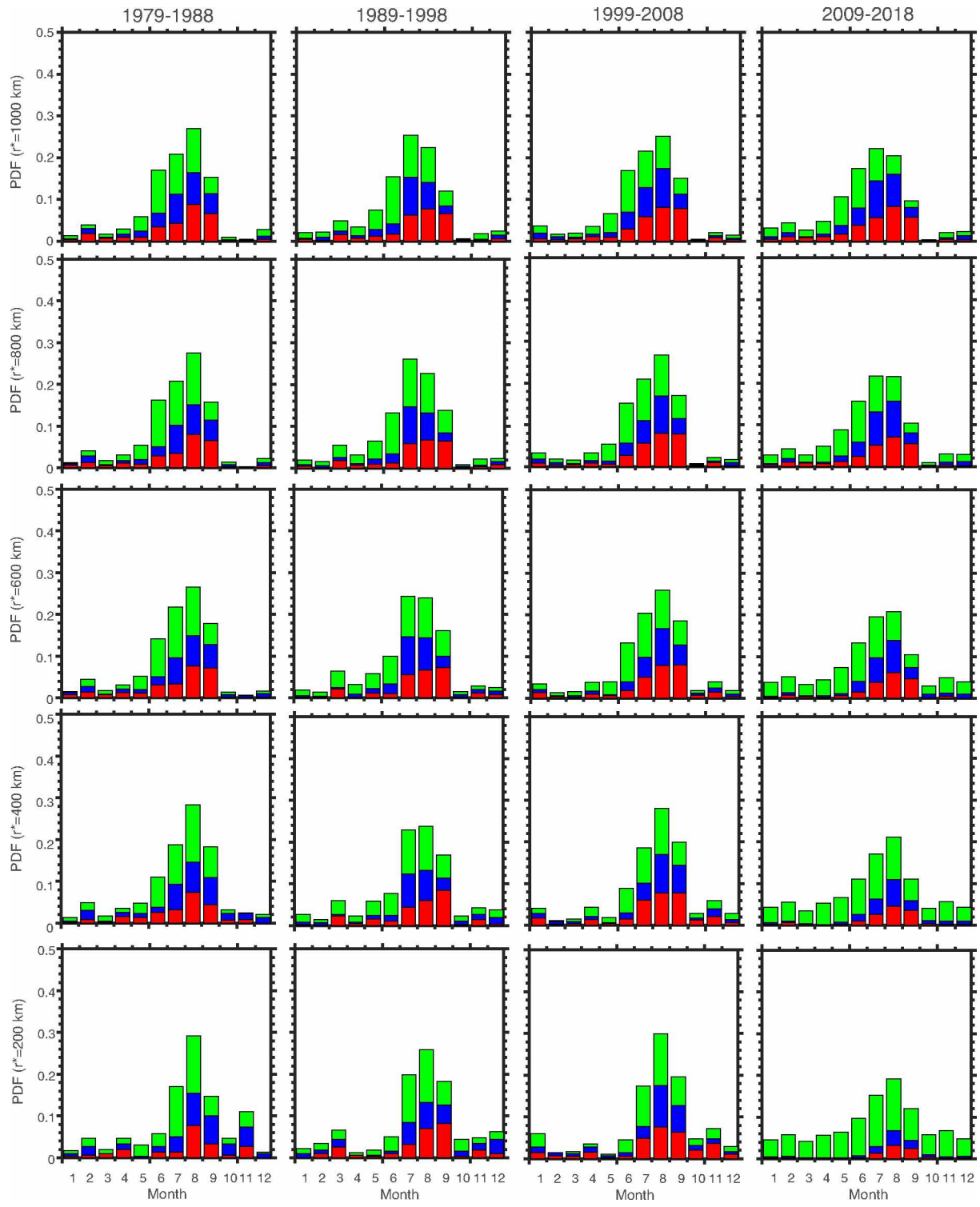

Figure 40. Stacked bar charts shown the propability distribution function (PDF) of storm counts over Central Arctic. Blue, green, and red sectors represent storms from $\boldsymbol{G_1^-}$, $\boldsymbol{G_1^0}$, and $\boldsymbol{G_1^+}$ respectively.

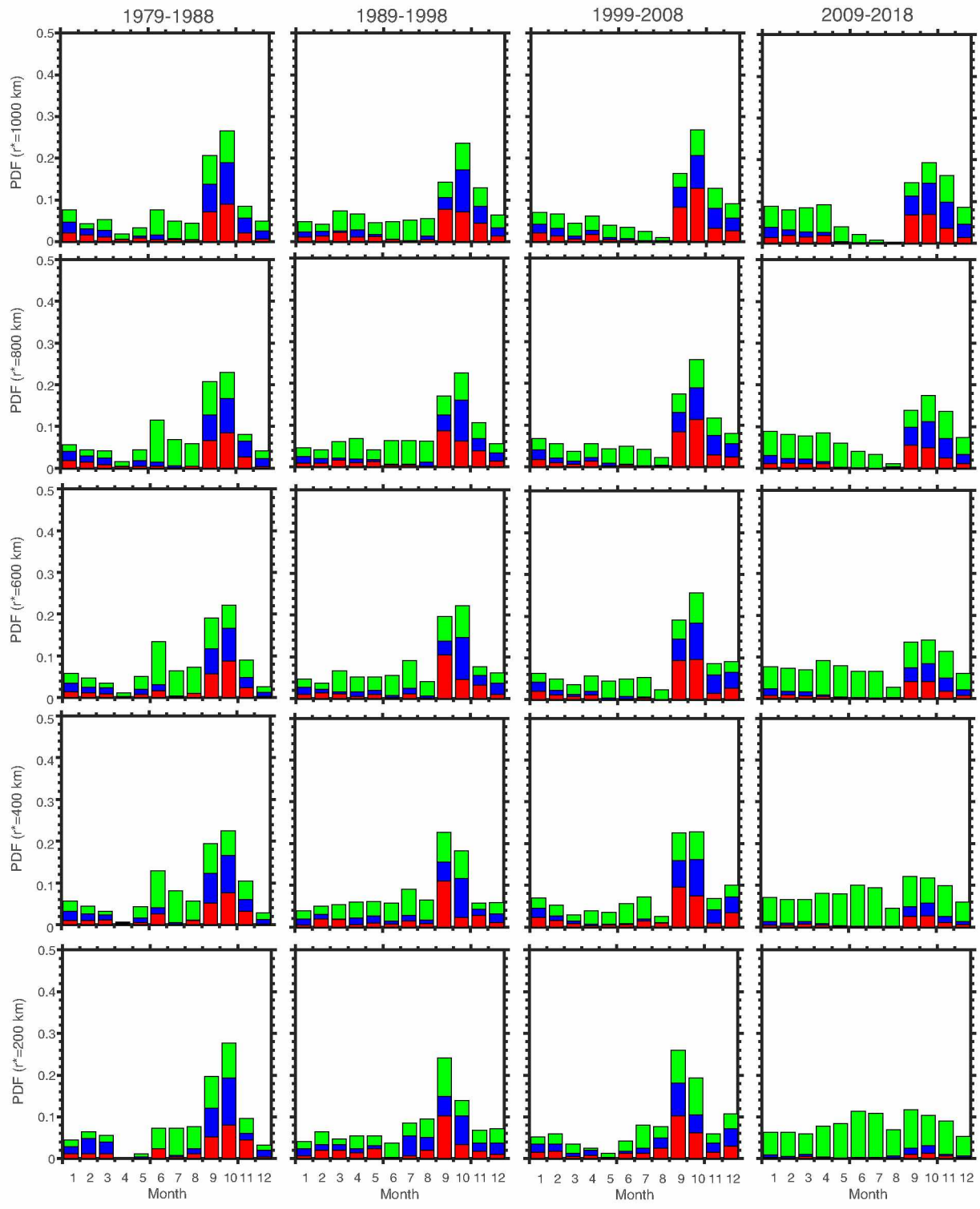

Figure 41. Stacked bar charts shown the propability distribution function (PDF) of the storm counts over the Central Arctic. Blue, green, and red sectors represent storms categorized into $\boldsymbol{G_2^-}$, $\boldsymbol{G_2^0}$, and $\boldsymbol{G_2^+}$ groups respectively.

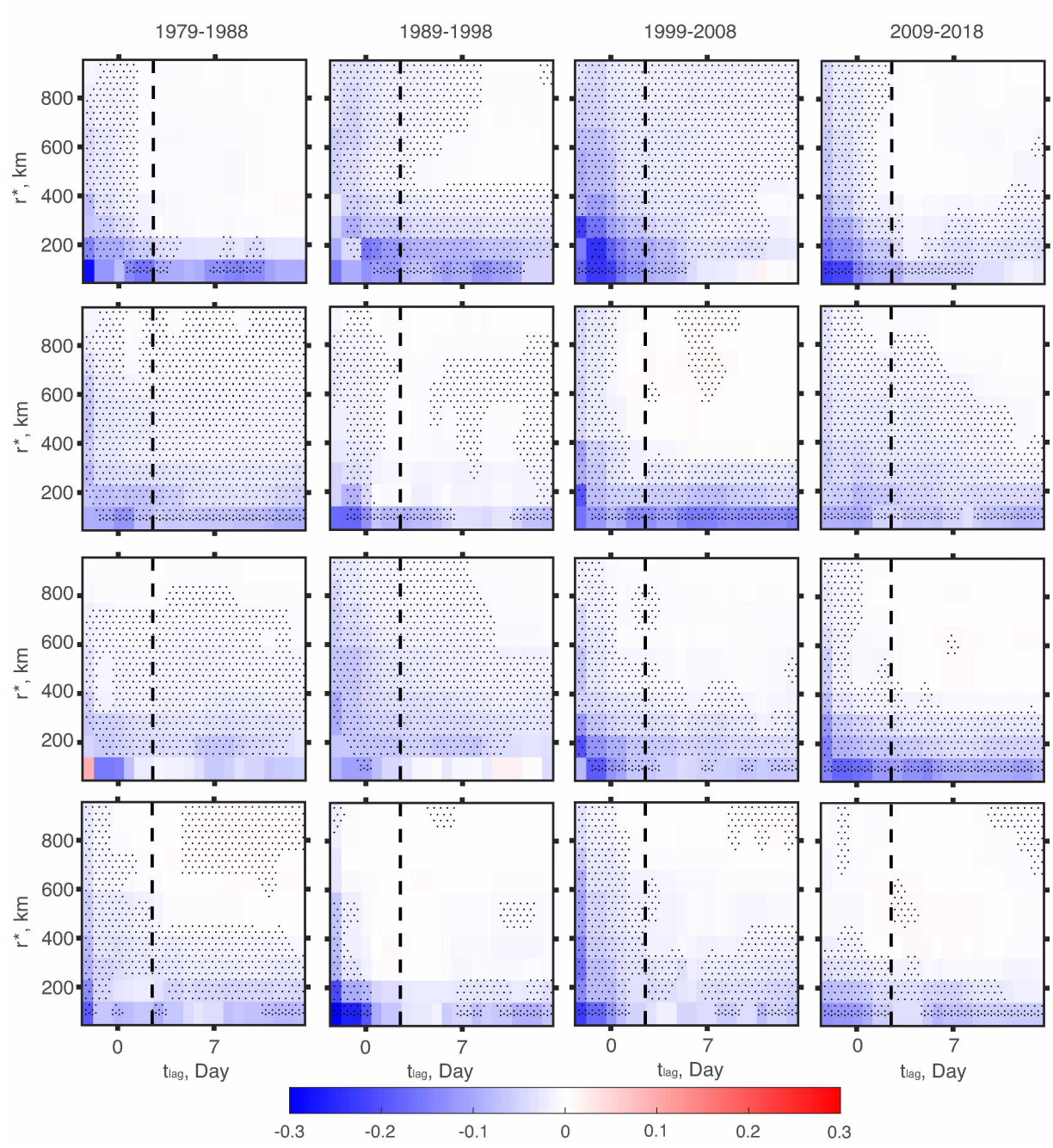

Figure 42. The ratio between sea ice area difference between SC/Post-SC and CC/Post-CC and the total area with radius $\boldsymbol{r^*}$ for $\boldsymbol{G_1^+}$ (top), $\boldsymbol{G_1^-}$, $\boldsymbol{G_2^+}$, and $\boldsymbol{G_2^-}$ (bottom) span from 1979-1988 (left), 1989-1998, 1999-2008, and 2009-2018 (right) over the Central Arctic Seas. The thick black dashed line represents $\boldsymbol{t_{lag} = -2}$ days.

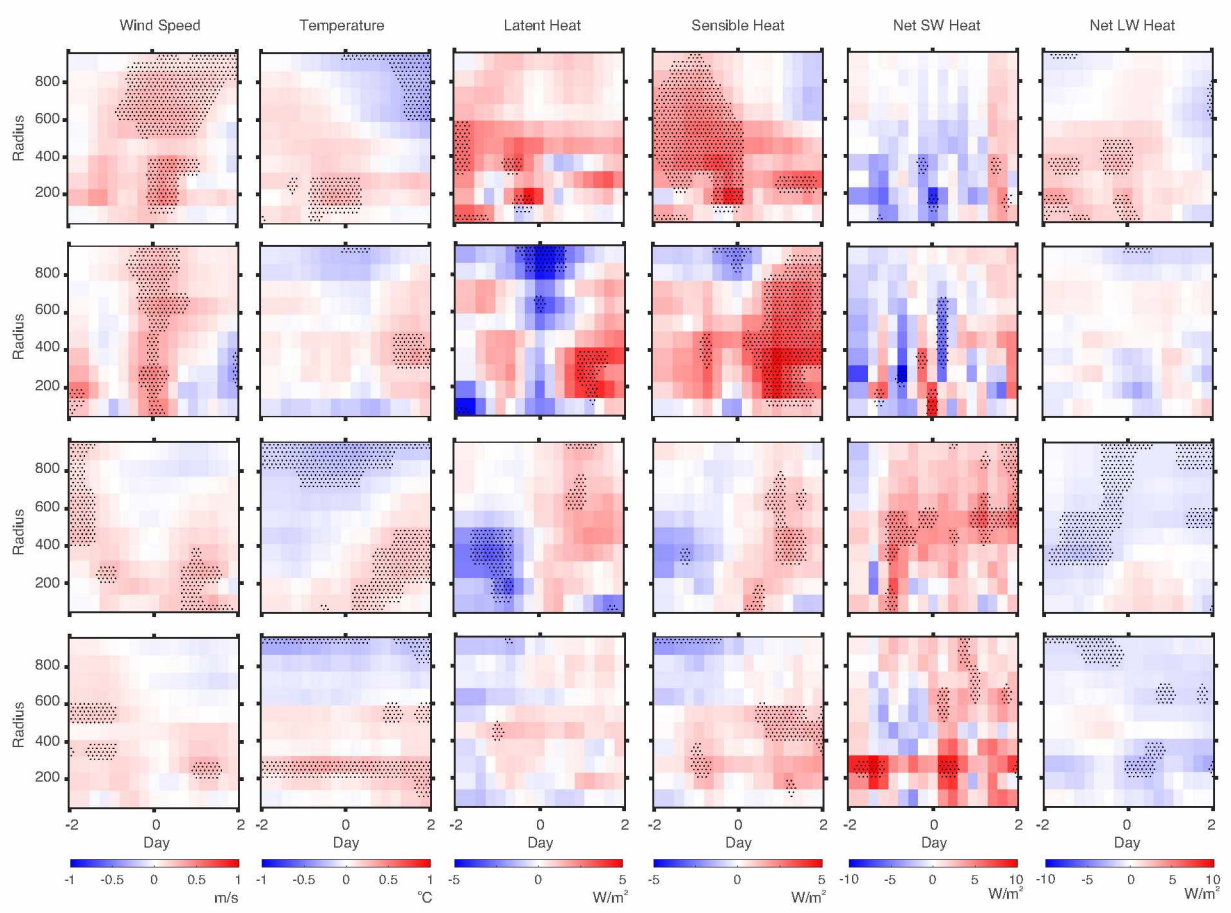

Figure 43. Composite fields for storms over the Chukchi Sea in 1979-1988 including surface winds, surface air temperature, latent heat flux, sensible heat flux, surface net SW flux, and surface net LW flux from left to right. Color represents the difference between SC and CC for each field. From top row to bottom row, the composite files correspond to storms categorized into $\boldsymbol{G_1^+}$, $\boldsymbol{G_1^-}$, $\boldsymbol{G_2^+}$, and $\boldsymbol{G_2^-}$ groups.

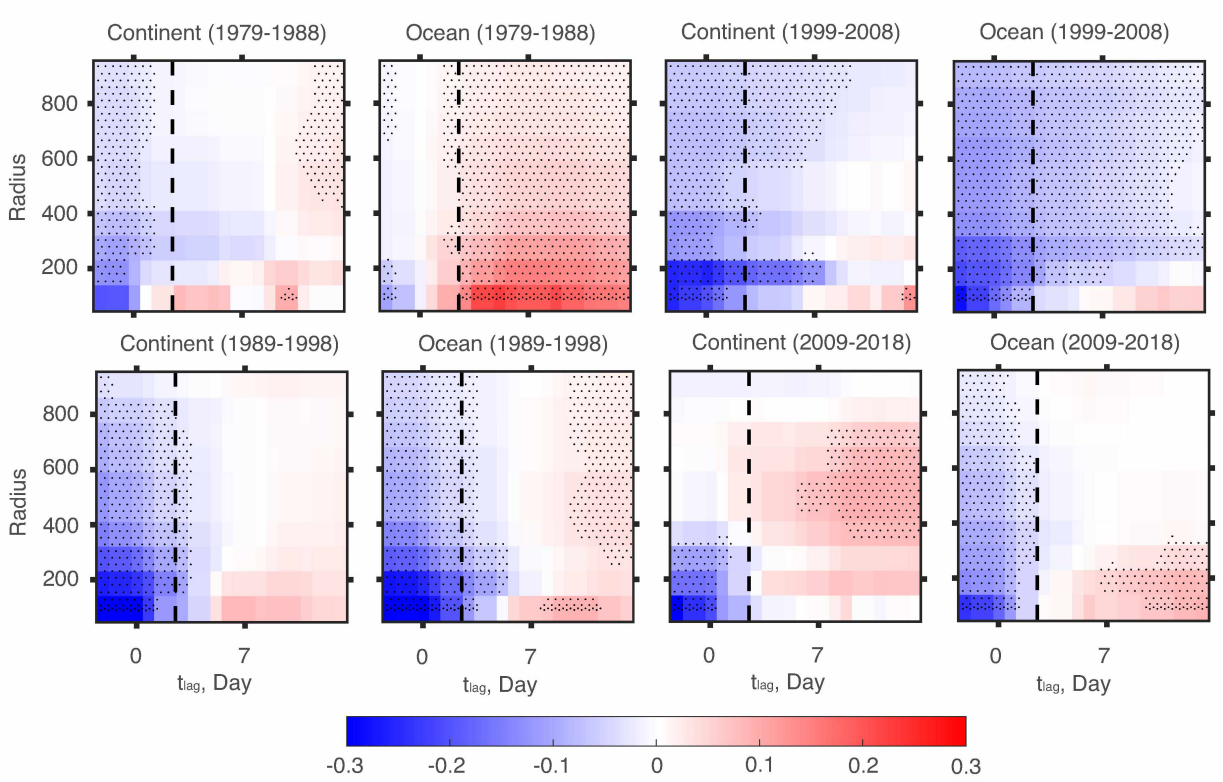

Figure 44. The ratio between sea ice area difference between SC/Post-SC and CC/Post-CC and the total area with radius $\boldsymbol{r}^*$ for $\boldsymbol{G_1^+}$ span from 1979-1988, 1989-1998, 1999-2008, and 2009-2018 over the East Siberian and Laptev Seas. Storms are further categorized into continental and ocean storms based on $\boldsymbol{F_{cont}}$. The thick black dashed line represents $\boldsymbol{t_{lag} = -2}$ days.

4.10 Tables

Table 5. Total storm track numbers of and their overall trends (numbers in parenthesis) in different regions and in different seasons, 1979-2018

	Annual Total	Winter	Spring	Summer	Autumn
All	563.5 (0.812)	140.3 (0.388)	138.5 (0.206)	136.2 (0.015)	148.5 (0.204)
Bering Sea	110.2 (-0.022)	30.1 (0.079)	26.6 (-0.106)	23.5 (-0.094)	30.0 (0.100)
Chukchi Sea	43.5 (**0.401**)	7.3 (**0.167**)	8.6 (0.092)	16.9 (0.078)	10.7 (0.063)
E. Siberian and Laptev Sea	71.8 (0.139)	8.9 (-0.04)	17.3 (0.018)	27.7 (**0.164**)	18.0 (-0.005)
Barents and Kara Seas	159.4 (0.207)	39.0 (-0.076)	43.3 (**0.275**)	35.3 (0.078)	41.9 (-0.070)
GIN Seas	303.8 (**2.737**)	85.9 (**0.966**)	80.4 (**0.802**)	60.8 (0.412)	76.8 (**0.557**)
Central Arctic Ocean	111.7 (0.382)	21.7 (0.082)	23.9 (0.132)	36.1 (0.112)	30.0 (0.056)
Beaufort Sea	37.0 (0.078)	6.6 (0.002)	6.2 (-0.007)	13.3 (0.041)	10.8 (0.041)

Statistically significant slopes at the $p < 0.05$ level are shown in bold

Table 6. The average deep storm counts, the overall trends, the percentage of deep storms relative to the total storm counts in different regions and in different seasons from 1979-2018.

	Total	Winter	Spring	Summer	Autumn
All storms					
Mean	273.8	100.0	57.4	33.4	83.0
Tend	0.531	0.274	0.057	0.015	0.185
	48.6%	71.3%	41.4%	24.5%	55.9%
Percentage					
Bering Sea					
Mean	64.5	24.3	14.6	5.7	19.9
Tend	0.002	0.072	-0.041	-0.055	0.025
	58.5%	80.7%	54.9%	24.3%	66.3%
Percentage					
Chukchi Sea					
Mean	27.3	6.1	4.7	8.9	7.6
Tend	**0.321**	**0.157**	0.067	0.038	0.059
	62.8%	83.6%	54.7%	52.7%	71.0%
Percentage					
E. Siberian and Laptev Sea					
Mean	20.8	4.2	4.5	5.9	6.2
Tend	0.032	-0.054	-0.027	0.052	0.060
	29.0%	47.2%	26.0%	21.3%	34.4%
Percentage					
Barents and Kara Seas					
Mean	72	25.1	15.2	9.2	22.5
Tend	0.035	-0.127	0.119	0.039	0.004
	45.2%	64.4%	35.1%	26.1%	53.7%
Percentage					
GIN Seas					
Mean	180.1	68.9	42.1	16.7	52.4
Tend	**2.149**	**0.841**	**0.610**	0.159	**0.539**
	59.3%	80.2%	52.4%	27.5%	68.2%
Percentage					
Central Arctic Ocean					
Mean	40.4	11.0	7.1	10.7	11.7
Tend	0.155	0.079	-0.021	0.011	0.086
	36.2%	50.7%	29.7%	29.6	39.0%
Percentage					
Beaufort Sea					
Mean	9.0	2.4	0.8	2.9	3.0
Tend	0.063	0.014	-0.006	0.008	0.035
Percentage	24.3%	36.4%	12.9%	21.8%	27.8%

Statistically significant slopes at the $p < 0.05$ level are shown in bold

Table 7. The average continental life time fraction for storms categorized into the G_1^+ group at different r^*.

r^*	1979-1988	1989-1998	1999-2008	2009-2018
100	0.28	0.30	0.28	0.22
200	0.35	0.27	0.30	0.20
300	0.31	0.24	0.30	0.20
400	0.29	0.24	0.26	0.17
500	0.28	0.22	0.27	0.16
600	0.27	0.23	0.28	0.15
700	0.25	0.22	0.27	0.17
800	0.25	0.21	0.27	0.18
900	0.25	0.22	0.26	0.18
1000	0.26	0.21	0.27	0.18

Table 8. The average continental life time fraction for storms categorized into the $\boldsymbol{G_1^-}$ group at different $\boldsymbol{r^*}$.

r^*	1979-1988	1989-1998	1999-2008	2009-2018
100	0.37	0.33	0.29	0.31
200	0.35	0.32	0.30	0.31
300	0.33	0.34	0.30	0.30
400	0.32	0.35	0.29	0.32
500	0.30	0.35	0.27	0.35
600	0.30	0.33	0.28	0.34
700	0.28	0.33	0.27	0.34
800	0.29	0.33	0.27	0.34
900	0.29	0.32	0.27	0.33
1000	0.29	0.31	0.27	0.34

Table 9. The average continental life time fraction for storms categorized into the $\boldsymbol{G_2^+}$ group at different $\boldsymbol{r^*}$.

r^*	1979-1988	1989-1998	1999-2008	2009-2018
100	0.28	0.39	0.34	0.30
200	0.29	0.34	0.31	0.29
300	0.31	0.33	0.31	0.28
400	0.30	0.33	0.34	0.30
500	0.33	0.32	0.39	0.28
600	0.32	0.32	0.37	0.29
700	0.31	0.33	0.39	0.28
800	0.28	0.35	0.38	0.25
900	0.28	0.35	0.35	0.24
1000	0.27	0.36	0.34	0.23

Table 10. The average continental life time fraction for storms categorized into the $\boldsymbol{G_2^-}$ group at different $\boldsymbol{r^*}$.

r^*	1979-1988	1989-1998	1999-2008	2009-2018
100	0.37	0.29	0.32	0.35
200	0.42	0.29	0.36	0.35
300	0.38	0.27	0.32	0.37
400	0.37	0.27	0.31	0.35
500	0.34	0.29	0.32	0.35
600	0.33	0.27	0.33	0.36
700	0.33	0.26	0.32	0.37
800	0.35	0.27	0.32	0.36
900	0.33	0.28	0.31	0.37
1000	0.33	0.29	0.32	0.37

Table 11. The temporal correlation coefficient between storm counts in group $\boldsymbol{G_1^+}$ and total sea ice area over seven regions from 1979-2018.

r^*	Bering Sea	Chukchi Sea	E. Siberian and Laptev Sea	Barents and Kara Seas	GIN Seas	Central Arctic Ocean	Beaufort Sea
100	0.06	-0.15	-0.57	-0.32	-0.07	-0.79	-0.34
200	-0.05	-0.24	-0.47	-0.40	-0.12	-0.72	-0.31
300	-0.09	-0.16	-0.45	-0.45	-0.13	-0.60	-0.29
400	-0.11	-0.15	-0.47	-0.45	-0.14	-0.54	-0.26
500	-0.03	-0.22	-0.40	-0.45	-0.12	-0.40	-0.25
600	0.01	-0.21	-0.37	-0.45	-0.08	-0.39	-0.28
700	0.04	-0.25	-0.35	-0.40	-0.09	-0.31	-0.27
800	0.03	-0.29	-0.36	-0.40	-0.11	-0.28	-0.26
900	0.03	-0.30	-0.32	-0.40	-0.13	-0.33	-0.25
1000	0.06	-0.35	-0.29	-0.39	-0.14	-0.35	-0.22

Table 5. The temporal correlation coefficient between storm counts in group G_1^- and total sea ice area over seven regions from 1979-2018.

r^*	Bering Sea	Chukchi Sea	E. Siberian and Laptev Sea	Barents and Kara Seas	GIN Seas	Central Arctic Ocean	Beaufort Sea
100	0.18	-0.24	-0.37	-0.50	-0.12	-0.75	-0.35
200	0.29	-0.07	-0.43	-0.51	-0.17	-0.69	-0.38
300	0.30	-0.14	-0.41	-0.44	-0.18	-0.67	-0.41
400	0.25	-0.19	-0.35	-0.49	-0.21	-0.67	-0.35
500	0.26	-0.18	-0.28	-0.53	-0.24	-0.67	-0.39
600	0.20	-0.18	-0.28	-0.55	-0.26	-0.6	-0.40
700	0.10	-0.22	-0.30	-0.50	-0.27	-0.54	-0.34
800	0.07	-0.23	-0.30	-0.49	-0.31	-0.53	-0.26
900	0	-0.17	-0.32	-0.47	-0.32	-0.46	-0.26
1000	-0.05	-0.17	-0.35	-0.47	-0.34	-0.40	-0.27

Table 6. The temporal correlation coefficient between storm counts in group G_2^+ and total sea ice area over seven regions from 1979-2018.

r^*	Bering Sea	Chukchi Sea	E. Siberian and Laptev Sea	Barents and Kara Seas	GIN Seas	Central Arctic Ocean	Beaufort Sea
100	0.10	-0.07	-0.57	-0.55	-0.03	-0.70	-0.34
200	0.31	-0.07	-0.58	-0.54	-0.05	-0.75	-0.45
300	0.38	-0.02	-0.49	-0.53	-0.07	-0.74	-0.47
400	0.42	0.02	-0.39	-0.54	-0.10	-0.64	-0.43
500	0.46	0.03	-0.39	-0.51	-0.09	-0.61	-0.44
600	0.41	0.01	-0.32	-0.55	-0.09	-0.61	-0.45
700	0.37	0	-0.32	-0.54	-0.14	-0.57	-0.46
800	0.37	-0.11	-0.32	-0.50	-0.19	-0.50	-0.44
900	0.36	-0.08	-0.28	-0.46	-0.24	-0.44	-0.42
1000	0.39	-0.09	-0.24	-0.47	-0.29	-0.38	-0.41

Table 7. The temporal correlation coefficient between storm counts in group G_2^- and total sea ice area over seven regions from 1979-2018.

r^*	Bering Sea	Chukchi Sea	E. Siberian and Laptev Sea	Barents and Kara Seas	GIN Seas	Central Arctic Ocean	Beaufort Sea
100	0.09	-0.37	-0.49	-0.40	-0.04	-0.78	-0.40
200	0.30	-0.17	-0.59	-0.39	-0.11	-0.75	-0.39
300	0.30	-0.29	-0.60	-0.35	-0.11	-0.62	-0.39
400	0.19	-0.30	-0.62	-0.35	-0.12	-0.54	-0.38
500	0.10	-0.23	-0.66	-0.35	-0.14	-0.48	-0.34
600	0.03	-0.25	-0.66	-0.36	-0.15	-0.47	-0.30
700	0.06	-0.16	-0.62	-0.38	-0.16	-0.42	-0.29
800	0.06	-0.17	-0.62	-0.42	-0.16	-0.36	-0.28
900	0.11	-0.17	-0.59	-0.44	-0.15	-0.28	-0.29
1000	0.07	-0.15	-0.57	-0.44	-0.14	-0.19	-0.27

4.11 References

Boisvert, L. N., A. A. Petty, and J. C. Stroeve (2016), The impact of the extreme winter 2015/16 Arctic cyclone on the Barents–Kara Seas. *Mon. Wea. Rev.*, **144**, 4279–4287, doi:10.1175/MWR-D-16-0234.1.

Brümmer, B. and H. Hoeber (1999), A mesoscale cyclone over the Fram Strait and its effects on the sea ice. *J. Geophys. Res.*, **104**(D16), 19085–19098.

Brümmer B., G. Müller, B. Affeld, R. Gerdes, M. Karcher, F. Kauker (2001), Cyclones over Fram Strait: impact on sea ice and variability. *Polar Res,* **20**(2):147–152.

Brümmer B., and Coauthors (2008), Impact of a Fram Strait cyclone on ice edge, drift, divergence, and concentration: possibilities and limits of an observational analysis. *J. Geophys. Res.,***113**, C12003, doi:10.1029/2007JC004149.

Comiso, J. C. (2017), *Bootstrap Sea Ice Concentrations from Nimbus-7 SMMR and DMSP SSM/I-SSMIS, Version 3.* (Indicate subset used). Boulder, Colorado USA. NASA National Snow and Ice Data Center Distributed Active Archive Center. doi: https://doi.org/10.5067/7Q8HCCWS4I0R. (Date Accessed).

Curry, J. A., J. L. Schramm, and E. E. Ebert (1993), Impact of clouds on the surface radiation balance of the Arctic Ocean, *Meteorol. Atmos. Phys.*, **51**, 197–217.

Intrieri, J. M., and Coauthors (2002), An annual cycle of Arctic surface cloud forcing at SHEBA, *J. Geophys. Res.*, **107**(C10), 8039, doi:10.1029/2000JC000439.

Kriegsmann, A., and B. Brümmer (2014), Cyclone impact on sea ice in the central Arctic Ocean: A statistical study, *Cryosphere*, **8**, 303–317, doi:10.5194/tc-8-303-2014.

Maslanik, J. A., and R. G. Barry (1989), Short-term interactions between atmospheric synoptic conditions and sea-ice behaviour in the Arctic, *Ann. Glaciol.*, **12**, 113–117, 1.

Onarheim, I. H., Eldevik, T., Smedsrud, L. H., and J. C. Stroeve (2018). Seasonal and regional manifestation of Arctic sea ice loss. *J. Clim.*, **31**(12), 4917–4932. https://doi.org/10.1175/JCLI-D-17-0427.1.

Overland J. E., and P. Turet (1994), Variability of the atmospheric energy flux across 70°N computed from the GFDL data set. In: The Polar Oceans and Their Role in Shaping the Global Environment, Geophysical Monograph Series 85, Johannessen OM, Muench RD, Overland JE (eds). American Geophysical Union: Washington, DC.

Parkinson, C. L., and J. C. Comiso (2013), On the 2012 record low Arctic sea ice cover: Combined impact of preconditioning and an August storm, *Geophys. Res. Lett.*, **40**, 1356–1361, doi:10.1002/grl.50349.

Pickart, R. S., and Coauthors (2009), Upwelling on the continental slope of the Alaskan Beaufort Sea: Storms, ice, and oceanographic response, *J. Geophys. Res.*, **114**, C00A13, doi:10.1029/2008JC005009.

Polyakov, I. V., A. V. Pnyushkov, and T. A. Timokhov (2012), Warming of the intermediate Atlantic Water of the Arctic Ocean in the 2000s, *J. Clim.*, **25**(23), 8362–8370, doi:10.1175/JCLI-D-12-00266.1.

Rae, J.G.L., A. D. Todd, E. W. Blockley, J. K. Ridley (2017), How much should we believe correlations between Arctic cyclones and sea ice extent? *Cryosphere*, **11**, 3023–3034.

Rigor, I. G., J. M. Wallace, and R. L. Colony (2002), Response of Sea Ice to the Arctic Oscillation, *J. Clim.*, **15**, 2648–2663.

Serreze M. (1995), Climatological aspects of cyclone development and decay in the Arctic. *Atmos Ocean*, **33**(1), 1–23, https://doi. org/10.1080/07055900.1995.9649522.

Serreze, M. C, F. Carse, R. G. Barry, and J. C. Rogers (1997), Icelandic low activity: climatological features, linkages with the NAO, and relationships with recent changes in the Northern Hemisphere circulation. *J. Clim.*, **10**, 453-164.

Simmonds I., C. Burke, and K. Keay (2008), Arctic climate change as manifest in cyclone behavior. *J Clim*, **21**(22), 5777–5796. https://doi. org/10.1175/2008jcli2366.1

Simmonds, I., and I. Rudeva (2012), The great Arctic cyclone of August 2012, *Geophys. Res.Lett.*, **39**, L23709, doi:10.1029/2012GL054259.

Sorteberg A, J. E. Walsh (2008), Seasonal cyclone variability at 70°N and its impact on moisture transport into the Arctic. *Tellus,* **60**A, 570 – 586, DOI:10.1111/j.16000870.2008.00314.x.

Steele, M., and J. H. Morison (1993), Hydrography and vertical fluxes of heat and salt northeast of Svalbard in autumn, *J. Geophys. Res.*, **98**, 10,013, doi:10.1029/93JC00937.

Wei, J., X. Zhang, and Z. Wang (2019), Impacts of extratropical storm tracks on Arctic sea ice export through Fram Strait. *Clim. Dyn.*, **52**(3-4), 2235–2246. https://doi.org/10.1007/s00382-018-4254-8.

Yang, J., J. Comiso, R. Krishfield, and S. Honjo (2001), Synoptic storms and the development of the 1997 warming and freshening event in the Beaufort Sea, *Geophys. Res. Lett.*, **28**, 799–802, 2001, doi:10.1029/2000JC000583.

Yang, J., J. Comiso, D. Walsh, R. Krishfield, and S. Honjo (2004), Storm-driven mixing and potential impact on the Arctic Ocean, *J. Geophys. Res.*, **109**, C04008, doi:10.1029/2001JC001248.

Zhang J., R. Lindsay, A. Schweiger, and M. Steele (2013), The impact of an intense summer cyclone on 2012 Arctic sea ice retreat. *Geophys. Res. Lett.*, **40**(4), 720–726.

Chapter 5 Conclusions

The overarching goal for this study is to explore to what extent do storms impact sea ice changes from a synoptic-scale to a climate scale. To answer this question, we split my thesis into three subtopics that include: a storm case study that based on data collected by the Korean icebreaker ARAON, a model study that explored how pan-Arctic scale sea ice thickness distribution is impacted by the magnitude of the sea ice strength and the air-ice drag, and a composite analysis for all storms passing over seven regions from 1979 to 2018 based on ERA-Interim reanalysis and satellite-based sea ice observations.

Each subtopic is connected to sea ice changes but with distinct emphases. In conducting the observational-based storm case study, we emphasize storm-induced ocean processes that may potentially impact sea ice changes through modifying the sea ice energy budget terms. In Chapter 2, we examined how the storm impacts the state of and changes in sea ice and upper ocean by employing the in-situ observations on board the icebreaking R/V Araon. Two long-lived, intense storms were captured on August 2016. During the storm period, less energy was received over the sea ice surface compared with the pre-storm and post-storm conditions. However, the storm dynamically enhanced upper-ocean mixing and induced upwelling of Pacific-origin warm water due to Ekman pumping effects. The changing ocean dynamics result in noted upper-ocean warming and, in turn, an increase in ocean-to-sea ice heat flux, which is larger than the net heat loss from the sea ice surface due to storms. As a consequence, the sea ice area decreases accelerated. After storms moved away, excessive sea ice melting lead to a rapid salinity decrease within the SML due to the freshwater release. Therefore, the enhanced

static stability within the halocline may prohibit further upward heat transport after storms moved away.

Storm case studies often focus on extreme storms and are confined within limited spatial and temporal scales. Therefore, to generalize findings based on case studies to the entire Arctic is challenging. Since many factors may contribute to long-term sea ice variations, to gain a better understanding of how storms impact sea ice in a climate scale, we first investigate the physical mechanisms controlling long-term sea ice changes using model simulations. In Chapter 3, we identify key processes controlling the pan-Arctic scale sea ice thickness distribution without the impact on storms. We analyzed variations of sea ice thickness distribution from our idealized model simulations under different air-ice drag and sea ice strength conditions. We found that sea ice volume, velocity, and thickness are highly sensitive to perturbed air-ice momentum flux and sea ice strength. The decrease in sea ice strength alone results in thicker ice and therefore a larger ice volume throughout the year since more kinetic energy is converted to the potential energy to build sea ice ridge, instead of causing frictional loss. Our results also indicate that increased sea ice strength or decreased air-ice momentum flux causes counter-clockwise rotation of the ice transpolar drift, resulting in an increase in sea ice export through Fram Strait and therefore reduction of the pan-Arctic sea ice thickness. After applying a tracer technique to our model results, we found that sea ice tends to have a larger magnitude of the seasonal cycle over the western Arctic and associated with a broader sea ice thickness distribution. As the tracer moved into the eastern Arctic, the dynamic process becomes dominant in governing the sea ice thickness, and the sea ice thickness distribution becomes much narrower.

In Chapter 4, we explored the general role of storm impact on sea ice area based on a newly developed composite analysis. This composite analysis is different compared with previous studies in several ways: our composite analysis combines both the Lagrangian perspective in terms of storm track and the Eulerian perspective in terms of local sea ice changes, our selection of subregions considered not only the geophysical locations but also the bathymetry, our analysis includes all storms spanning from 1979 to 2018 focusing not only on their short-term and mid-term but also on long-term impacts on sea ice, our composite analysis investigated the storm impact on sea ice in a radius-time space, and our analysis considered long term sea ice variations by splitting the time period into four fixed ten-year windows. Through this analysis, we found storms over periphery seas tend to cause sea ice decrease starting from two days before the storm arrived until two days or one week after the storm moved away. This finding is consistent with our storm case analysis shown in Chapter 2. Results also indicate sea ice tends to recover to or even exceed the climatological trends one or two weeks after storms moved away. Storms that occur during the fall tend to have a larger impact on sea ice compared with summer storms. Storms over the western Arctic (Chukchi, East Siberian, and Laptev Seas) tend to have a larger impact on sea ice area compared with the eastern Arctic (Barents and Kara Seas). Under no-storm conditions (Chapter 4), thermodynamic processes are more dominant in controlling sea ice properties over the western Arctic compared with the eastern Arctic. The sea ice thickness distribution is relatively broader over the western Arctic, and thin ice has a faster response time to external forcings (via both dynamic and thermodynamic processes) induced by storms compared with thicker ice. Not surprisingly, storms have less short- and mid-term impact on sea ice over the eastern Arctic since the sea ice thickness distribution becomes narrower and the mode shifted to a larger sea ice thickness bin compared with the western

Arctic. Over the central Arctic, storm counts are highly correlated with the total sea ice area over the masked region. More storms reach the central Arctic resulting in less sea ice area; therefore, storms tend to have a long-term impact on sea ice area. As reflected by the composite analysis of energy budget terms, storms may enhance energy exchanges between mid-latitudes and high latitudes over the periphery seas and result in large sea ice area perturbations. As storms move into the Central Arctic, they serve as a primary mechanism transporting heat and moisture and causing persistent sea ice area decrease. Over GIN seas, sea ice properties are more likely controlled by changes in the large-scale automorphic circulation and sea ice strength (Chapter 3). Storms only have limited impact on sea ice properties.

Increased frequency of storms raises great concerns about its impacts on sea ice and upper ocean over recent decades. These concerns have also extended to the broader communities, in particular considering the increasing economic and societal activities over the Arctic. The declining Arctic sea ice opens up faster shipping channels, improves accessibility to Arctic ports, and reduces costs to explore massive mineral and fishery resources in the Arctic. An updated storm track statistic over the pan-Arctic scale (Chapter 4) potentially helps to improve the design of coastal energy facilities and new shipping routes. The storm track information also helps better understanding and credible assessment of changes in nutrient production and transport, which are vital to fishery management and ecosystems since nutrient production and transport are key processes affecting the efficiency of transfer of primary production through the food web. Springtime recurrent nutrient bloom is relatively well understood and predicted. After the nutrients in the euphotic zone become depleted, the vertical transport of nutrients from deeper water becomes important. However, storm-associated episodic bloom is still poorly understood, especially over high latitudes. Storms directly impact nutrient transport via two

major pathways. Firstly, during the storm period, strong surface winds induced by storms intensify the vertical ocean mixing (Findlay et al., 2006; Marta et al., 1990). Secondly, interactions between wind stress and surface layer current will induce near-inertial oscillation (Pollard 1980), which will last for several days and intermittent by generate nutrient flux through the pycnocline (Rippeth et al., 2009). Storms may also indirectly alter nutrient production and transport through their impact on sea ice (Chapter 1 and Chapter 4). The decline of the sea ice, consequently increasing the aware of open water, leads to more absorption of the shortwave radiation within the ocean surface layer, which allows near-surface phytoplankton to receive more solar irradiance. Additionally, sea ice serves as a barrier between the atmosphere and the ocean, and the persistence of sea ice alters the atmosphere-ocean wind stress, which varies the vertical nutrient transport in consequence. Therefore, results from this study may potentially help us to better understand the past and predict the future fish productions over the Arctic.

Given the current results on how storm impact sea ice based on observations and reanalysis data, it is of future interest to use this new composite analysis method to further explore storm-induced physical processes and their impact on sea ice and upper ocean structure using coupled ocean-sea ice model simulations using the inter-annual forcing (IAF) data sets.

References

Findlay, H. S., A. Yool, M. Nodale, and J. W. Pitchford, 2006: Modelling of autumn plankton bloom dynamics. *J. Plankton Res.*, **28**, 209-220, doi:10.1093/plankt/fbi114.

Marta, J., R. R. Bidigare, and T. D. Dickey, 1990: Nutrients and mixing, chlorophyll and phytoplankton growth, *Deep-Sea Res. Part A*, **37**, 127-143.

Pollard, R. T. 1980: Properties of near-surface inertial oscillations. *J. Phys. Oceanogr.*, **10**(3), 385-398.

Rippeth, T. P., P. Wiles, M. R. Palmer, J. Sharples, and J. Tweddle, 2009: The diapcynal nutrient flux and shear-induced diapcynal mixing in the seasonally stratified western Irish Sea. *Cont. Shelf Res.*, **29**(13), 1580-1587.

Chapter 6 Appendix

ACW: Alaskan Coastal Water

AMSR2: Advanced Microwave Scanning Radiometer 2

ARTIST: Arctic Radiation and Turbulence Interaction Study

CESM: Community Earth System Model

CSW: Chukchi Summer Water

CTD: Conductivity, Temperature, and Depth

ECMWF: European Centre for Medium-Range Weather Forecasts

IAF: Inter-Annual Forcing

IBRV: Icebreaking Research Vessel

IMB**:** Ice Mass Balance Buoy

NYF: Normal Year Forcing

OA: Observational Area

Pre-SC: Pre-Storm Condition

Post-SC: Post-Storm Condition

PTM: Pacific-origin Temperature Maximum

sBSW: Summer Bering Sea Water

SC: Storm Condition

SML: Surface Mixed Layer

SSMI: Special Sensor Microwave Imager

SSMIS: Special Sensor Microwave Imager/Sounder